NUMERICAL SIMULATION OF A DIRECT INJECTION SPARK IGNITION ENGINE USING ETHANOL AS FUEL

By

Shalabh Srivastava

A THESIS

Submitted to
Michigan State University
in partial fulfillment of the requirements
for the degree of

MASTER OF SCIENCE

Department of Mechanical Engineering

2008

ABSTRACT

NUMERICAL SIMULATION OF A DIRECT INJECTION SPARK IGNITION ENGINE USING ETHANOL AS FUEL

By

Shalabh Srivastava

Numerical simulations have been performed to compare the vaporization and combustion of gasoline and ethanol in a direct injection spark ignition engine. The widely used, open source, computational fluid dynamics KIVA - 3V code has been used for this purpose. A multidimensional look up table of ignition delays has been formulated from a detailed mechanism for ethanol oxidation using CHEMKIN™ and has been used to modify the ignition delays predicted by the global one step mechanism used to simulate combustion. The "cold start" phenomenon in ethanol operated engines has been observed in the simulations and various strategies to enhance ethanol vaporization and combustion have been tested. Simulation results indicate that some of the strategies used for emission control and downsizing of gasoline engines may be employed for "improving" combustion in ethanol operated engines.

ACKNOWLEDGEMENTS

I would like to take this opportunity to express my deep sense of gratitude and profound thanks to my thesis advisor Dr. Farhad A. Jaberi, for his constant help, continual encouragement and guidance during the course of my Masters' research. He has been a constant source of inspiration and moral support throughout the course of this work. I would not have completed this work successfully without his incessant support.

I would also like to thank my committee members Dr. Harold Schock, Dr. Andre Benard and Dr. Mei Zhuang for their insights into my work and for finding the time to review my manuscript and make valuable suggestions.

I am indebted to my lab mates Araz, Murat, Li and Mark for providing me with valuable information regarding my work. A special thanks is due to Yuxin Zhang for his invaluable help.

I dedicate this thesis to my family whose constant support, unconditional love and encouragement throughout my life has made this work possible.

Shalabh Srivastava

TABLE OF CONTENTS

LIST OF TABLES

LIST OF FIGURES

Images in this thesis are presented in color.

LIST OF SYMBOLS

Symbol/Abbreviation	Description (page, figure or table of first reference)
ATDC	After Top Dead Centre (29)
BBDC	Before Bottom Dead Centre (29)
BDC	Bottom Dead Centre (30)
BTDC	Before Top Dead Centre (29)
CA	Crank Angle (50)
CAD	Crank Angle Degrees (31)
er	Equivalence Ratio (56)
IC	Internal Combustion (11)
MON	Motor Octane Number (3)
NO_x	NO, NO_2 (8)
RNG	Renormalization Group (14)
RON	Reference Octane Number (3)
SMD	Sauter Mean Diameter (32)
SMR	Sauter Mean Radius (19)

CHAPTER 1

INTRODUCTION

The demand for petroleum based fuels like gasoline and diesel has increased substantially over the last few years, especially in the developing Asian countries like China, India, etc. Considering the fact that the supply of these fuels is limited and is bound to diminish over a period of time, efforts are being made to develop alternative sources of fuels like vegetable oils, alcohols, bio-diesel etc. Out of these, one of the most attractive alternative sources of fuel is bio-based ethanol.

The idea of using ethanol as a fuel for internal combustion engines is not new. Henry Ford himself had envisioned the use of ethanol as an engine fuel [1]. But eventually, ethanol lost out to gasoline due to lower running cost and other practical (commercial) considerations favorable to gasoline. The use of ethanol-gasoline blends was revived in Brazil in the 1980's, with over 3 million vehicles with suitable modifications running on the latest technology.

In the US, recently, there has been an increasing interest in the use of ethanol-gasoline and ethanol-diesel blends. The reasons for this surge are manifold [2]. One of the most important factors is the better emission characteristics of ethanol-blended fuels. The use of such fuels is likely to have a positive impact in the fight to reduce the total emissions from vehicles, particularly NO_x, and would

thus help in reducing the damage to our environment. It is also a "carbon-neutral" source, thus reducing the total greenhouse emissions from the transportation sector. Secondly, the use of biofuels and the consequent development of low temperature more efficient engines would help in reducing the dependence on foreign oil. Thirdly, the Midwest region in the US has huge potential for the production of corn-based ethanol. The development of ethanol based fuels as a major source of energy for automobiles would not only benefit the economy of the region, but it would also increase the competitiveness of the indigenous auto industry.

As a part of the initiative to develop a prototype of ethanol based engines, the aim of this thesis is a numerical investigation of the performance of gasoline and ethanol based engines and to study strategies to enhance the combustion of ethanol.

The thesis is organized as follows. The first Chapter gives an overview of the properties of ethanol as compared to gasoline and the advantages/ disadvantages of using ethanol-blended fuels. The second Chapter discusses the various features of the main tool used to obtain the results in this thesis – the numerical code KIVA 3V. The third Chapter outlines the setup of the problem and the various methodologies and models developed to perform this study, including the ignition delay model. The fourth Chapter presents the results of the study and summarizes the various findings and suggests methods to give a better

quantitative comparison.

1.1 Comparison of properties of Ethanol and Gasoline

An overview of the differences in the physical properties of ethanol and gasoline would be essential to understand the challenges faced in using either of them as fuels in internal combustion engines and also in performing numerical simulations.

Table 1.1 : Properties of Ethanol and Gasoline [3,4]

Parameter	Ethanol	Gasoline
Molecular Weight (g/mol)	46.070	113.228
Average Octane Number (RON+MON)/2	104	91
Lower heating value (kcal/kg)	6700	10394
Latent heat (kcal/kg)	210.7	90.82
Heat of Formation (kcal/mole)	-51.95	-52.78
Liquid Density at 20 degrees C and 1 atm (gm/L)	789.37	751
Boiling Point (K)	351.55	300-498
Ignition Temperature (K)	695.93	530.37
Critical Temperature (K)	513.92	548.0

1.1.1 Octane Number

One of the most important of the differences between ethanol and gasoline is the comparatively higher octane rating of ethanol. The higher octane rating of ethanol allows a higher compression ratio, thus overcoming the disadvantage of a lower heat of combustion.

1.1.2 Latent Heat of Vaporization

As can be seen from Figure 1.01, the latent heat of vaporization of ethanol is 2-3 times higher than that of gasoline. Consequently, more energy is required to evaporate a sufficient amount of fuel to make a combustible fuel – air mixture. This causes a severe "cold start" problem in winter and in colder weather when the engine does not start due to lesser fuel evaporation. This problem is more severe for ethanol as compared to gasoline due to its higher vaporization energy.

1.1.3 Enthalpy

Ethanol has a lower enthalpy than gasoline (Figure 1.02) and contains approx. 34% less energy per unit volume than gasoline. This disadvantage can be offset by increasing the compression ratio of the engine [5], which is possible due to the higher octane number of ethanol.

1.1.4 Vapor Pressure

The Vapor Pressure of ethanol is slightly lower than that of gasoline till about 430 K and is higher at higher temperatures (Figure 1.03). Thus, all other conditions being the same, gasoline will evaporate faster at lower temperatures while ethanol evaporation would be faster at higher temperatures.

1.1.5 Liquid Viscosity

The liquid viscosity of ethanol is higher than gasoline (Figure 1.04). This implies that the liquid droplets of ethanol are difficult to break up as compared to

gasoline, thus effectively reducing the secondary break up of ethanol fuel droplets. Larger droplet size implies lesser fuel evaporation as the total surface area exposed to the hot gases is lesser.

1.1.6 Surface Tension

The surface tension of ethanol is higher than that of gasoline (Figure 1.05). Higher surface tension also leads to lesser secondary breakup of fuel droplets and consequently lesser fuel evaporation.

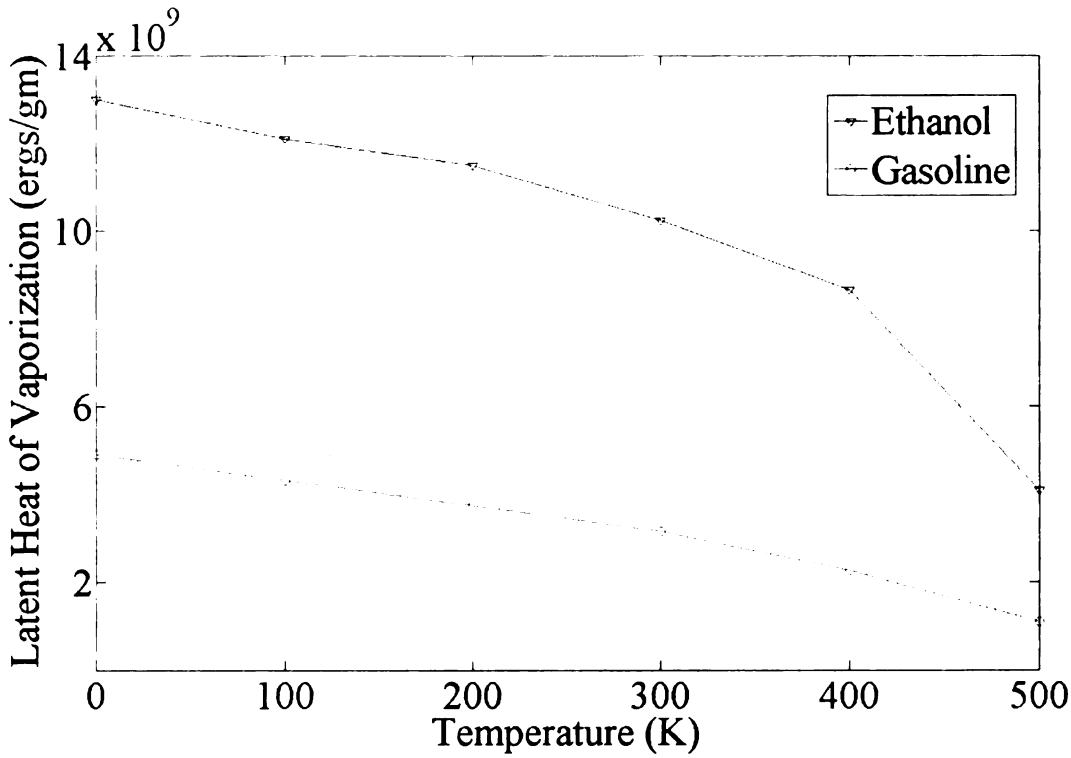

Figure 1.01 Comparison of Latent heat of Vaporization

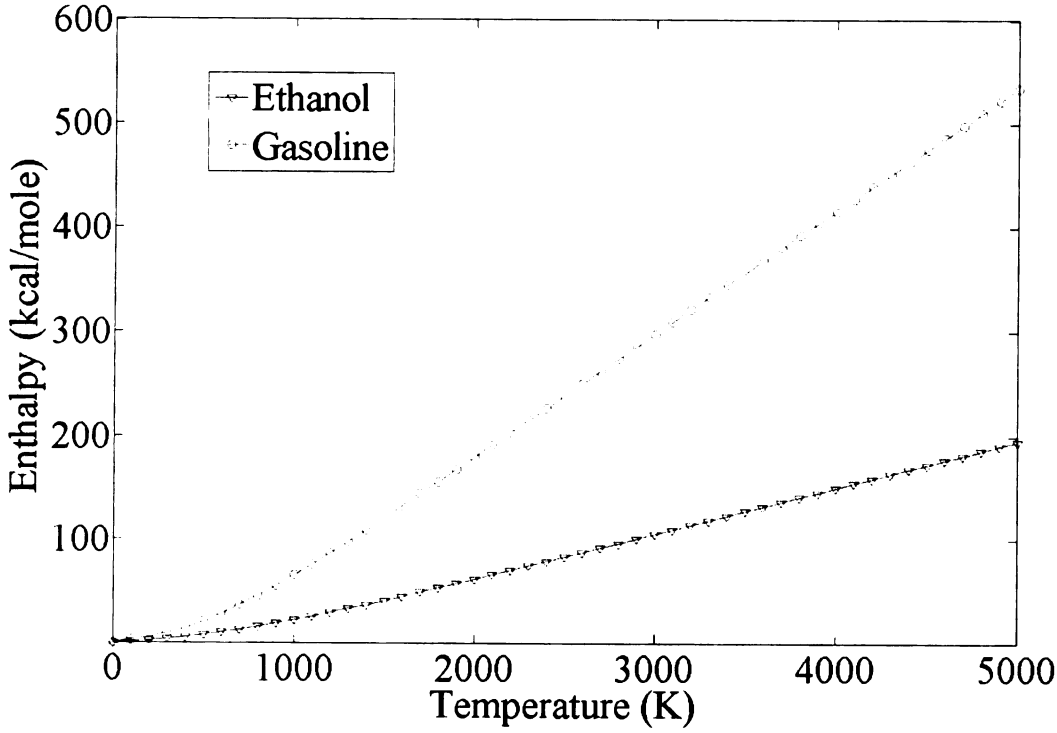

Figure 1.02 Comparison of Enthalpy

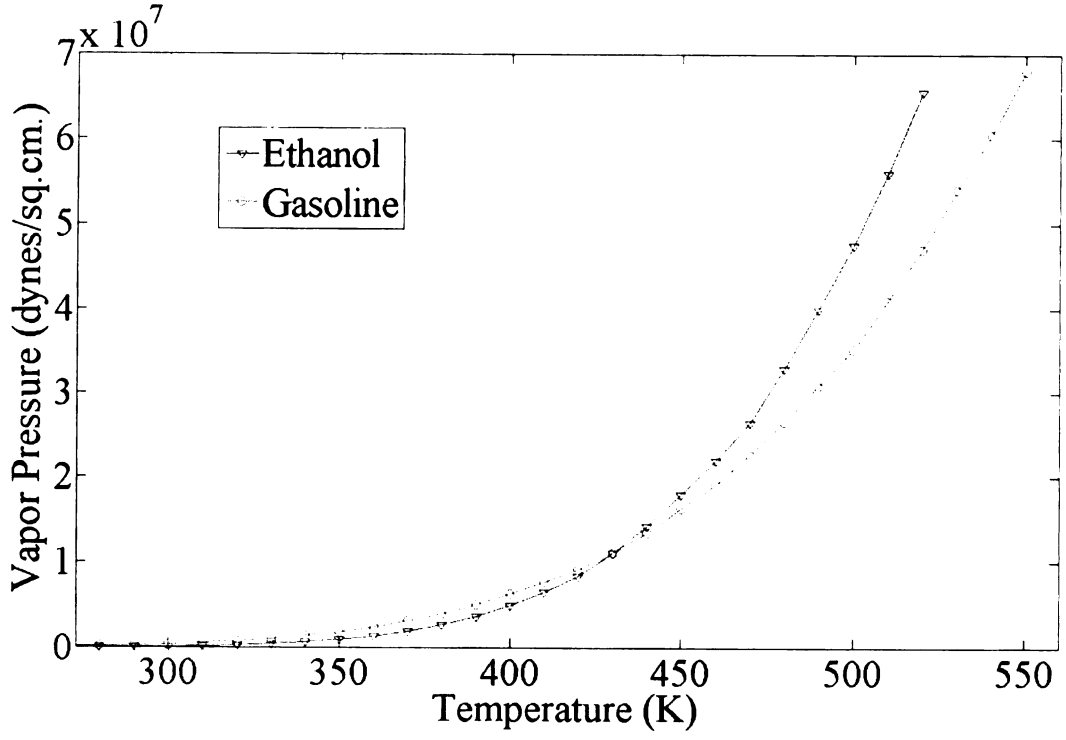

Figure 1.03 Comparison of Vapor Pressure

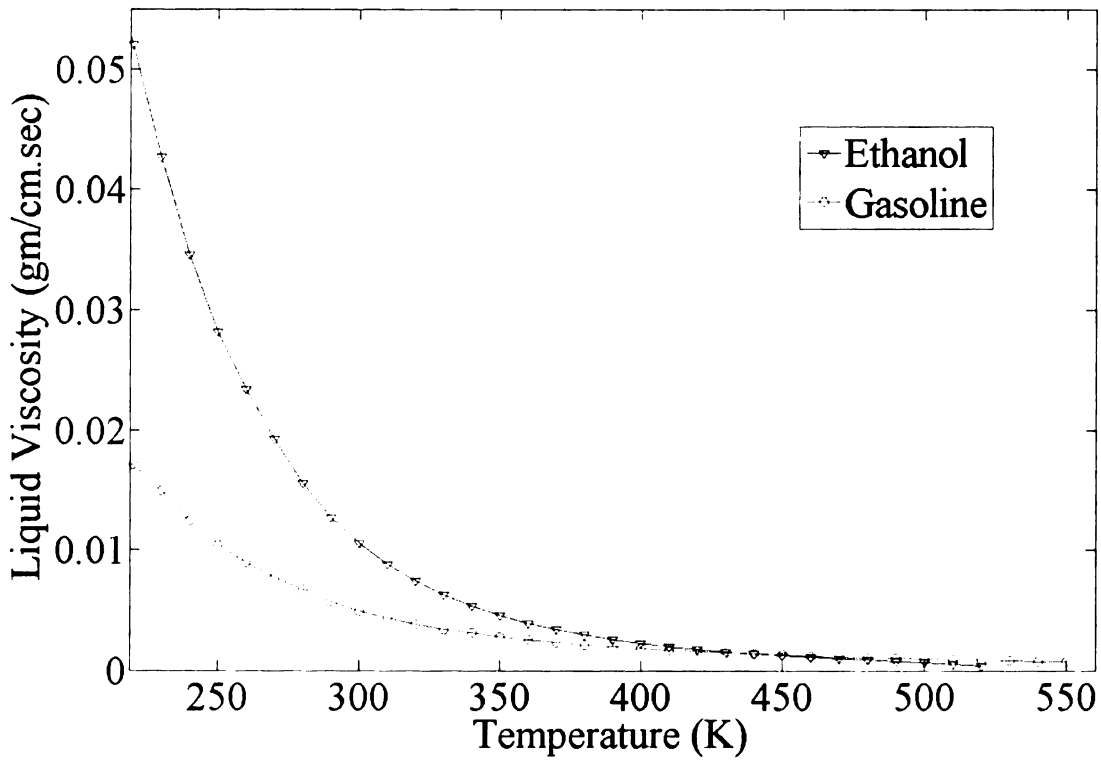

Figure 1.04 Comparison of Liquid Viscosities

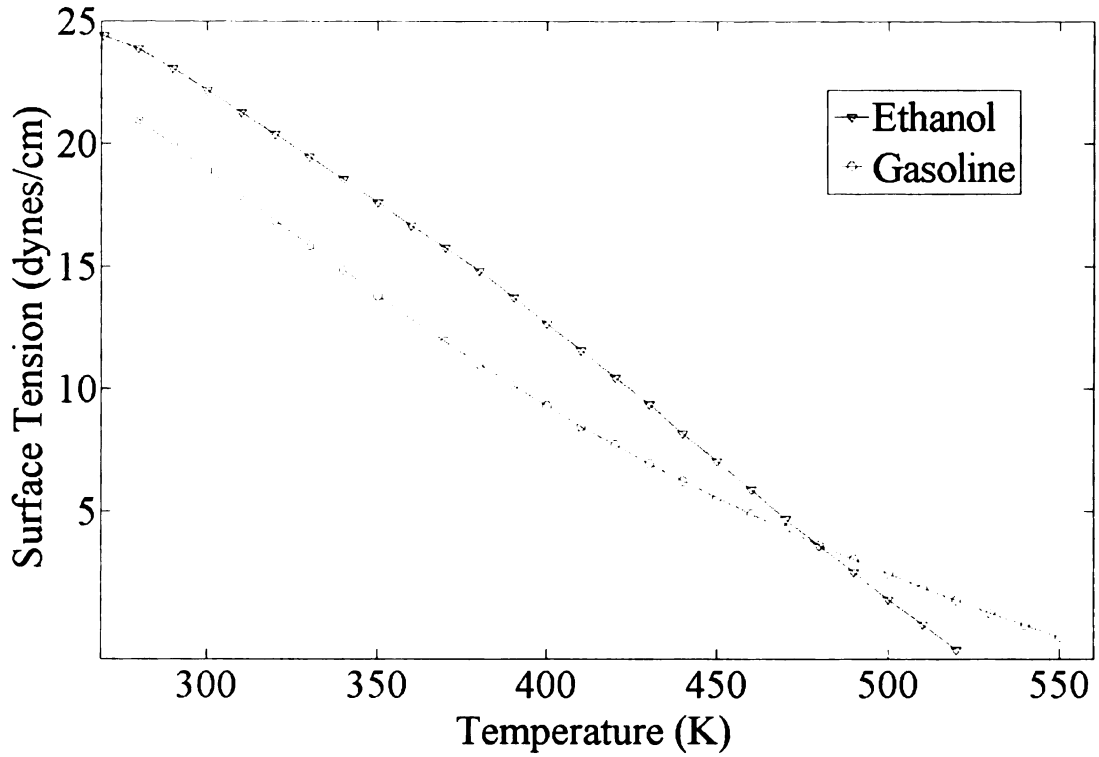

Figure 1.05 Comparison of Surface Tension

1.2 Advantages of Ethanol over Gasoline

Ethanol (and alcohols in general) has many properties that make it advantageous to use it as a fuel for Internal Combustion Engines [1]. The high heat of vaporization of ethanol results in lower peak temperatures, thus reducing the production of NO_x by the thermal mechanism [6]. Emissions such as CO and hydrocarbons are also significantly lesser. Nakata et al. [6] suggest that the emission of unburned hydrocarbons decreases due to the absence of high boiling point components in ethanol. The high octane number of ethanol gives it anti-knocking properties, which can be utilized by increasing the compression ratio, thus increasing the engine power. The use of ethanol also increases the engine efficiency as the cooling heat loss is lower due to the lower combustion temperatures. Ethanol is obtained from agricultural crops like sugarcane, corn, etc., and is thus a renewable source of energy.

1.3 Disadvantages

The use of ethanol as a fuel does have some drawbacks [1]. One of the major problems faced is that of "cold start". Since ethanol has a high heat of vaporization and a low vapor pressure, at low temperatures the evaporation of the fuel is insignificant and the fuel which evaporates further decreases the temperature. Thus, in the colder regions, and at colder times of the day, startup of the engine can be quite troublesome. Effective strategies like hydrogen

enrichment [8], etc. are needed to overcome this deficiency. Use of ethanol reduces emission of regulated pollutants like CO, NO_x and partially burnt hydrocarbons. However, the amounts of unregulated pollutants like aldehydes, which are a major cause of photochemical smog in major urban centers, increase. Production of ethanol requires cultivation of energy crops, excessive growth of these might lead to problems such as soil degradation. Some groundwater modeling studies have also suggested that in case of spilling of ethanol-blended gasoline into the environment, the plume length of benzene in groundwater might increase. [7]

1.4 Strategies to overcome cold start problem

The cold start problem has come under the notice of the automobile industry and academia and consequently many efforts have been made to overcome this problem. One method suggested by Davis [8] is to enrich E85 with hydrogen to exploit its volatility and extremely fast burn rate. Since it is difficult to store, hydrogen is generated when required by a partial oxidation reformer run on E85.

Nakata et al. [6] have studied ways to increase the fuel temperature and compressed gas temperature and have found that valve timing optimization is an effective method to improve cold start combustion. If the valve is opened much later than normal operation and to a smaller lift, the high pressure difference between the intake and cylinder causes the air velocity to increase and

consequently heats up the air. Also, the effective compression ratio can be increased by closing the intake valve near the bottom dead center.

Converting a part of ethanol fuel into a more volatile compound is another promising method to solve the cold start problem [9]. Ethanol can be dehydrated into more volatile ethyl ether during cold start or even earlier on board the vehicle. However, this method requires modification of the combustion chamber to include a catalyst convertor and is also dependent on the availability of a catalyst stable over a wide range.

A catalytic ignition source can be used to aid the combustion of aqueous ethanol, as suggested by Cordon et al.[10] The basic principle in a design utilizing this method would be to ignite a homogeneous charge of liquid ethanol by compression in an catalytic pre-chamber and follow this by torch ignition in the main chamber. Sales et al. [11] suggest burning gasoline during cold start as auxiliary system and using ethanol once the temperatures rise.

Despite the difficulties being faced by the biofuel industry, the use of ethanol is catching on and provided sufficient research is done into the various aspects of the ethanol fuel well-to-wheel process, it has the capability to satisfy some major needs of the automobile industry in the near future.

CHAPTER 2

KIVA 3V

KIVA 3V is a computer program written in FORTRAN which allows numerical modeling of transient 2 dimensional and 3 dimensional chemically reacting flows with sprays in internal combustion engines with vertical or canted valves, and is the major tool used in this project. KIVA was first developed in the 1980's at Los Alamos National Laboratory (LANL) [12-15] and has undergone several revisions over the years [16-18]. The program has been widely used in both industry and academia for both IC engine and non-engine flows and the various models and sub-models have been modified to keep up with latest developments and knowledge of the various processes occurring in Internal Combustion engines. This chapter gives a brief overview of the various models and sub – models in KIVA 3V as their understanding is essential to comprehend the outstanding features and limitations of the simulations.

Each cycle in KIVA is divided into two phases: a Lagrangian Phase and a rezone phase. In the Lagrangian phase, no convection occurs across cell boundaries, with the vertices moving with the fluid velocity. In the rezone phase, the computational mesh is changed by moving the vertices to satisfy user specified coordinates, the flow field being frozen. The flow field is then remapped to the new computational mesh by material convection across the boundaries of the

computational cells.

2.1 Fluid Phase Governing Equations

The differential equations governing the fluid phase in KIVA 3V [15] are given below.

2.1.1 Continuity equation

The continuity equation for species m:

$$\frac{\partial \rho_m}{\partial t} + \nabla.(\rho_m \mathbf{u}) = \nabla.\left[\rho D \nabla\left(\frac{\rho_m}{\rho}\right)\right] + \dot{\rho}_m^c + \dot{\rho}^s \delta_{ml} \qquad \textbf{- (2.1)}$$

Here ρ_m, ρ, $\mathbf{u}$, D, $\dot{\rho}_m^c$ (Equation 2.13) and $\dot{\rho}^s$ are the mass density of species m, total mass density, fluid velocity, diffusion coefficient, source term due to chemistry and source term due to spray, respectively.

2.1.2 Momentum equation

The momentum equation for the fluid mixture in a turbulent flow:

$$\frac{\partial(\rho \mathbf{u})}{\partial t} + \nabla.(\rho \mathbf{u}\mathbf{u}) = -\frac{1}{\alpha^2}\nabla p - \nabla(2/3\rho k) + \nabla.\boldsymbol{\sigma} + \mathbf{F}^s + \rho \mathbf{g}, \qquad \textbf{- (2.2)}$$

where p is the fluid pressure, $\mathbf{F}^s$ is the rate of momentum gain per unit volume due to the spray, $\mathbf{g}$ gives the specific body force and $\boldsymbol{\sigma}$ is the viscous stress tensor given by

$\sigma = \mu\left[\nabla \mathbf{u} + (\nabla \mathbf{u})^T\right] + \lambda \nabla.\mathbf{u}\mathbf{I}$, μ and λ being the first and second coefficients of viscosity, respectively.

2.1.3 Internal energy equation

The internal energy equation for a multiphase mixture with chemical reactions and sprays is:

$$\frac{\partial(\rho I)}{\partial t} + \nabla.(\rho \mathbf{u} I) = -p\nabla.\mathbf{u} - \nabla.\mathbf{J} + \rho\varepsilon + \dot{Q}^C + \dot{Q}^S, \qquad \textbf{- (2.3)}$$

where I is the specific internal energy, $\dot{Q}^C$ (Equation 14) and $\dot{Q}^S$ are the source terms due to chemical heat release and spray interactions, respectively.

$\mathbf{J}$ is the heat flux vector with contributions from heat conduction and enthalpy diffusion.

$\mathbf{J} = -K\nabla T - \rho D\sum_m h_m \nabla(\rho_m / \rho)$, where T is the fluid temperature and h_m is the specific enthalpy of species m.

2.2 TURBULENCE MODELS

The KIVA 3V code provides the facility of using 2 different turbulence models. These models are briefly described below.

2.2.1 Standard $k-\varepsilon$ Model

The standard $k-\varepsilon$ model is a two-equation turbulent viscosity model in which transport equations for turbulent kinetic energy (k) and turbulent kinetic energy dissipation rate (ε) are solved. In KIVA 3V some terms have been added by A.A. Amsden et al[15]. The source term $\dot{W}^S$ is due to interaction with the spray.

In the ε – equation, the source term has been added to account for velocity dilatation induced length scale changes.

$$\frac{\partial \rho k}{\partial t} + \nabla.(\rho \mathbf{u} k) = -\frac{2}{3}\rho k \nabla.\mathbf{u} + \boldsymbol{\sigma} : \nabla \mathbf{u} + \nabla.\left[\left(\frac{\mu}{\mathrm{Pr}_k}\right)\nabla k\right] - \rho\varepsilon + \dot{W}^s \qquad \textbf{- (2.4)}$$

$$\frac{\partial \rho \varepsilon}{\partial t} + \nabla.(\rho \mathbf{u} \varepsilon) = -\left(\frac{2}{3}\dot{c}_{\varepsilon_1} - c_{\varepsilon_3}\right)\rho\varepsilon\nabla.\mathbf{u} + \nabla.\left[\left(\frac{\mu}{\mathrm{Pr}_\varepsilon}\right)\nabla\varepsilon\right]$$

$$+\frac{\varepsilon}{k}\left[c_{\varepsilon_1}\boldsymbol{\sigma} : \nabla \mathbf{u} - c_{\varepsilon_2}\rho\varepsilon + c_s\dot{W}^s\right] \qquad \textbf{- (2.5)}$$

The constants used for this model are the same as those used in the standard model as they have been shown to be acceptable in engine calculations.

$c_{\varepsilon_1} = 1.44, c_{\varepsilon_2} = 1.92, c_{\varepsilon_3} = -1.0, \mathrm{Pr}_k = 1.0, \mathrm{Pr}_\varepsilon = 1.3$

2.2.2 RNG $k-\varepsilon$ Model

This model is a Renormalization Group (RNG) theory variant of the standard $k-\varepsilon$ model, which considers the effects of compressibility using a rapid distortion analysis of the regime applicable to engine flows. This leads to changes in several turbulence model constants and the addition of a term representing the ratio of the turbulent to mean-strain time scale to the ε equation. The modified ε – equation is

$$\frac{\partial \rho \varepsilon}{\partial t} + \nabla.(\rho \mathbf{u} \varepsilon) = -\left(\frac{2}{3}c_{\varepsilon_1} - c_{\varepsilon_3}\right)\rho\varepsilon\nabla.\mathbf{u} - \frac{2}{3}\rho C_\mu C_\eta k \nabla^2.\mathbf{u}$$

$$\nabla.\left[\left(\frac{\mu}{\mathrm{Pr}_\varepsilon}\right)\nabla\varepsilon\right] + \frac{\varepsilon}{k}\left[(c_{\varepsilon_1} - C)\boldsymbol{\sigma} : \nabla \mathbf{u} - c_{\varepsilon_2}\rho\varepsilon + c_s\dot{W}^s\right] \qquad \textbf{- (2.6)}$$

where $\mu = \mu_0 + \rho.\nu_t = \mu_0 + \rho C_\mu \frac{k^2}{\varepsilon}$

2.3 CHEMICAL REACTIONS

KIVA allows any number of chemical reactions with any number of species. However, in practice, the number of chemical reactions and species is limited by considerations like minimum timestep and stiffness of the system of equations. By default, KIVA has 13 chemical species: Fuel, O_2, N_2, CO_2, H_2O, H, H_2, O, N, OH, CO, NO, HO_2. The user can solve any number of reactions involving these species.

The chemical reactions occurring in the system are represented as

$$\sum_m a_{mr}\chi_m \Leftrightarrow \sum_m b_{mr}\chi_m \qquad \textbf{- (2.7)}$$

where χ_m represents one mole of species m.

By mass conservation, the integral stoichiometric coefficients for reaction r, a_{mr} and b_{mr}, must satisfy

$$\sum_m (a_{mr} - b_{mr})W_m \qquad \textbf{- (2.8)}$$

The rate of kinetic chemical reaction r, $\dot{\omega}_r$ is given by

$$\dot{\omega}_r = k_{fr}\prod_m (\rho_m / W_m)^{a'_{mr}} - k_{br}\prod_m (\rho_m / W_m)^{b'_{mr}} \qquad \textbf{- (2.9)}$$

where a'_{mr}, b'_{mr} are reaction orders and k_{fr}, k_{br} are coefficients given by the Arrhenius expressions:

$$k_{fr} = A_{fr}T^{\zeta_{fr}} \exp\{-E_{fr}/T\} \qquad \textbf{- (2.10)}$$

$$k_{br} = A_{br}T^{\zeta_{br}} \exp\{-E_{br}/T\} \qquad \textbf{- (2.11)}$$

E_{fr} and E_{br} are the activation energies of the forward and backward reactions.

In addition to the kinetic reactions, KIVA has the facility for equilibrium reactions to take into account the effect of some species which exist in equilibrium at adiabatic flame temperatures.

These reactions are:

$N_2 \Leftrightarrow 2N$, $O_2 \Leftrightarrow 2O$

$2CO_2 \Leftrightarrow 2CO+O_2$

$H_2 \Leftrightarrow 2H$

$2OH \Leftrightarrow O_2+H_2$

$2H_2O \Leftrightarrow 2H_2+O_2$

The rates of these equilibrium reactions are determined by imposing the constraints that

$$\prod_m (\rho_m / W_m)^{b_{mr} - a_{mr}} = K_c^r(T) = \exp\{A_r \ln T_A + B_r / T_A + C_r + D_r T_A + E_r T_A{}^2\},$$

where $T_A = T / 1000\,\mathrm{K}$ **- (2.12)**

The source term $\dot{\rho}_m^c$ in equation (1) and the source term $\dot{Q}^c$ in equation (3) are given by

$$\dot{\rho}_m^c = W_m \sum_r (b_{mr} - a_{mr}) \dot{\omega}_r \qquad \textbf{- (2.13)}$$

$$\dot{Q}^c = \sum_r Q_r \dot{\omega}_r \,, \quad Q_r = \sum_m (a_{mr} - b_{mr})(\Delta h_f^0)_m \qquad \textbf{- (2.14)}$$

Here $(\Delta h_f^0)_m$ is the heat of formation of species m at absolute zero.

2.4 Essential features of a spray simulation

In order to properly simulate the spray process in an IC engine, the effects of various sub – processes like drop breakup, distortion and drag, turbulent dispersion, drop collision and coalescence, drop vaporization and spray-wall interaction need to be modeled. In KIVA 3V, a discrete particle technique is used to represent evaporating liquid sprays. Each computational particle represents a number of drops of identical size, velocity and temperature with Monte Carlo sampling techniques used to determine the properties of the droplets at injection and downstream locations. Mass, momentum and energy exchange govern the interaction between the spray and fluid. The following spray equation is used to represent the evolution of the spray:

$$\frac{\partial f}{\partial t} + \nabla_{\mathbf{x}} \cdot (f\mathbf{v}) + \nabla_{\mathbf{v}} \cdot (f\mathbf{F}) + \frac{\partial (fR)}{\partial r} + \frac{\partial (f\dot{T}_d)}{\partial T_d} + \frac{\partial (f\dot{y})}{\partial y} + \frac{\partial (f\ddot{y})}{\partial \dot{y}} = \dot{f}_{coll} + \dot{f}_{bu} \qquad \textbf{- (2.15)}$$

Here $\mathbf{x}$ represents the three components of the droplet position, $\mathbf{v}$ the three droplet velocity components, r the equilibrium radius, T_d the uniform droplet temperature, y the distortion from sphericity and $\dot{y}$ the time rate of change of y. F, R, $\dot{T}_d$, and $\ddot{y}$ are the time rates of change of $\mathbf{v}$, r, T_d and $\dot{y}$ respectively. f is the droplet probability distribution function, defined such that $f(\mathbf{x}, \mathbf{v}, r, T_d, y, \dot{y}, t)d\mathbf{v}drdT_d dyd\dot{y}$ gives the probable number of droplets per unit volume at position x and time t with velocities in the interval $(\mathbf{v}, \mathbf{v} + d\mathbf{v})$, radii in the interval $(r, r + dr)$, temperatures in the interval $(T_d, T_d + dT_d)$, and displacement parameters in the interval $(y, y + dy)$ and $(\dot{y}, \dot{y} + d\dot{y})$.

$\dot{f}_{coll}$ is the source term due to droplet collisions and $\dot{f}_{bu}$ is the source term due to droplet breakup. Detailed expressions for these source terms are given in [15].

2.4.1 Droplet Drag and Dispersion

In order to include the effect of turbulence on the droplet drag, its heat and mass exchange with the gas and its oscillation and breakup, a fluctuating velocity $\mathbf{u}'$ is added to the local mean gas velocity. Each component of $\mathbf{u}'$ follows a Gaussian distribution with mean square deviation $2/3k$, where k is the specific turbulent kinetic energy of the gas in the cell in which the particle is located. Thus, the acceleration of a droplet F is given by

$$F = \frac{3}{8}\frac{\rho}{\rho_d}\frac{|\mathbf{u}+\mathbf{u}'-\mathbf{v}|(\mathbf{u}+\mathbf{u}'-\mathbf{v})C_D}{r}+\mathbf{g} \qquad \textbf{- (2.16)}$$

where the first term on the right hand side represents the aerodynamic drag and the second term represents the gravitational force.

2.4.2 Droplet Collision and Coalescence

When two droplets collide, there are two possibilities: either they coalesce or they undergo velocity changes, depending on the forces acting on them. At lower Weber numbers, surface tension forces dominate, causing the drops to coalesce, while at higher Weber numbers they separate due to higher inertia forces [19]. To implement this in KIVA, a collision impact parameter b is calculated and compared to a critical collision parameter b_{crit} that depends on the Weber number. If $b < b_{crit}$, the droplets coalesce, otherwise they undergo velocity

changes. The collision calculation is performed only for particles in the same computational cell, thus making the simulation dependent on the number of particles and fineness of the grid.

2.4.3 Spray Atomization and Breakup

2.4.3.1 Spray Atomization

KIVA 3V offers two methods to determine the droplet size distribution at injection. One is to inject a mono-disperse distribution with droplet size being determined by the specified Sauter Mean Radius (SMR). The other is to use a χ-squared distribution for the sizes of injected droplets. In this case,

$f(r) = \frac{1}{\bar{r}} e^{-r/\bar{r}}$, where $\bar{r} = \frac{1}{3} r_{32}$ is the number – averaged drop radius and r_{32} is the input SMR. In either case, further atomization is governed by the spray breakup model.

2.4.3.2 Drop Breakup - Taylor Analogy Breakup (TAB) Model

The spray droplet breakup in KIVA 3V is modeled by the Taylor Analogy Breakup (TAB) model, which is based on the analogy between an oscillating droplet and a spring-mass system, originally proposed by Taylor and implemented in KIVA by O'Rourke and Amsden [20]. According to this model, a droplet breaks up into a distribution of smaller droplets if its distortion y, which is proportional to the displacement of the droplet surface from its equilibrium position divided by the droplet radius r, is greater than 1. y is governed by the following equation of a forced, damped harmonic oscillator:

$$\ddot{y} = \frac{2}{3}\frac{\rho}{\rho_d}\frac{(\mathbf{u}+\mathbf{u}'-\mathbf{v})^2}{r^2} - \frac{8\alpha(T_d)}{\rho_d r^3}y - \frac{5\mu_l(T_d)}{\rho_d r^2}\dot{y} \qquad \text{- (2.17)}$$

Here, $\mathbf{u}$, $\mathbf{u}'$, ρ, ρ_d, $\alpha(T_d)$, and $\mu_l(T_d)$ are the gas velocity, gas turbulence velocity, gas density, spray droplet density, liquid surface tension coefficient and liquid viscosity, respectively

As can be seen from the above equation, the gas aerodynamic forces on the droplet supply the external force, the surface tension forces supply the restoring force and the liquid viscosity supplies the damping force. Thus, higher aerodynamic forces would favor breakup and higher surface tension forces and liquid viscosity would be unfavorable.

2.4.4 Drop Vaporization

The rate of change of radius of the droplet due to mass transfer (vaporization) depends on the Sherwood number for mass transfer (Sh_d), the fuel vapor mass fraction at the droplet's surface (Y_1^*), the fuel vapor mass fraction in the cell ($Y_1 = \rho_1 / \rho$) and the fuel vapor diffusivity in air ($(\rho D)_{air}(\bar{T})$) and is given by the Frossling correlation:

$$R = \frac{dr}{dt} = -\frac{(\rho D)_{air}(\bar{T})}{2\rho_d r}\frac{Y_1^* - Y_1}{1 - Y_1^*}Sh_d \qquad \text{- (2.18)}$$

The heat conducted to the droplet from the surrounding air either increases the temperature of the droplet or causes phase change by providing latent heat for vaporization. Thus, the rate of droplet temperature change is given by:

$$\rho_d \frac{4}{3}\pi r^3 c_l \dot{T}_d - \rho_d 4\pi r^2 RL(T_d) = 4\pi r^2 Q_d \quad \textbf{- (2.19)}$$

where Q_d is the rate of heat conduction to the droplet surface per unit area, c_l is the liquid specific heat, and $L(T_d)$ is the latent heat of vaporization.

The whole calculation is carried out under the assumption that the temperature of the droplet is uniform.

2.4.5 Spray Wall Interaction and Wall film model

The interaction of the spray with the wall and the consequent formation of a wall-film is an important phenomenon in Internal Combustion Engines. Although Direct Injection Spark Ignition engines overcome the problem of fuel wall wetting in the port, however, there is still a possibility of wall film formation at the piston and cylinder walls as the time the fuel gets for vaporization is significantly lesser than for a port injected engine [21]. Wall film formation is known to lead to increased heat loss and rise in emission of unburned hydrocarbons due to pool burning at the wall. Thus, there is a need to model spray wall interaction and wall film formation.

KIVA uses a particle based wall film model. The wall film model considers the effect of mass, tangential momentum and energy addition due to the spray particles to the wall film and also splashing of spray particles. Other features of the wall film are discussed below.

2.5 Wall Film Model

The wall film model [22, 23] in KIVA 3V, models the film formation and transport on engine surfaces, heating and vaporization of the wall film, and the separation and re-entrainment of the wall film at sharp corners. Wall film dynamics is not only affected by the spray but also by the interaction of the wall film with the wall and the gas flow near the wall. The wall affects the wall film transport by the no-slip boundary condition and the vaporization by heat transfer from the wall to the film. Interaction with the gas boundary layers above the film affects the film transport and heat and mass transfer from the film. In order to predict this interaction with the gas boundary layer, new wall models have been developed.

2.5.1 Wall film mass equation

$$\frac{\partial \rho_l h}{\partial t} + \nabla_s [\rho_l (\bar{u}_l - v_w) h] = M \qquad \textbf{- (2.20)}$$

Here ρ_l, h, $\frac{\partial}{\partial t}$, ∇_s, $\bar{u}_l$, v_w and M are the constant liquid density, film thickness, time-rate-of-change in the frame of reference of the wall, surface gradient operator, mean film velocity in the laboratory frame, wall velocity and the mass source per unit wall area due to impingement, re-entrainment and vaporization, respectively.

The use of the particle method enables the conservation of the wall film mass without the need to solve the mass equation.

2.5.2 Wall film momentum equation

$$\rho h\left\{\frac{\partial u_f}{\partial t}+\left[(\mathbf{u}_f-\mathbf{u}_w).\nabla_s\right]\mathbf{u}_f\right\}+h\nabla_s p_f=\tau_w t-\mu_f(T_f)\frac{\mathbf{u}_f-\mathbf{u}_w}{h/2}$$

$$+\dot{P}_{imp}-(\dot{P}_{imp}.\mathbf{n})\mathbf{n}+\dot{M}_{imp}\left[(\mathbf{u}_w.\mathbf{n})\mathbf{n}-\mathbf{u}_f\right]+\delta p_f\mathbf{n}+\rho h\mathbf{g}, \qquad \textbf{- (2.21)}$$

where τ_w, t, μ_f, T_f, $\dot{P}_{imp}$, $\dot{M}_{imp}$, p_f, δp_f and $\mathbf{g}$ are the shear stress on the gas-side of the wall film, unit tangent to the wall in the direction $\mathbf{u}_f\cdot\mathbf{u}_w$, temperature dependent film viscosity, mean film temperature, momentum source/area due to impingement, liquid mass source/area due to impingement, film (impingement) pressure, pressure difference across film to bring about $(\mathbf{u}_f\cdot\mathbf{u}_w)\cdot\mathbf{n}=0$ and acceleration due to gravity, respectively. This equation has been derived assuming that the film velocity varies linearly within the film, and has a mean value $\mathbf{u}_f$ such that there is no relative velocity with respect to the wall in the normal direction.

2.5.3 Wall film energy equation

$$\rho_l h C_{vl}\left\{\frac{\partial\overline{T}_l}{\partial t}+\left[(\overline{\mathbf{u}}_l-\mathbf{v}_w)\nabla_s\right]\overline{T}_l\right\}=\lambda_l(\overline{T}_l)\left[\frac{T_s-\overline{T}_l}{h/2}-\frac{\overline{T}_l-T_w}{h/2}\right]$$

$$+Q_{imp}-I_l(\overline{T}_l)M_{imp} \qquad \textbf{- (2.22)}$$

where C_{vl} and λ_l are temperature dependent liquid specific heat and heat conductivity respectively, $I_l(\overline{T}_l)$ is the liquid internal energy at temperature $\overline{T}_l$, T_w is the wall temperature and Q_{imp} is the source term due to spray impingement.

2.6 Numerical Scheme

Some of the outstanding features of the numerical scheme are discussed in this section. The details of the discretisation of the equations and their solution can be found in the KIVA manuals [15-18].

2.6.1 Temporal Differencing

KIVA uses an implicit first-order temporal difference scheme for the Lagrangian Phase A and Phase B calculations. Calculations in Phase A consist of spray droplet collision and breakup terms, and mass and energy source terms due to the chemistry and spray. Phase B calculates the pressure gradient in the momentum equation, velocity dilatation terms in the mass and energy equations, momentum source term due to spray, terms due to diffusion of mass, momentum and energy terms, and the remaining source terms in the turbulence equations.

For the rezone phase or Phase C, an explicit subcycled scheme is used with a time step which is a submultiple of the main computational time step, thus ensuring stability.

2.6.2 Spatial Differencing

A control volume approach called the Arbitrary Lagrangian Eulerian method is used for spatial differencing. In this scheme, since the positions of the vertices of the hexahedral cells in the computational mesh can be specified arbitrarily as functions of time, a Lagrangian, Eulerian or a mixed approach can be used, hence the name.

CHAPTER 3

PROBLEM SPECIFICATION AND SETUP

The engine used in this thesis is a Ford 5.4 L 3 Valve Single Cylinder Engine. The engine has a pent-roof combustion chamber with two intake valves tilted at an angle of 5.1 degrees and one exhaust valve tilted at an angle of 5.8 degrees. The mesh used for the simulations has the same bore diameter and valve location and shape as the original engine but there are some differences in the cylinder head. The original cylinder head has some complicated features that could not be replicated in the mesh due to the limitations of the grid generator. The mesh has approximately 50000 cells at the bottom dead centre. Top and front views of the mesh are shown in Figure 3.01. The main specifications of the engine are given in the table below:

Table 3.1: Main Engine Specifications

Number of Cylinders	1
Bore	90.216 mm
Stroke	83.205 mm
Compression Ratio	9.8
Squish Clearance	2.945 mm
Engine Speed	2500 rpm

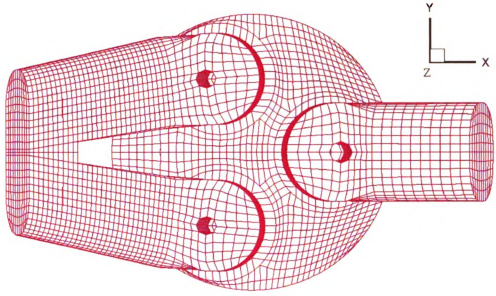

(a) Top View of Computational Mesh

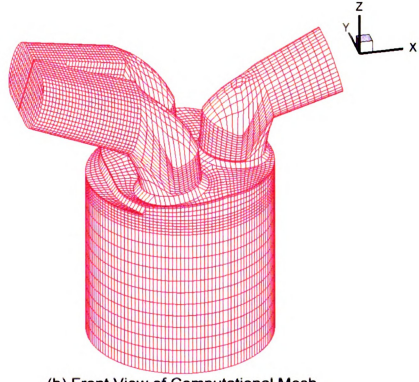

(b) Front View of Computational Mesh

Figure 3.01 Computational Mesh

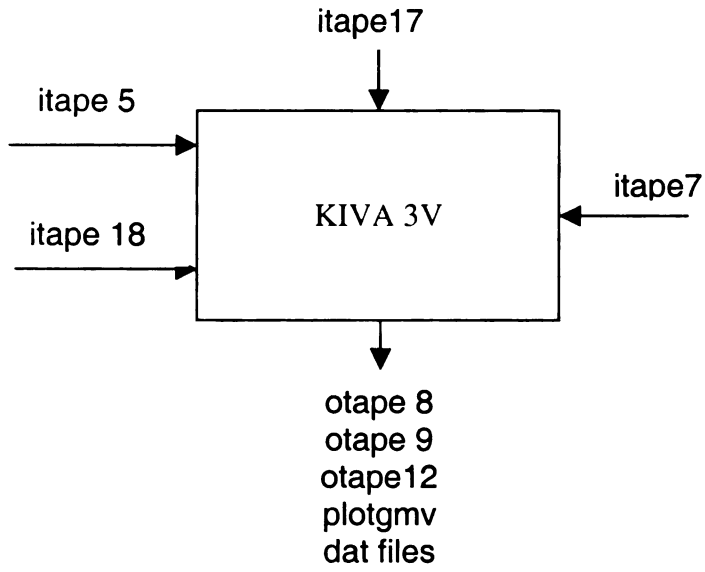

Figure 3.02 KIVA 3V inputs and outputs

Description of input and output files

Input files

itape17: Details of the grid

itape5: Main input file with initial and boundary conditions

itape18: Details of the valve lifts

itape7 : Restart file. Used if restarting a previous simulation.

Output files

otape8: Restart file

otape9: Detailed output for post processing

otape12: General information

plotgmv: Post processing file for TECPLOT

dat files: Summary files for in cylinder conditions

3.1 Grid Validation

The results from a computational simulation are sensitive to the resolution of the numerical grid. The solution of the governing Navier – Stokes equations becomes more accurate as the fineness of the grid increases. The standard way of testing the suitability of the grid is to change the grid density and observe the changes. But, due to the primitive nature of KIVA's grid generator, this is not possible. Another way to check the grid would be to compare the results obtained from a simulation with a well established physical relationship. Figure 3.03 compares the air mass calculated by adding up the air mass in individual cells with the air mass calculated using the ideal gas equation. Both match, indicating the satisfactory accuracy of the grid.

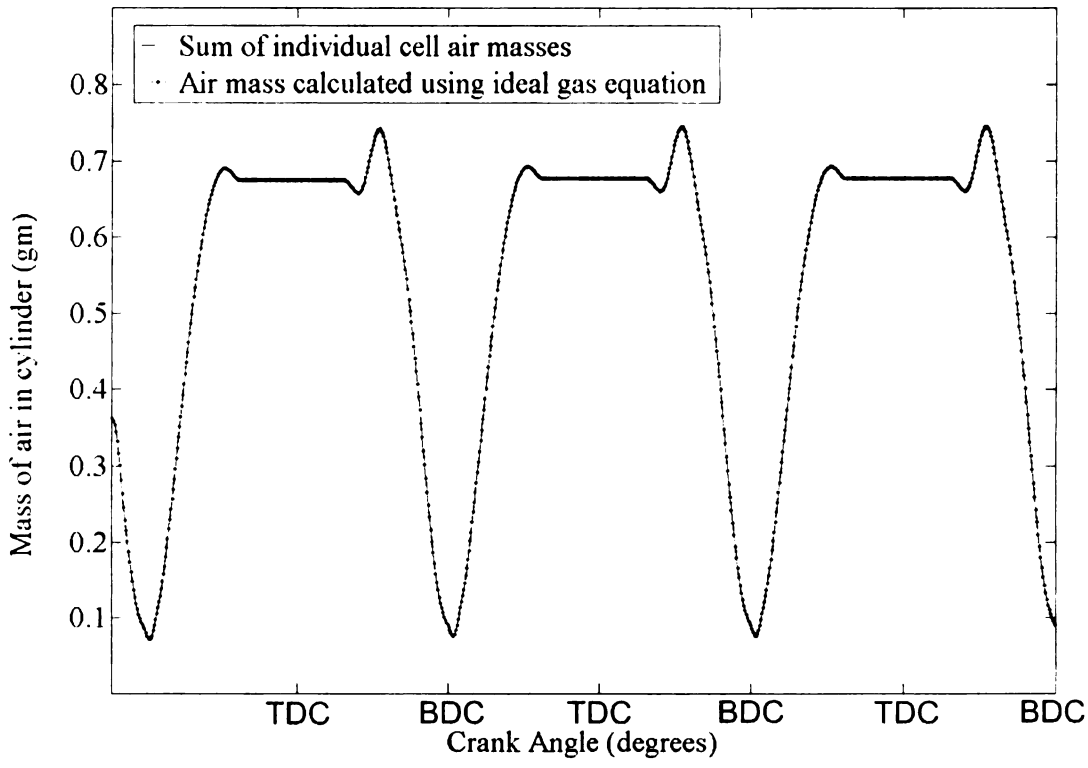

Figure 3.03 Air Mass calculated by two different methods

3.2 Valve Lifts

The intake and exhaust valve lifts are shown in Figure 3.04. The intake valves open 2-3 degrees before top dead centre (BTDC) and close completely 220 degrees after top dead centre (ATDC) and are thus open a few degrees after the piston starts moving up in the compression stroke. This leads to some backflow of air and effectively reduces the compression ratio. The exhaust valve starts opening near the end of the expansion stroke, about 80 degrees BBDC and closes near the end of the exhaust stroke, its closing coinciding with the opening of the exhaust valves.

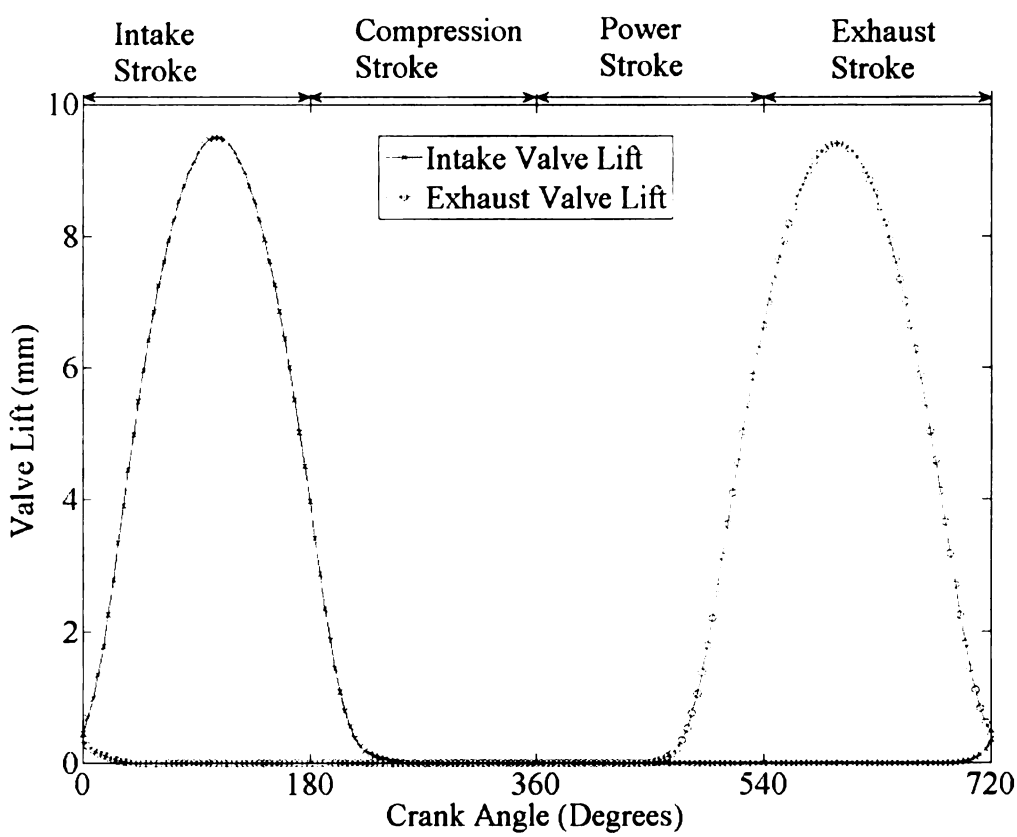

Figure 3.04 Valve Lifts for the intake and exhaust valves

3.3 Spray Configuration

Figure 3.05 gives a description of the parameters required to describe the location of the spray nozzles and the orientation of the spray.

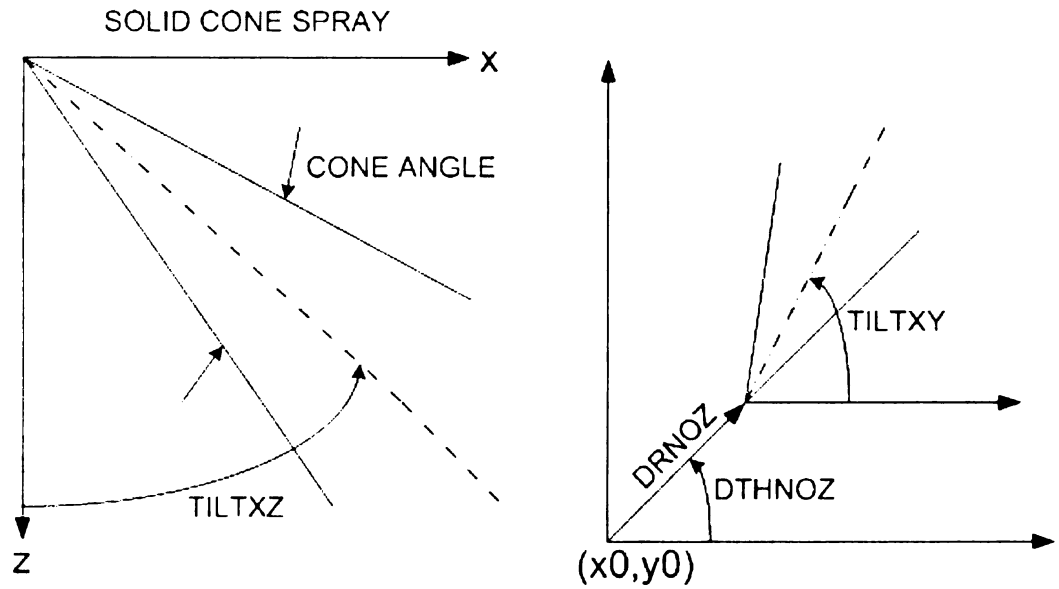

Figure 3.05: Definition of Spray Parameters

DRNOZ : Radius to the the location of the nozzle from the centre (x0,y0) of the cylinder

DZNOZ : Height of the nozzle from the piston at BDC i.e from z=0.

DTHNOZ : Azimuthal rotation in degrees, measured counter-clockwise from the y=0 axis

TILTXZ : x-direction inclination of the spray axis from vertical in the x-z plane

TILTXY : Rotation of the spray axis in the x-y plane, measured counter-clockwise from the x-axis

CONE : Cone angle for solid cone spray

Table 3.2 Spray Orientation Parameters

Number of Nozzles = 8

S.No.	DRNOZ (cm)	DZNOZ (cm)	DTHNOZ (degrees)	TILTXY (degrees)	TILTXZ (degrees)	CONE (degrees)
1	2.05	11.05	180	0	13	8
2	2.15	11.15	180	0	57	8
3	2.1	11.1	181.4	22	35	8
4	2.1	11.1	178.6	-22	35	8
5	2.06	11.14	181	-16	19	8
6	2.06	11.14	179	16	19	8
7	2.14	11.06	181	-16	51	8
8	2.14	11.06	179	16	51	8

Table 3.3 Other Spray Parameters

Parameter	Specification	
Injection time and duration	Crank Angle	Time
(i) Start of injection	2239 ATDC	0.1546 s
(ii) Duration of injection	101 CAD	6.733 ms
(iii) End of Injection	2340 ATDC	0.1613 s
Number of particles	64000	
Shape of Pulse	Square	
Injection Velocity	50 m/s	
Sauter Mean Radius (SMR)	15 μm	

3.3.1 Number of Spray Parcels

The behavior of the liquid spray phase depends significantly on the number of parcels used in the stochastic particle technique. The larger the number of parcels, better is the resolution of the liquid phase and better the statistical convergence [24]. However, using larger number of parcels is computationally expensive and the choice of number of parcels should be such that resolution is maximized and computer time minimized. Figure 3.06 shows the mean equivalence ratio of ethanol for runs with different number of parcels. It can be seen that while there are significant changes in the mean equivalence ratio when the number of parcels per nozzle is increased from 2000 to 8000, further increase in the number of parcels does not seem to have a major effect. But, the increase in computational time is substantial and this fact places an upper limit on the choice of the number of parcels. Injecting 8000 parcels seems to be a good choice to properly simulate the spray and still be able to carry out a parametric study.

3.3.2 Sauter Mean Diameter

Sauter Mean Diameter (SMD) is a measure of the average drop size of a spray and is defined as the diameter of a drop which has a volume-to-surface area ratio equal to the ratio of the sum of the volumes to the sum of the surface areas of all droplets in the spray [24].

$$SMD = \frac{\sum_{i=1}^{n} d_i^3}{\sum_{i=1}^{n} d_i^2}$$, where d_i is the diameter of the i[th] droplet.

A smaller SMD would imply higher surface area per unit volume, leading to more effective evaporation and mixture formation. The injectors in Direct Injection engines are designed to provide highly atomized fuel sprays and SMD's can be as low as 25 μm [24]. The value of SMD used for the simulations here is 30 μm.

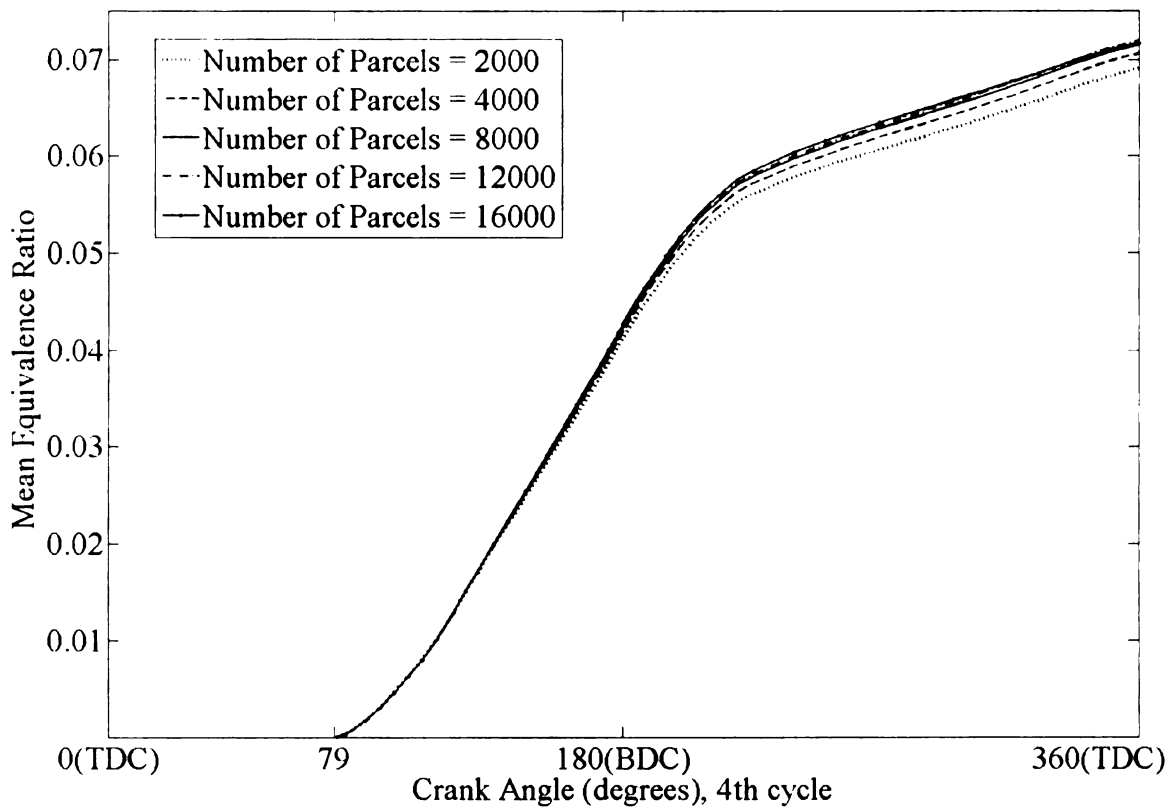

Figure 3.06 Effect of number of parcels on mean equivalence ratio

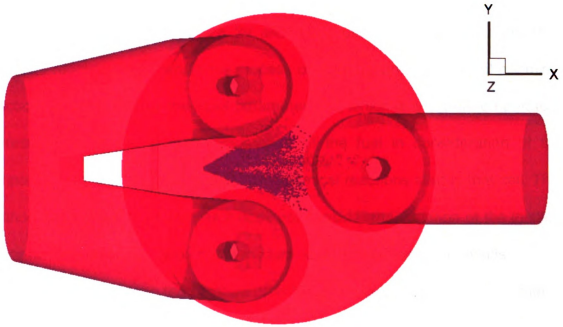

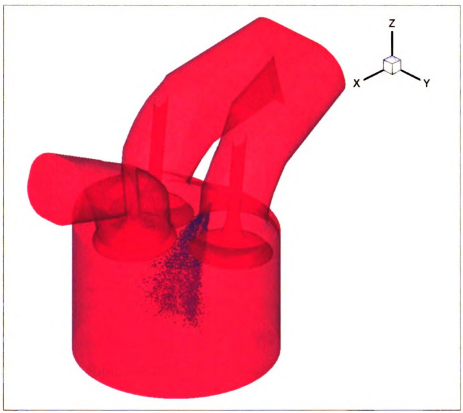

Figure 3.07 Spray configuration

3.4 Combustion Model

As explained in Chapter 2, KIVA 3V allows the use of an arbitrary number of chemical reactions to simulate the process of combustion. The start of chemical reactions is controlled by the input parameter *tcut*, which is a cut-off temperature corresponding to the ignition temperature of the fuel in consideration. If the temperature in a cell is greater than *tcut*, chemical reactions start in that cell. This method has severe limitations as it does not consider the variation of the ignition temperature with composition of the mixture, leading to unphysical results.

Figure 3.08 shows mean temperature plots for a simulation with ethanol as fuel.

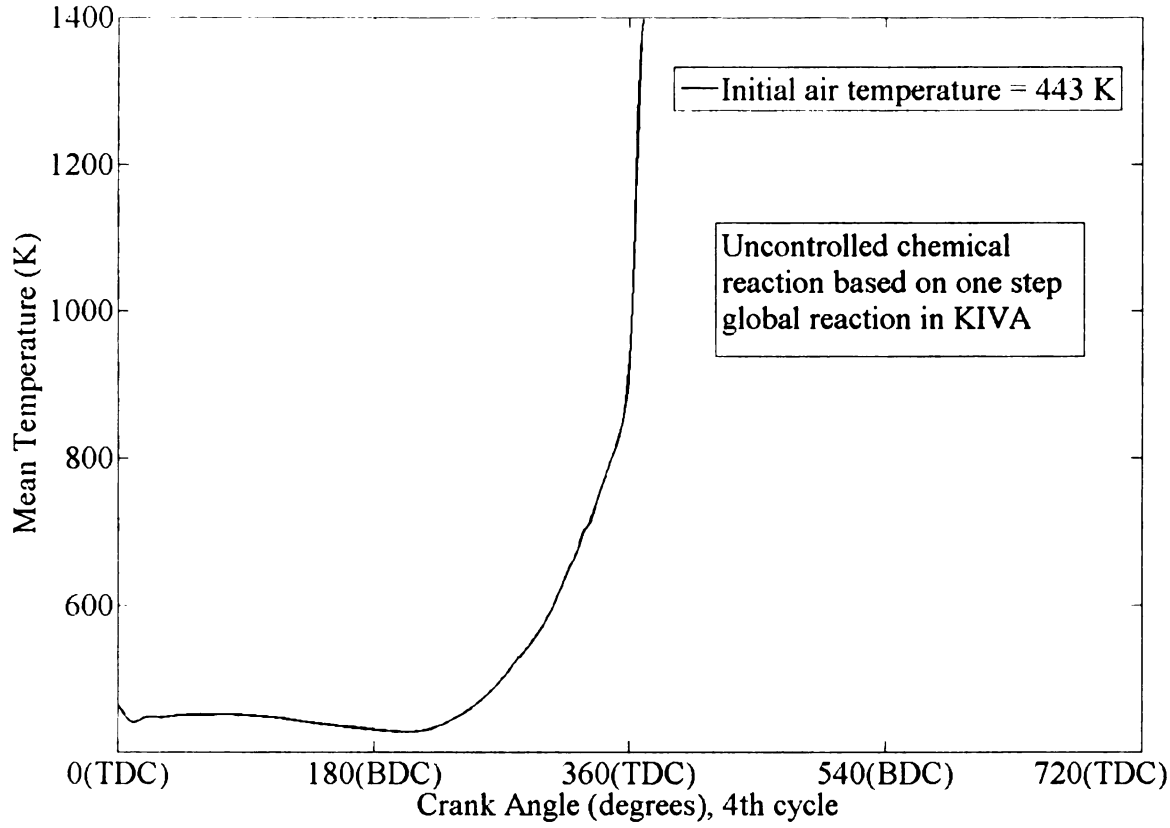

Figure 3.08 Simulations based on original KIVA combustion model

In the above case, no additional energy has been provided in the form of spark, but still combustion starts before Top Dead Centre is reached. This autoignition behavior is typical of a compression ignition engine and is uncharacteristic of a spark ignited engine based on ethanol. This autoignition is due to the fact that the ignition delays predicted by the one step global reaction used in KIVA are much smaller than the actual ignition delays. The global reaction does not consider the initiation and chain – branching steps, leading to smaller ignition delays. There is a need to improve the combustion model in KIVA in order to simulate the actual combustion process as accurately as possible.

One method to overcome this problem might be to delay the onset of the combustion process by making adjustments to the ignition delays predicted by the global reaction using ignition delays calculated by other means such as empirical ignition delay correlations or detailed chemical mechanisms.

3.4.1 Ignition Delay Correlations

Curran et al. provide a global ignition delay correlation for ethanol [25]:

$$\tau = 10^{-14.0} \exp(15500/T) [C_2H_5OH]^{-0.315} [O_2]^{-0.78} [Ar]^{+0.259}$$

This correlation has been obtained from shock tube data for ethanol/oxygen mixtures diluted in Argon and is valid for temperatures from 1100 – 1900 K and equivalence ratios from 0.25 – 1.5. The ignition delay time is in seconds.
Another correlation for the low temperature range of 667-743 K is given by

Bollentin et al. [26].

$$\tau = 6.53\times10^{-19}\exp(42140/(1.9858)T)[C_2H_5OH]^{-1.059}[O_2]^{-0.146}[N_2]^{+0.104}$$

The correlation was obtained by performing a study in a Le Chatelier type closed static reactor at a pressure of 1 atm. and has a correlation coefficient of 0.987. The major difference between the high temperature correlation of Curran and low temperature correlation of Bollentin is the high activation energy for the ignition at low temperautures. Bollentin et al. in their study also showed that the ignition delays predicted by these two correlations match at about 850 K. The high temperature correlation can thus be used for calculating ignition delays at temperatures higher than 850 K, the other correlation being used for lower temperatures.

Figure 3.09 compares the ignition delays obtained from the above correlations with the ignition delays obtained from the global reaction in KIVA for temperature and equivalence conditions typical of internal combustion engines. It can be seen that, as expected, the global reaction gives much lower ignition delays as compared to the ignition delays obtained from the correlations. Thus, if the ignition delays calculated using the correlations where incorporated into the global mechanism ignition delays, the deficiencies of the global mechanism can be overcome to an extent.

The fact that the empirical ignition delay correlations have been deduced from ignition delay data over a limited range of temperatures, pressures and equivalence ratios and the conditions in an internal combustion vary over a much wider range, encourages us to look towards other alternatives to these correlations, like look up tables formed from detailed mechanism data and valid over a wider range of parameters.

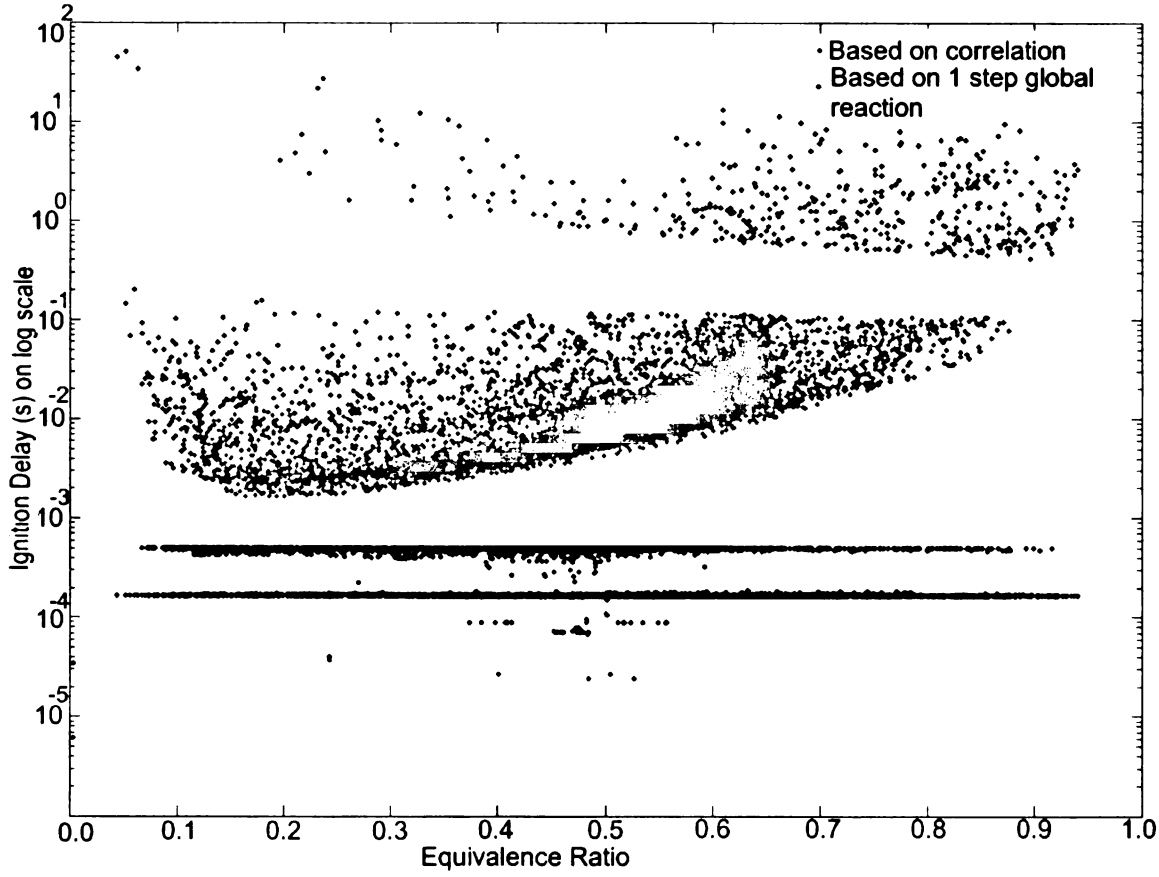

Figure 3.09 Comparison of ignition delays from two different methods

3.4.2 Ethanol Oxidation Mechanisms

Various reaction mechanisms have been developed for the oxidation of ethanol. Examples include the one step global reaction [27], and detailed multi-step mechanisms [28, 29].

3.4.2.1 Global Mechanism

Westbrook and Dryer [27] give a global reaction for the oxidation of ethanol, which represents many elementary reactions approximately:

$C_2H_5OH+3O_2 \rightarrow 2CO_2+3H_2O$

The rate of this reaction is given by

$$k_{ov} = AT^n \exp(-E_a / RT)[C_2H_5OH]^a [O_2]^b$$

where $n = 0$, $A = 1.5\times10^{12}$, $E_a = 30$ kcal/mole, $a = 0.5$, $b = 1.6$. These values have been obtained by varying the parameters such that the maximum flame speed and the equivalence ratio at which this maximum occurs, the lean and rich flammability limits and the variation of flame speed with pressure obtained from this reaction match with the experimental values.

This global reaction provides a comparatively easy way of including chemical reactions in a computational fluid dynamics code and has been used in KIVA 3V. However, it has some limitations that should be kept in mind before using it. First, it overpredicts the total extent of the reaction. It does not consider the effect of the presence of CO and H_2 in equilibrium with CO_2 and H_2O at adiabatic flame temperatures, thus giving higher values of the total heat of reaction and

adiabatic flame temperature. Similarly, it also does not consider the presence of some other species like H, O and OH, albeit in smaller amounts. KIVA overcomes this deficiency by using equilibrium reactions involving N_2, N, O_2, O, CO_2, CO, H_2O, H, H_2, and OH, as explained in Chapter 2. These reactions give the final distribution of the product while the rate of reaction is calculated by the one step equation.

Also, this one step reaction fails to take into account the fact that the fuel is first partially oxidized to CO and H_2, which are then further oxidized to CO_2 and H_2O when the fuel has been mostly consumed. This flaw can be avoided by using two reactions to first oxidize ethanol partially to CO and H_2O and then CO to CO_2:

$$C_2H_5OH+2O_2 \rightarrow 2CO+3H_2O$$

$$2CO+O_2 \rightarrow 2CO_2$$

3.4.2.2 Mechanism by Marinov

This mechanism [28] consists of 372 elementary reactions and 57 species. The mechanism has been validated for temperatures from 1000-1700 K, pressures from 1.0-4.5 atm and equivalence ratios from 0.5-2.0, by comparing the ignition delays with data from shock tubes, the laminar flame speeds with data from a combustion bomb and a counterflow twin flame, and species profiles with data from ethanol oxidation in jet-stirred and turbulent flow reactors. The mechanism takes into account the importance of the decomposition reactions of ethanol (a problem inherent in the global step reaction discussed above), the branching ratio selection for hydrogen extraction from ethanol by OH and also the reactions

of the hydroperoxyl radical.

Some studies have been performed by integrating the detailed mechanisms involving large number of reactions and species [30-36] with KIVA and other computational fluid dynamics softwares. But, such simulations are still rare due to the computational resources required and also because of the large amount of time required to run these simulations for relatively complex geometries.

If we compare the ignition delays obtained from the correlation with those obtained from the detailed mechanism of Marinov (Figures 3.10, 3.11. 3.12), we see that the ignition delays in the latter case are even higher. This indicates that even the ignition delay correlations do not successfully predict the ignition delays for engine conditions. This can be attributed to the fact that they were derived for a limited set of conditions, while the actual engine conditions have much larger variations. Thus, we can conclude that in order to properly predict the combustion process, we need to use the detailed Marinov mechanism for calculating the ignition delay times for different operating conditions. This can be done using the commercial software Chemkin^{TM} [37], which is a tool widely used for modeling complex chemical kinetics problems and provides various reactor models to solve the problem at hand.

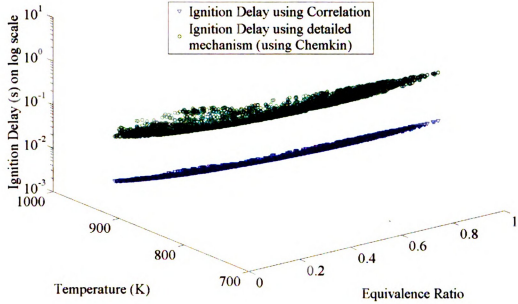

Figure 3.10 Scatter 3D Plot of Ignition Delay, Temperature and Equivalence Ratio

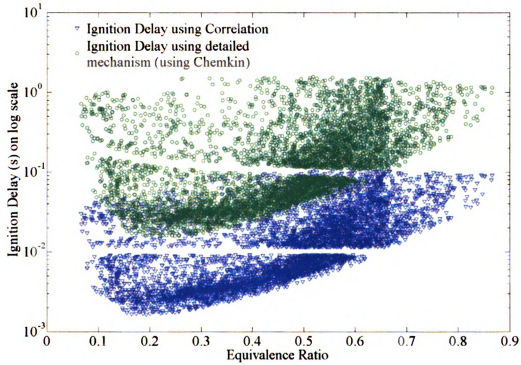

Figure 3.11 Variation of Ignition Delay with Equivalence Ratio

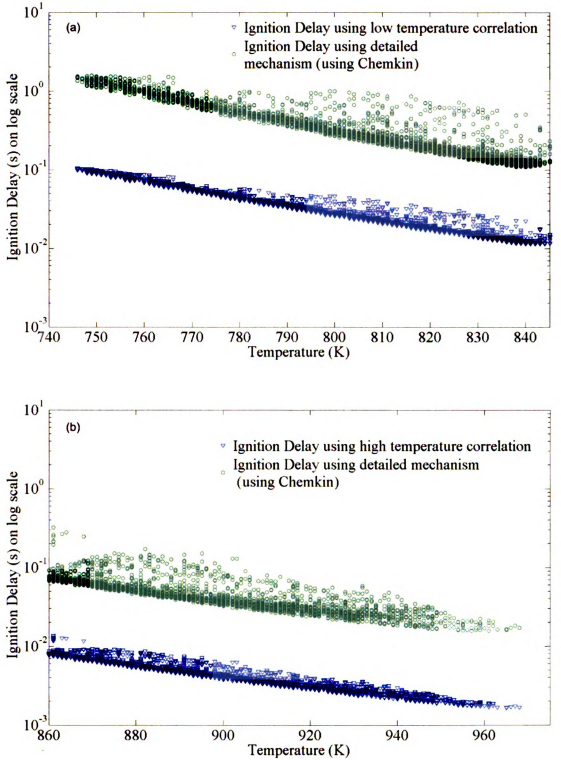

Figure 3.12 Variation of Ignition Delay with Temperature (a) using low temperature correlation (b) using high temperature correlation

3.4.3 Chemkin™ closed homogeneous constant volume 0-D reactor

Chemkin™ [37] is a commercially available software used for solving a variety of problems involving gas-phase and gas-surface chemical kinetics. It has several reactor models which can be used to simulate or solve the problem at hand. One of these reactor models is the closed homogeneous constant volume 0-D reactor, in which the contents are assumed to be well-mixed and uniform [38]. The reactor model also assumes that the mixing processes have no effect and the conversion of the reactants into products is controlled by the chemical kinetics only. This assumption leads to the use of spatially averaged or bulk properties and relatively less computationally expensive mathematical models, thus allowing large chemical mechanisms to be utilized. The governing equations of the reactor are described in detail in the Chemkin™ Theory Manual [38].

The solution of a problem requiring the use of Chemkin™ consists of three steps – preprocessing, model setup and run, and post processing [39], which are described as follows for the case of an ignition delay calculation for ethanol. The preprocessing step involves the specification of the reaction mechanism, which in case of ethanol is the Marinov mechanism, and the thermodynamic properties of the species, which are then verified for their accuracy and completeness. After the preprocessing, the cluster properties are specified. These include the type of reactor, the problem type, the reactor physical properties like temperature, pressure, volume, heat loss, heat transfer coefficient etc. and the composition of

the reactant mixture. For an ethanol ignition delay calculation, the closed homogeneous 0-D reactor is used and the energy equation is solved keeping the volume constant. For the physical properties, only the temperature, pressure and volume are input since no heat loss is assumed. The composition of the mixture is given in terms of the equivalence ratio, fuel (C_2H_5OH) and oxidizer (O_2) composition, and the expected products of combustion (CO_2, H_2O). The next step is to specify the solver settings like the time duration of the run and the maximum time step, which have to be changed for different runs depending on the physical properties and composition of the mixture. After the completion of the setup, the model is run, the output of each run being the ignition delay. There can be many criteria for the calculation of the ignition delay like the time at which the slope of the temperature profile reaches its maximum value i.e. the temperature inflection point or the time at which the maximum concentration of a product species is reached. For ethanol, the temperature inflection point criterion is used. There is also an option for running parametric studies, which enables the variation of one of the reactor physical properties or mixture composition, keeping other parameters constant, thus helping in building up a database of ignition delays.

3.4.4 Look-up table for ethanol ignition delay times

In KIVA 3V, the chemical source terms are calculated in the Lagrangian Phase, as described in Chapter 2. As their solution is decoupled from the calculation of the diffusion, acoustic and convection terms, we can assume, at each time step, each cell in the computational domain to be a closed homogeneous constant volume reactor with a given species concentration, pressure and temperature. Using these parameters, we can calculate the ignition delays associated with the conditions prevalent in a cell using the closed homogeneous constant volume 0-D reactor in Chemkin^{TM} and delay the onset of the chemical reactions in the cell by that time. In this way, we would have added an artificial ignition delay to the ignition delay predicted by the one step global reaction. Figure 3.13 shows the ignition delays calculated using the detailed Marinov mechanism for an equivalence ratio range 0.1-2.0 and temperature range 800 – 1500 K. These ignition delays have been incorporated into a look – up table in the *chem* subroutine of the KIVA code. At each time step, the subroutine looks up the ignition delay in the table based on the equivalence ratio and temperature conditions prevalent in the cell. If the ignition delay is higher than 6.67e-4 s, the subroutine skips the calculation of the chemical source terms, thus delaying the start of chemical reactions in the cell. If the ignition delay is less than 6.67e-4 s, chemical reactions start in the cell, indicating the start of the combustion

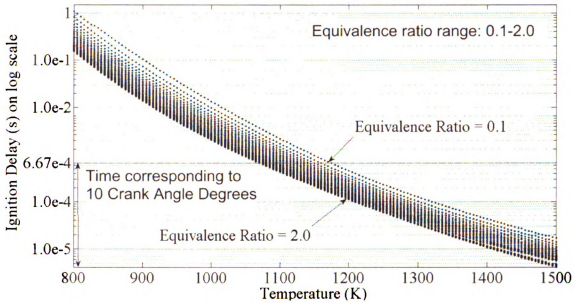

Figure 3.13 Ignition delay for Ethanol calculated using detailed Marinov Mechanism. Equivalence ratio range 0.1-2.0.

calculation. 6.67e-4 s corresponds to 10 crank angle degrees, the typical duration of the uncontrolled combustion process in an IC engine.

Figure 3.14 shows mean temperature plots for the same simulations as in Figure 3.08.

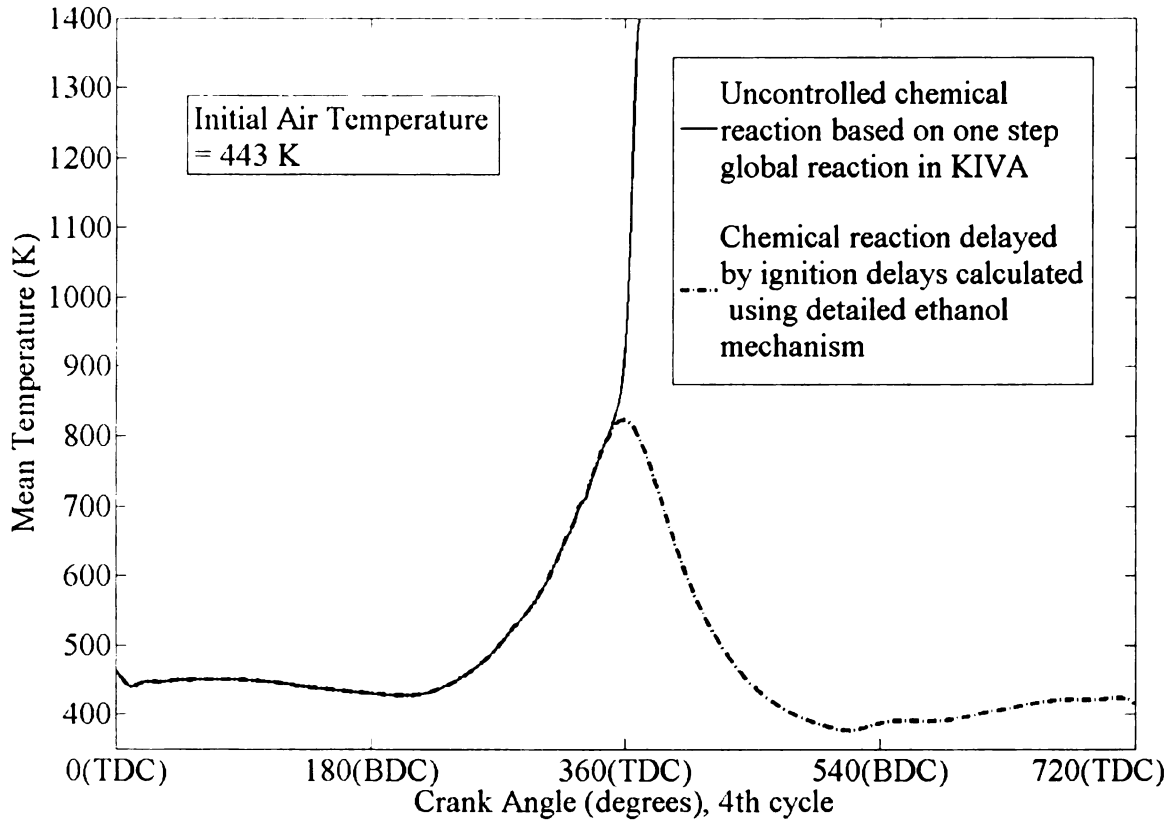

Figure 3.14 Simulations based on new combustion model

Comparison between figures 3.08 and 3.14 shows that the incorporation of the ignition delay model has resulted in the successful avoidance of the unphysical autoignition phenomenon.

Colin et al. [43] have described a similar method and have also included low temperature ignition phenomena.

3.5 Effect of Initial Conditions

For a successful simulation of the internal combustion engine process, the calculations should be free of the effect of the initial conditions and should be controlled by the boundary conditions. The effect of initial conditions wears off after a few cycles. In order to determine the cycle in which to carry out the simulations, the code was run for 20 complete cycles (figure 3.15) without addition of fuel.

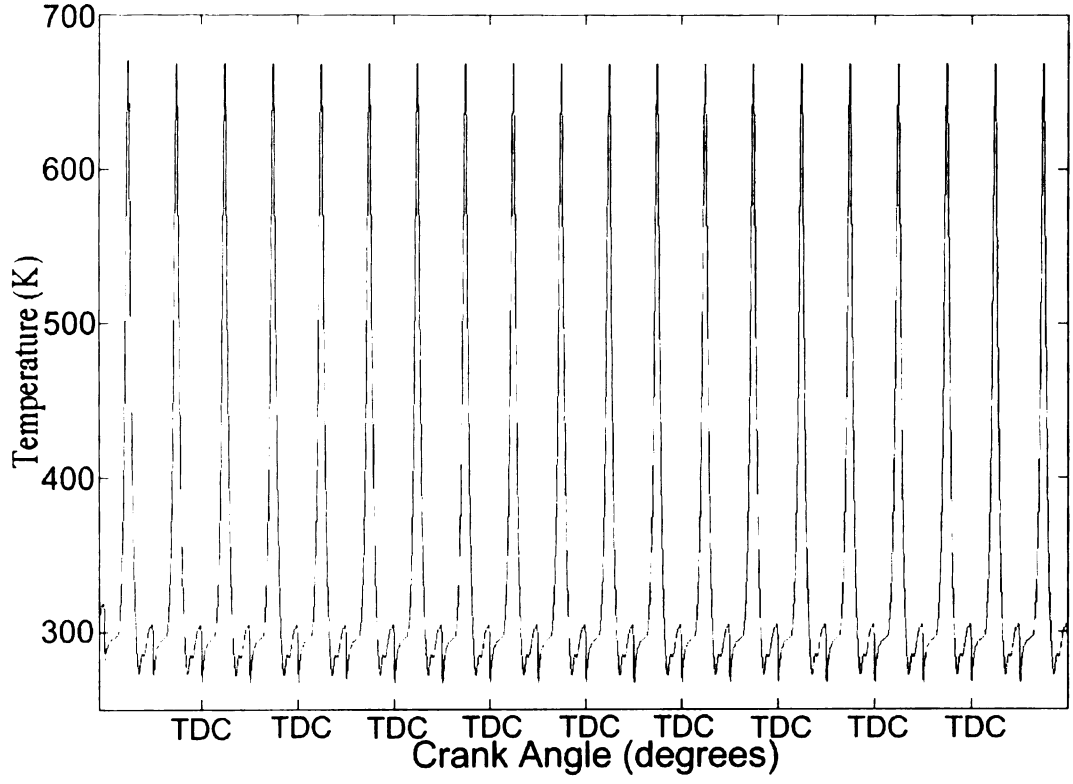

Figure 3.15 Mean temperature variation for 20 cycles without spray

On comparison of the mean temperatures in the 4th and 20th cycle (Figure 3.16), it can be seen that they match perfectly, indicating that there is no variation in the mean temperature after the 4th cycle.

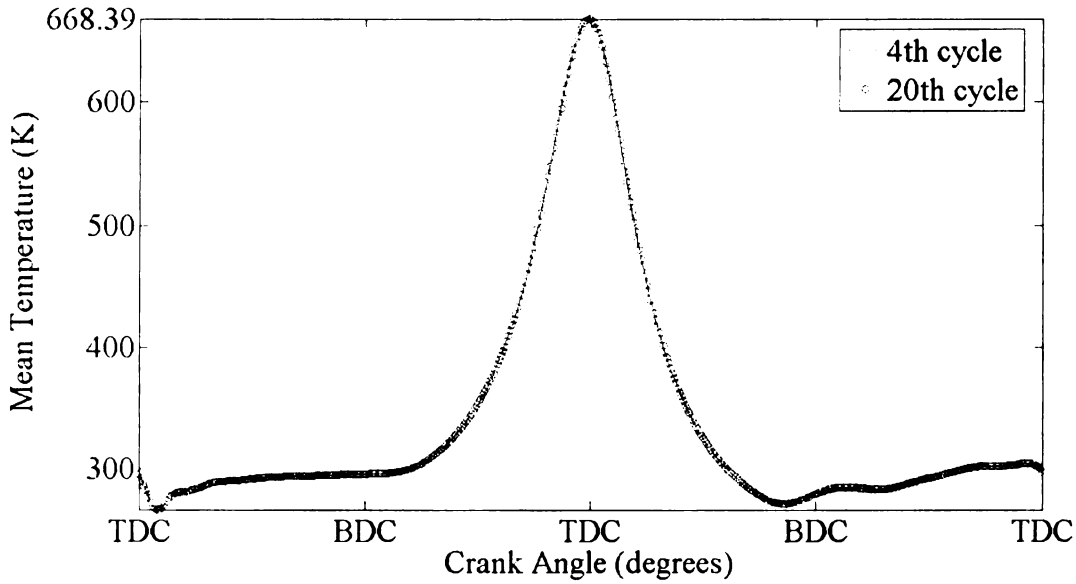

Figure 3.16 Comparison between mean temperatures for 4th and 20th cycle

Figure 3.17 shows the mean temperature variation in the cylinder for the first seven cycles for two different initial pressure conditions. After the first 180 degrees ATDC, the temperature profiles are the same for both the cases. The effect of the difference in the initial pressures is thus seen for a few degrees and simulations done in the second or later cycles would be independent of the initial conditions.

From the above it can be concluded that simulations run in the 4th cycle would give results independent of initial conditions.

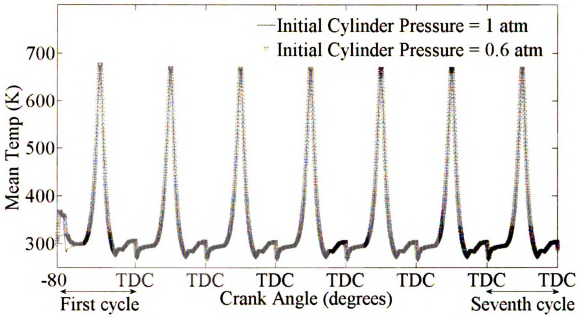

Figure 3.17 Effect of different initial conditions

CHAPTER 4

RESULTS

4.1 Streamlines

Figures 4.1, 4.2 and 4.3 show streamlines at three different cross sections.

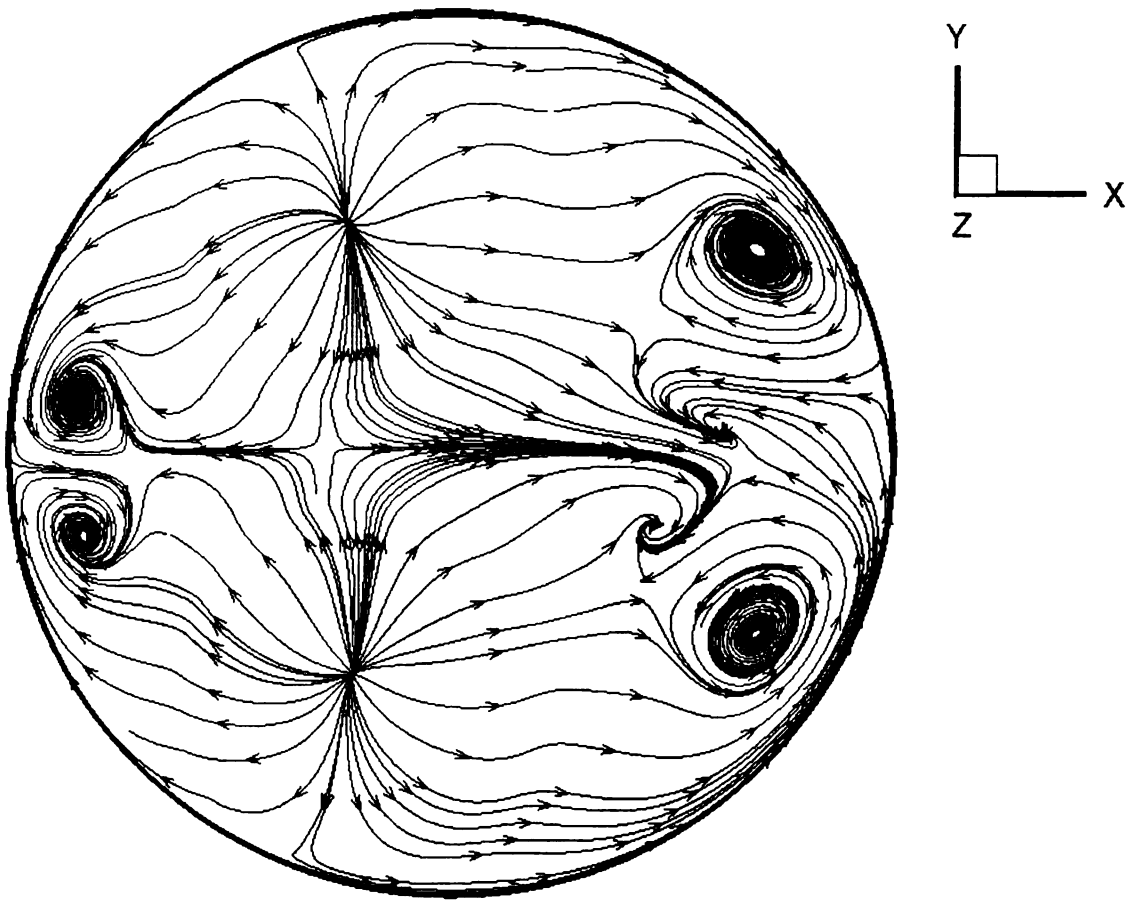

Figure 4.01 Streamlines at section z=8.35 cm

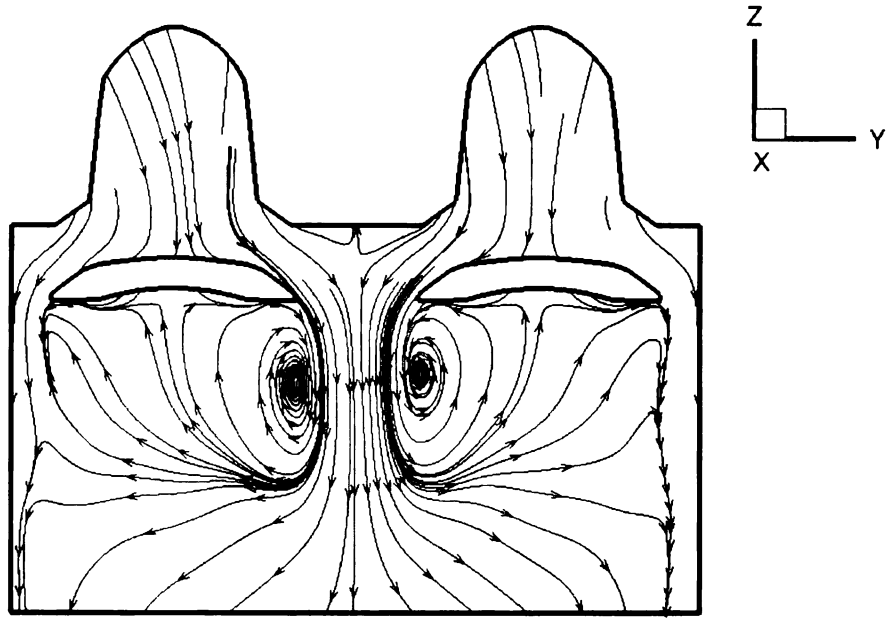

Figure 4.02 Streamlines at section x=0 cm

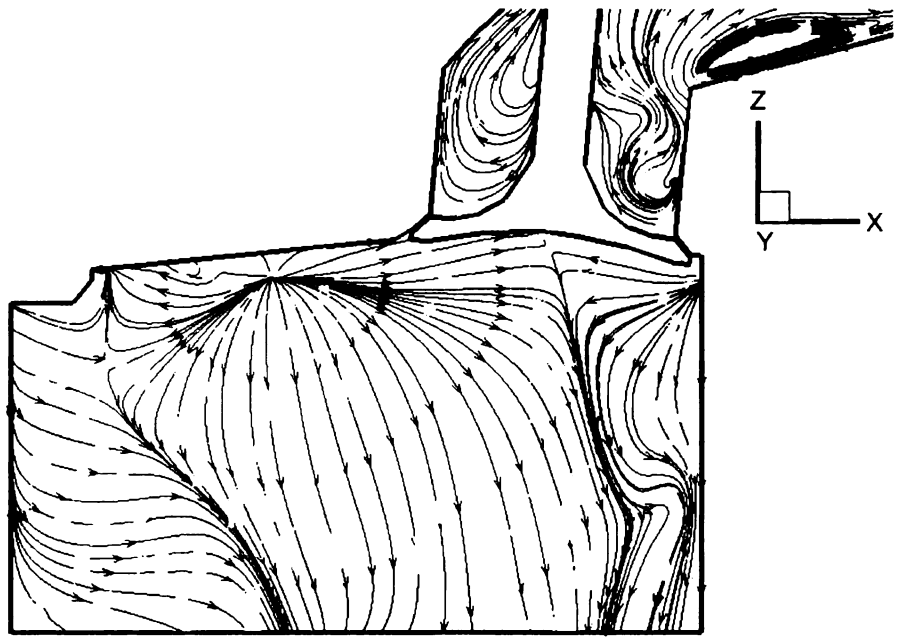

Figure 4.03 Streamlines at section y=0 cm

4.2 Comparison between gasoline and ethanol combustion

In order to compare the performance of gasoline and ethanol as fuels, simulations were run for one cycle from 2160 ATDC to 2880 ATDC. The amount of fuel injected in each case was calculated to give an equivalence ratio of 1.0 for both gasoline and ethanol in case of complete vaporization. This value was 0.046 gm/cycle for gasoline and 0.075 gm/cycle for ethanol. The initial temperature of the air was room temperature, i.e 20 deg C or 293 K. A spark was added at a crank angle of 2505 ATDC which is 15 degrees below the Top Dead Centre. Figure 4.04 compares the combustion in both the cases. As can be seen, combustion occurs in the case of gasoline and a peak temperature of approximately 2000 K is obtained, while in the case of ethanol, there is no significant combustion. Figure 4.05 compares the equivalence ratio averaged over the entire cylinder. At the instant of giving the spark, the gasoline mixture has a mean equivalence ratio of 0.564 while the ethanol mixture is very lean with a mean equivalence ratio of only 0.073. At such a low equivalence ratio, combustion of the ethanol mixture is not a possibility, even at the elevated temperatures obtained due to the spark. This illustrates the cold start problem observed in ethanol based engines.

In order to better understand the conditions prevalent in the cylinder at the point of ignition, contours of the equivalence ratio at three different cross sections are shown in figures 4.06-4.08. .

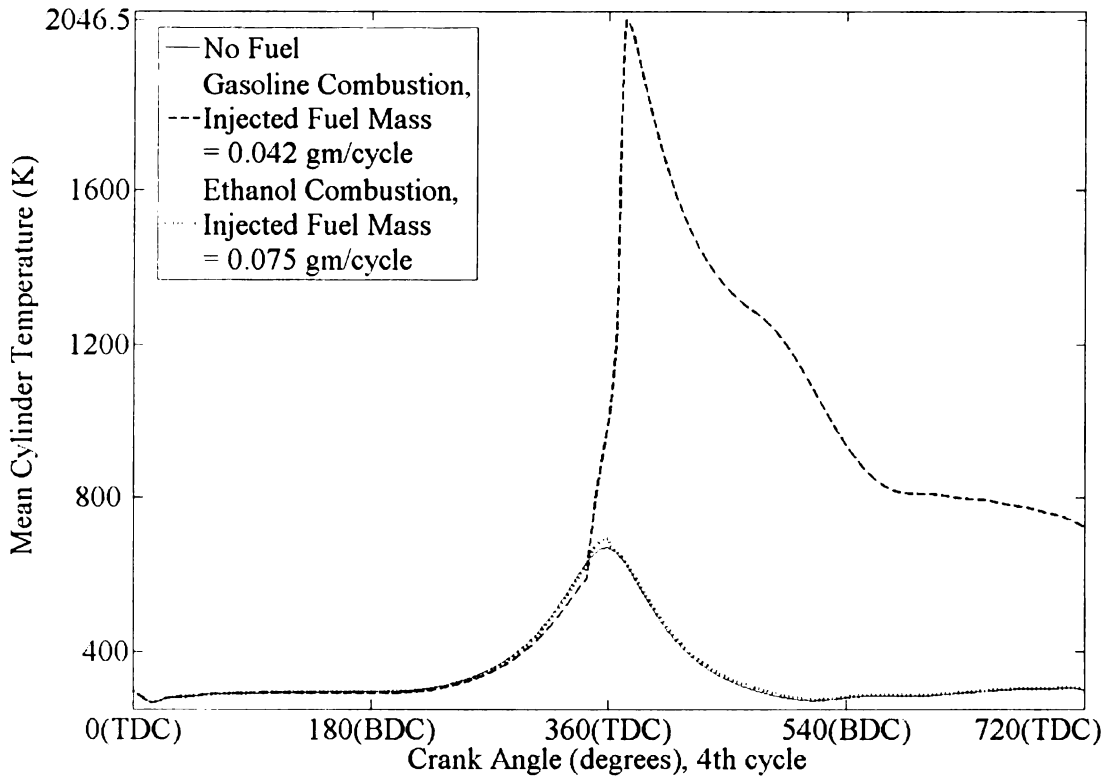

Figure 4.04 Comparison of Gasoline and Ethanol combustion

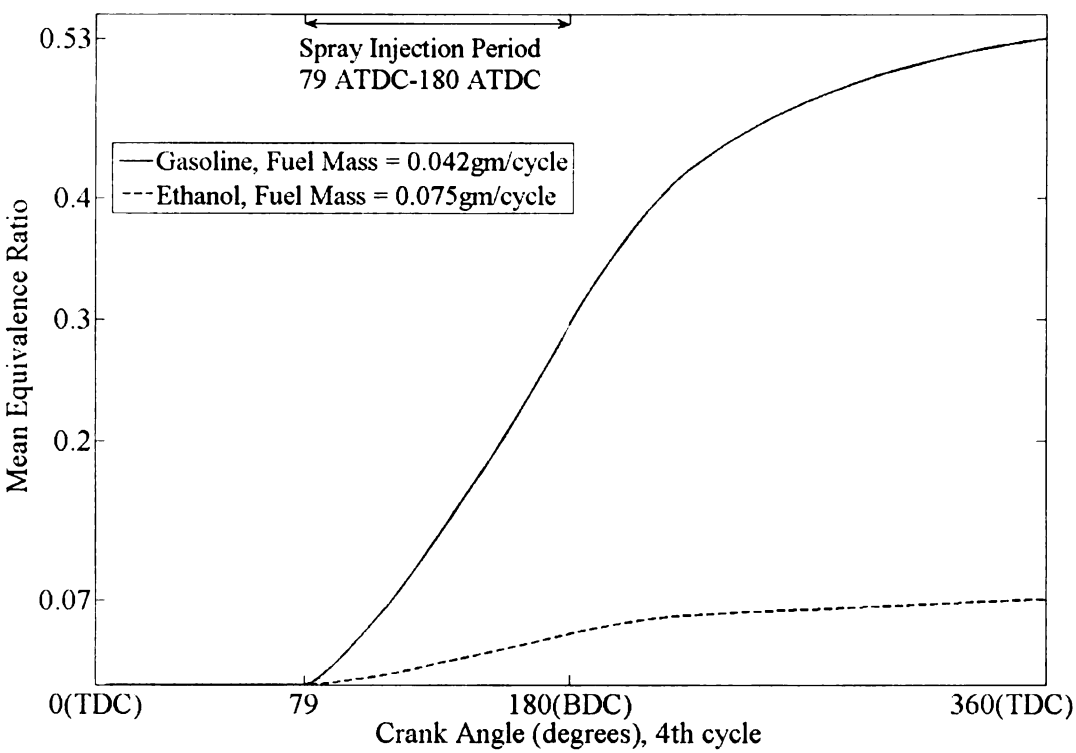

Figure 4.05 Comparison of vaporization of Gasoline and Ethanol

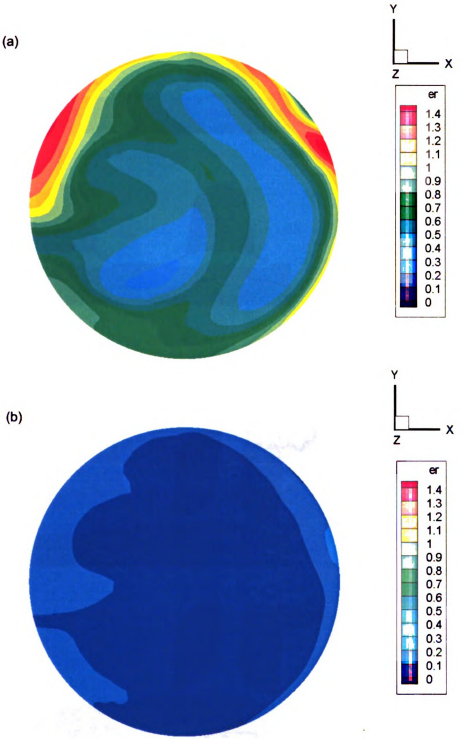

Figure 4.06 Contour Plots of Equivalence Ratio (er) at cross-section z=8.35 cm for (a) Gasoline (b) Ethanol

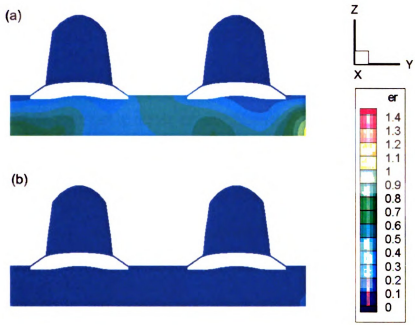

Figure 4.07 Contour Plots of Equivalence Ratio (er) at cross-section x=0 cm for (a) Gasoline (b) Ethanol

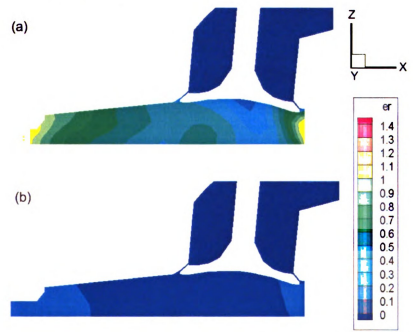

Figure 4.08 Contour Plots of Equivalence Ratio (er) at cross-section z=8.35 cm for (a) Gasoline (b) Ethanol

4.3 Effect of increasing injected fuel mass

Since injecting sufficient mass is not giving a stoichiometric mixture, a possible alternative to get a richer or stoichiometric mixture might be to inject more fuel. Figure 4.09 shows mean equivalence ratios obtained when 1.125 gm/cycle and 1.50 gm/cycle of ethanol, which would give equivalence ratios of 1.5 and 2.0, respectively, on complete vaporization, are added. Surprisingly, the mean equivalence ratio decreases further when more fuel is added. This can be explained by the local cooling effect due to spray vaporization. When the fuel is being added, there is more vaporization in the case of higher fuel mass, as can be seen in Fig. 4.09. But there is lesser evaporation after the spray period due to the thicker wall film formed in the higher fuel mass cases.

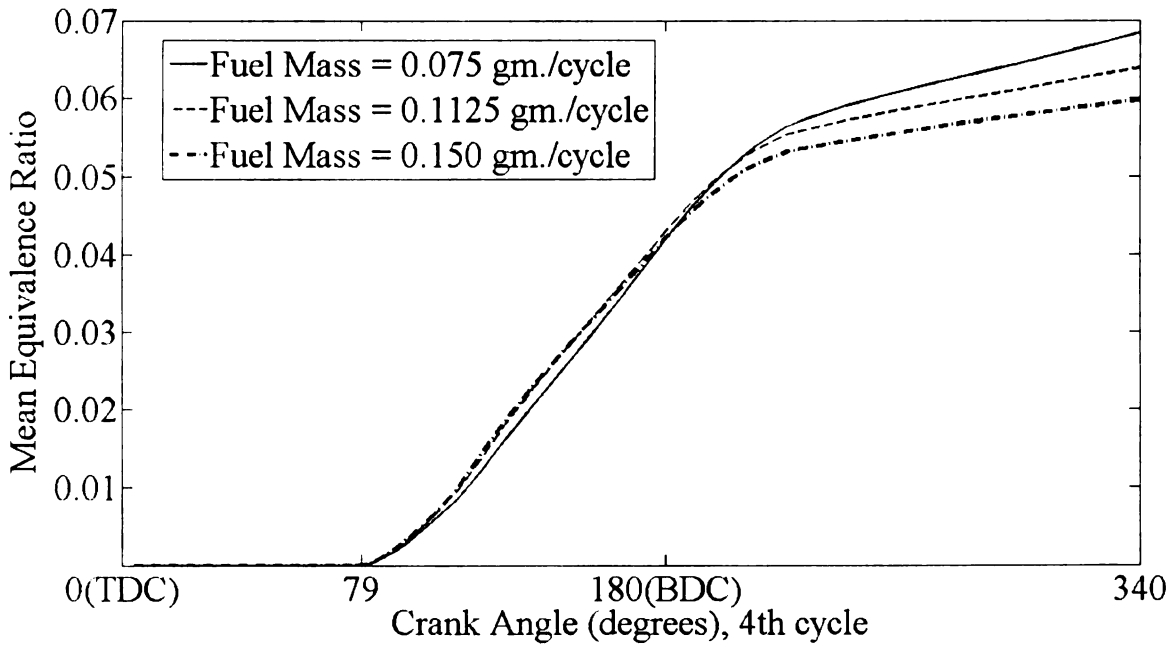

Figure 4.09 Comparison of mean equivalence ratios for different injected fuel amounts

4.4 Strategies for better vaporization of Ethanol Fuel

With an objective to increase the vaporization of ethanol in order to ensure better combustion, several strategies might be considered. Nakata et al. [6] have studied the effect of ethanol on S.I. engines and have suggested methods to improve combustion of ethanol under cold conditions. They found raising compression ratio and valve timing optimization to be useful in getting a combustible ethanol – air mixture. In the second case, an increase in air temperature is obtained due to the higher pressure difference between the intake port and cylinder and also due to an effective increase in the compression ratio due to the intake valves closing near the bottom dead center. Other possible methods include heating up the incoming fuel so that lesser energy is required for vaporization or heating up the incoming air so that more energy can be provided to the fuel for vaporization. The latter can be achieved by either directly heating up the incoming air or using a turbocharger to achieve an increase in the air pressure and a corresponding increase in the air temperature. In the following sections, the effects of these strategies on the fuel vaporization separately, and in combination with each other, would be considered.

4.4.1 Effect of heating the injected fuel

If the temperature of the injected fuel is increased, chances of better fuel vaporization exist. By heating the fuel to a higher temperature before injection

into the cylinder, the amount of heat that the cylinder gas has to provide to the fuel is reduced, thus ensuring better vaporization. deAvila et al. [40] have shown that exhaust gases can be used to vaporize the fuel completely before injection. The effect of increasing the fuel temperature by steps of 10 K on the mean equivalence ratio can be observed in Fig 4.10. The temperature of the fuel is not raised beyond 343 K as the boiling point of ethanol is 351.6 K and injecting the fuel at temperatures near this leads to instant vaporization. This causes numerical instabilities in the code and prohibitively small time steps are required during the vaporization calculation. Fig. 4.11 shows contours of equivalence ratio at the cross-section z=8.35 cm for cases with different inlet fuel temperatures.

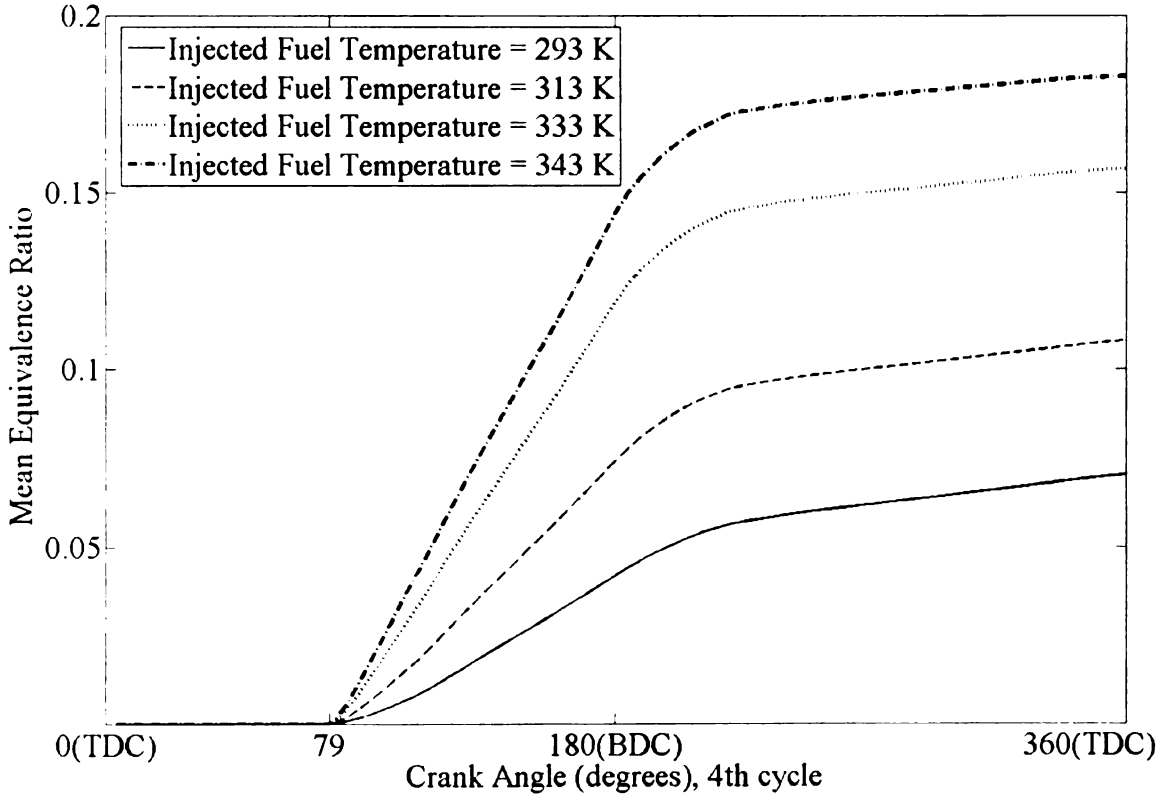

Figure 4.10 Effect of heating inlet fuel on the mean equivalence ratio

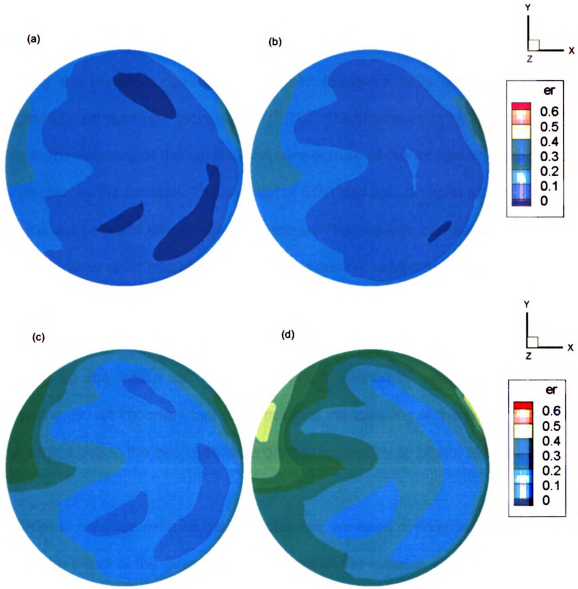

Figure 4.11 Contours of equivalence ratio (er) at cross section z=8.35 cm for inlet fuel temperature (a) 293 K, (b) 303 K, (c) 323 K, (d) 343 K

The equivalence ratio at the centre of the plane z=8.35 cm, where the spark energy would be added, is maximum for the case with inlet fuel temperature 343 K, thus indicating better chances of combustion.

4.4.2 Effect of heating incoming air

One of the methods currently being used to control NOx emissions from SI engines is exhaust gas recirculation (EGR). The decrease in NOx emissions is due to the lowering of the combustion temperature of the air fuel mixture caused by dilution by the exhaust. The concept of EGR can also be used as a strategy to aid the cold start of ethanol based engines. The exhaust can be directly mixed with the intake air or part of the exhaust gas can be used to heat up the incoming air. Since, at lower temperatures, even partial combustion of ethanol may not be possible, some quantity of gasoline may be burnt and its exhaust can be used for heating up the intake air. No matter which method is used to heat up the incoming air, an important fact to be noted is the lowering of the power output of the engine due to the decrease in air density caused by its higher temperature.

In order to simulate exhaust gas recirculation, we need to have more information about the effect of the gaseous components of the exhaust on the ignition delay of the air fuel mixture. Exhaust gas components like CO_2 are known to increase ignition delay times in internal combustion engines and an in depth study needs to be done to characterize the effect of CO_2 and other components on the ignition delay of ethanol.

In the current study, the exhaust gas recirculation has been approximated by increasing the intake air temperature, without incorporating the effect of exhaust

gas components and we should expect to see higher temperatures and better mixing.

Fig. 4.12 compares the gain in peak temperature (at Top Dead Centre) due to the higher temperature of the incoming air. As expected, the gain is highest when the air is heated by 300 degrees. Since the temperature during the intake and compression stroke is higher in the case of higher intake air temperature, we should expect a corresponding increase in the vaporization of the fuel. This expected rise can be observed in Fig 4.13.

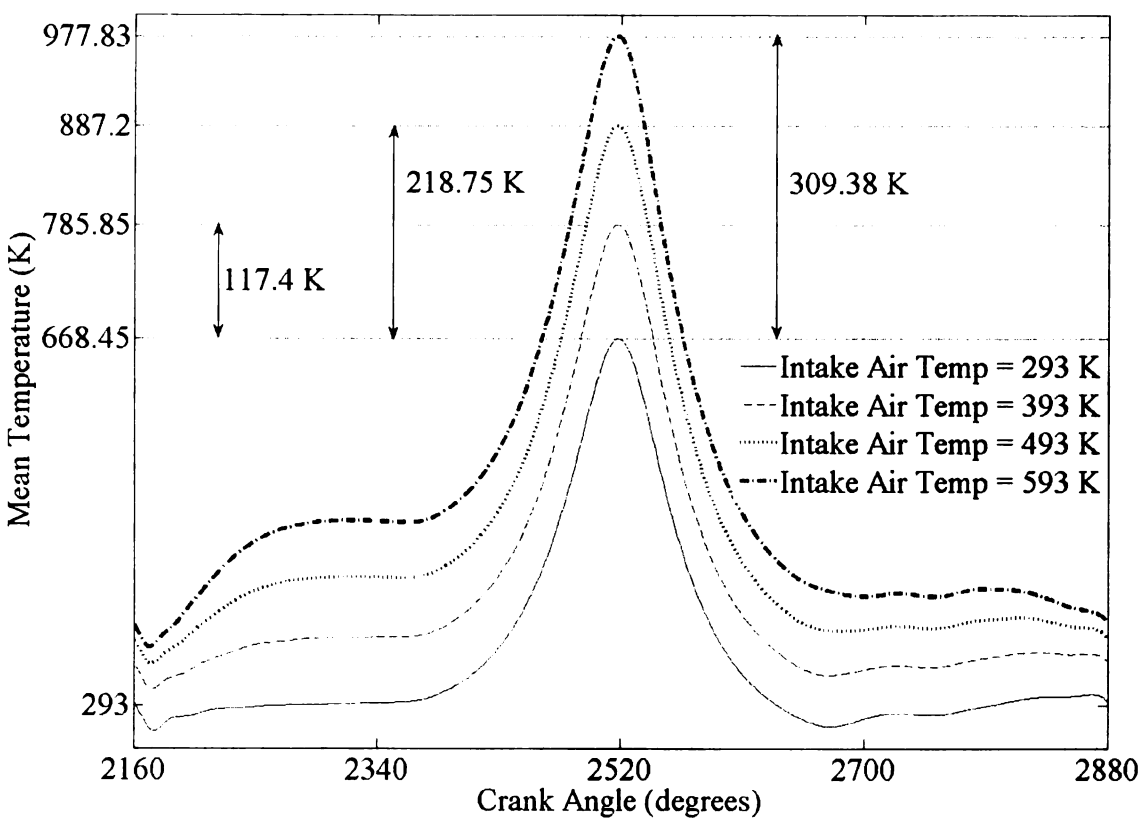

Figure 4.12 Effect of heated intake air on mean cylinder temperature

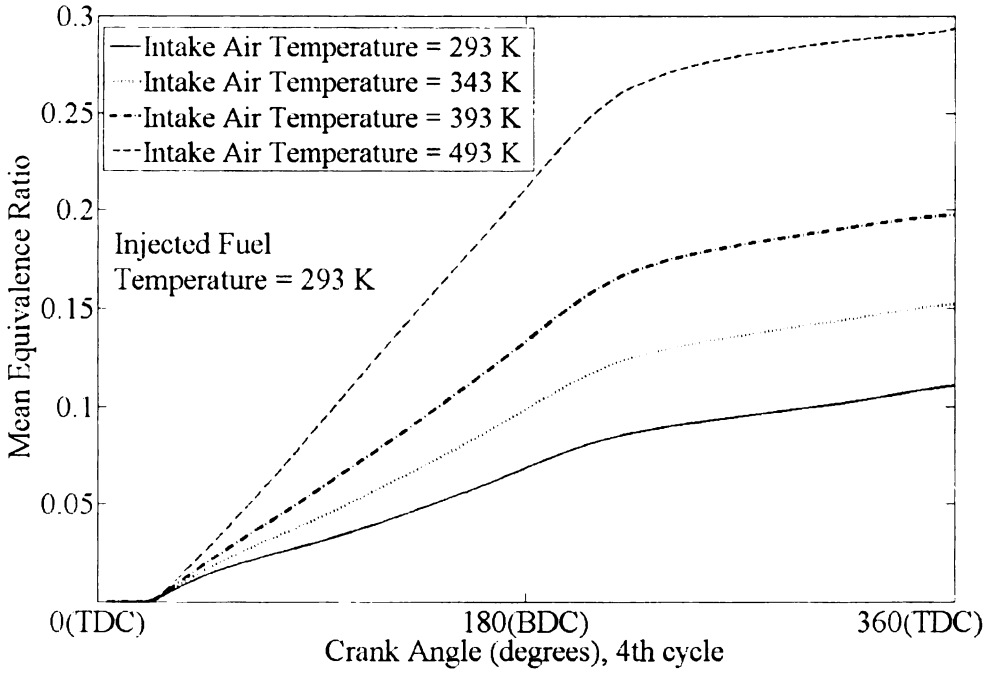

Figure 4.13 Effect of heated intake air on mean equivalence ratio

One advantage of using ethanol as a fuel is the lower range of temperatures obtained after combustion which results in reduced cooling heat loss, thus leading to higher efficiency. Besides the lower adiabatic flame temperatures of ethanol as compared to gasoline, another reason for the lower combustion temperatures is the drop in temperature caused by the high latent heat of vaporization of ethanol. This effect can be observed in Figs. 4.14-4.17, where the drop in peak mean temperature has been plotted. For the case when the intake air temperature is 293 K (fig 4.14), the drop in the mean temperature is not significant as not much evaporation is taking place due to the already low gas temperature. But as the gas temperature increases, the amount of fuel being vaporized also increases and consequently the drop in peak temperature also increases.

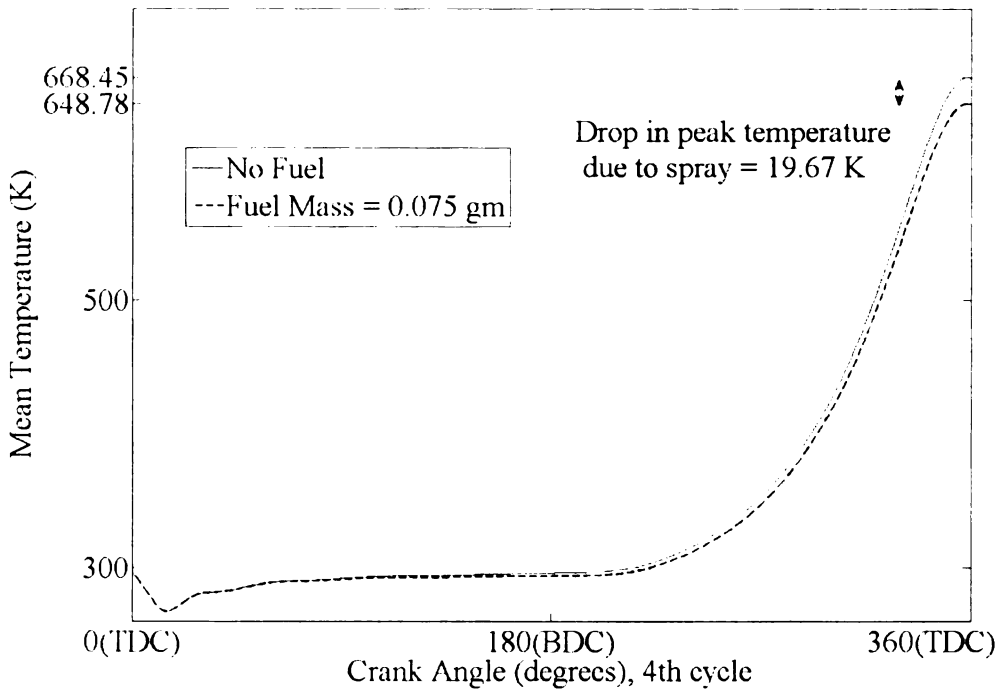

Figure 4.14 Drop in mean temperature due to fuel evaporation. Incoming air temperature 293 K

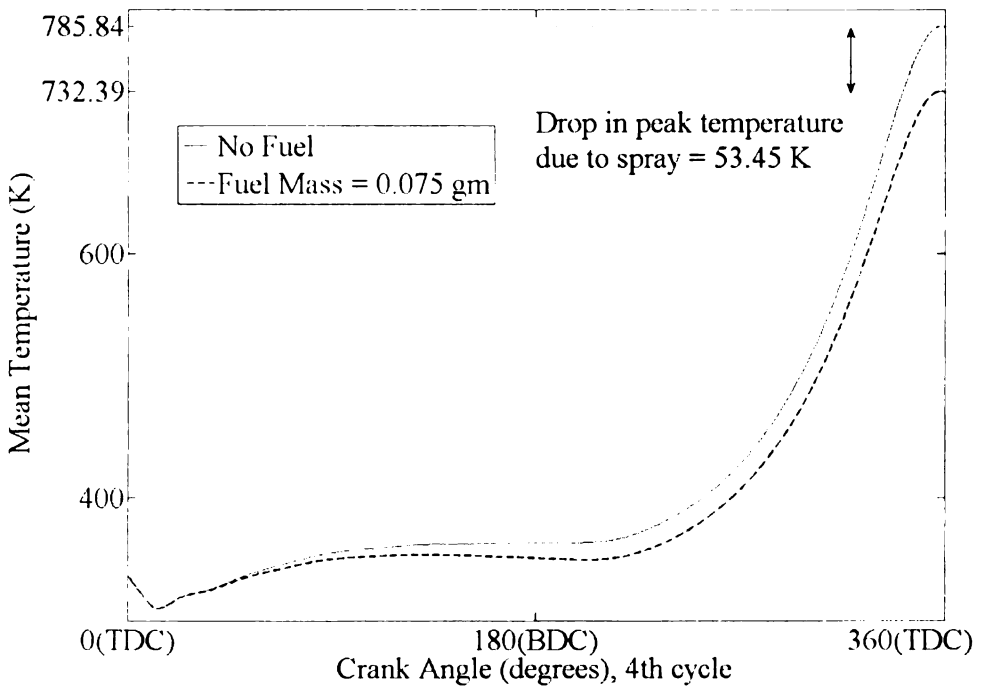

Figure 4.15 Drop in mean temperature due to fuel evaporation. Incoming air temperature 393 K

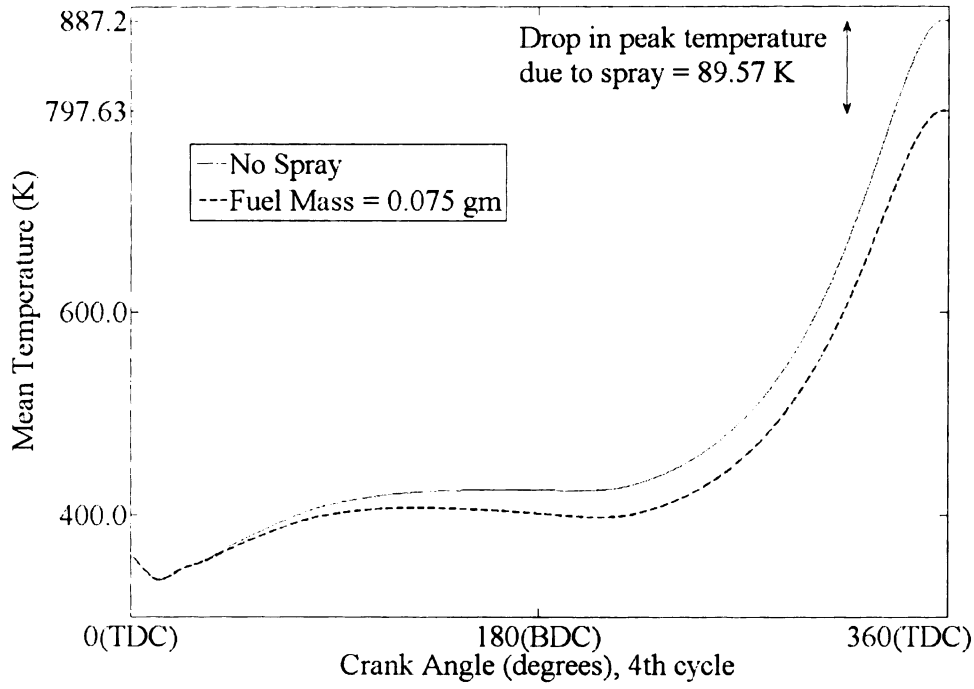

Figure 4.16 Drop in mean temperature due to fuel evaporation. Incoming air temperature 493 K

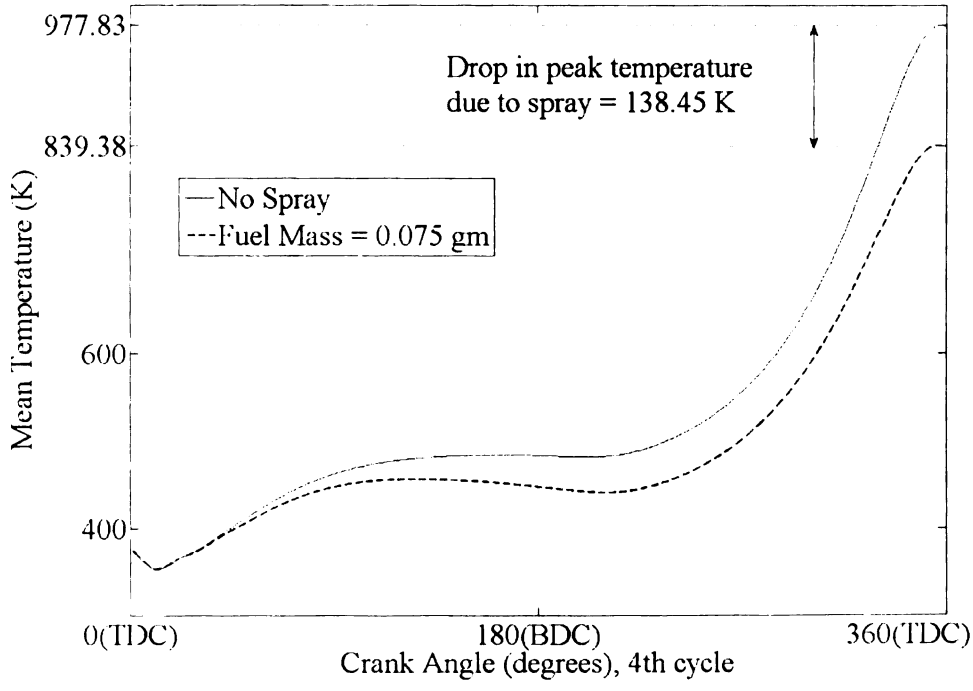

Figure 4.17 Drop in mean temperature due to fuel evaporation. Incoming air temperature 593 K

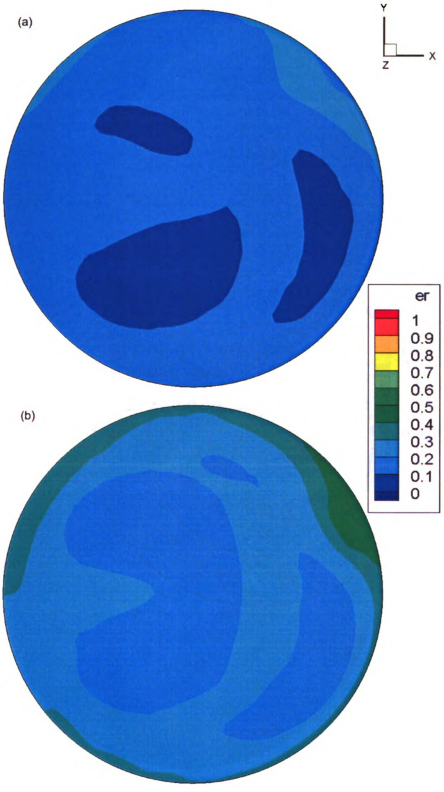

Figure 4.18 Contours of equivalence ratio (er) at cross section z=8.35 cm at CA 2505 ATDC for intake air temperature (a) 293 K, (b) 393 K

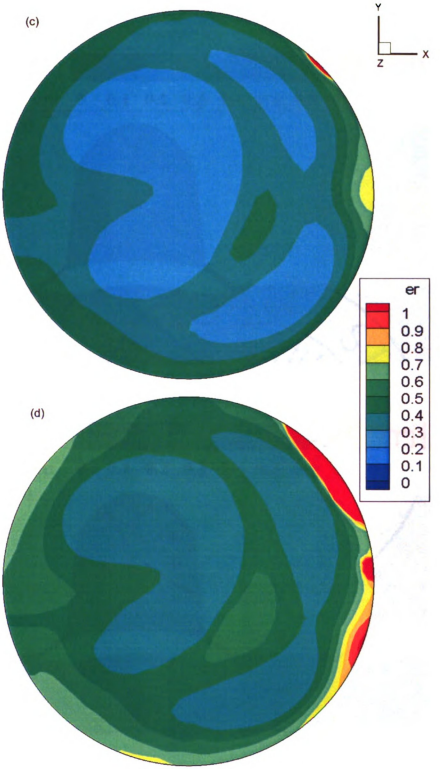

Figure 4.18 (contd.) Contours of equivalence ratio (er) at cross section z=8.35 cm at CA 2505 ATDC for intake air temperature (c) 493 K, (d) 593 K

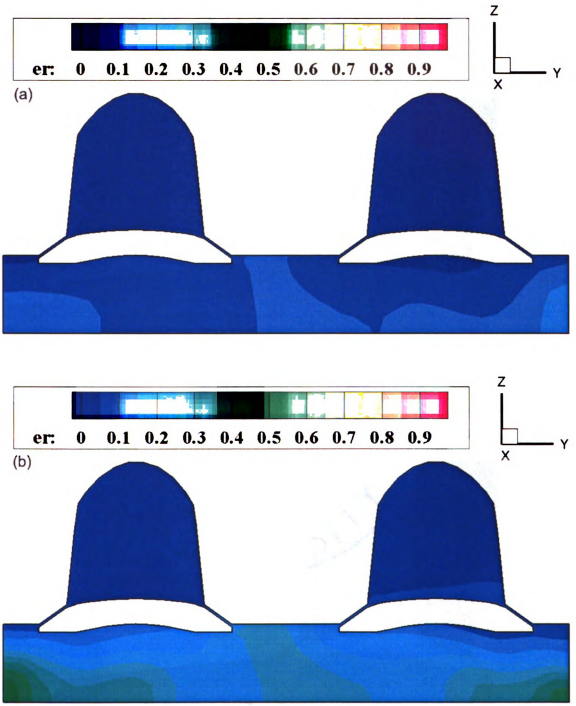

Figure 4.19 Contours of equivalence ratio (er) at cross section x=0 at CA 2505 ATDC for intake air temperature (a) 293 K, (b) 593 K

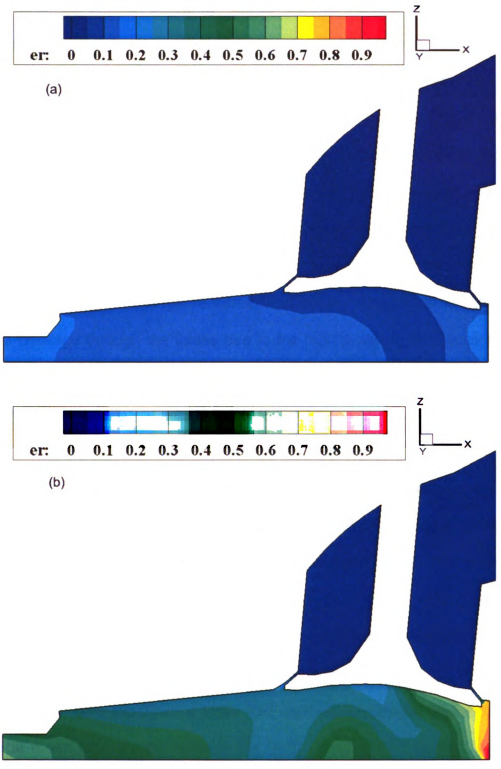

Figure 4.20 Contours of equivalence ratio (er) at cross section y=0 at CA 2505 ATDC for intake air temperature (a) 293 K, (b) 593 K

4.4.3 Effect of turbocharging

Turbocharging is generally used in gasoline SI Engines for the purpose of downsizing and at the same time maintaining adequate power [41]. The concept of turbocharging can be employed in ethanol based SI engines in order to overcome the cold start problem or to ensure better combustion. Exhaust from the engine from a previous cycle can be passed through a turbine, which in turn can be used to run a compressor which supplies air at a high pressure and temperature to the intake manifold. The air can then be cooled using an intercooler heat exchanger to increase its density. The air would again heat up in its passage through the intake due to the high pressure difference between the intake and the cylinder. Consequently, the higher temperature and pressure of the cylinder gas would lead to better fuel vaporization.

The cylinder gas temperature rise expected due to turbocharging can be seen in Fig. 4.21 where the mean temperature in the cylinder has been plotted for three different turbocharging pressures and compared with the case with no turbocharging. Typical compressors used in SI engines can provide a boost of 50-75 % to the incoming air, so we can expect to get pressures upto 1.75 atm through turbocharging. Thus, we can get a temperature rise of about 250 K, which can give significantly better fuel vaporization as can be seen in Fig 4.22. The mean equivalence ratios in Fig. 4.22 do not reflect the actual gain in fuel vaporization as the amount of air entering the cylinder also increases (Fig. 4.23) due to the higher pressure gradient between the intake and the cylinder, thus

lowering the effective equivalence ratio.

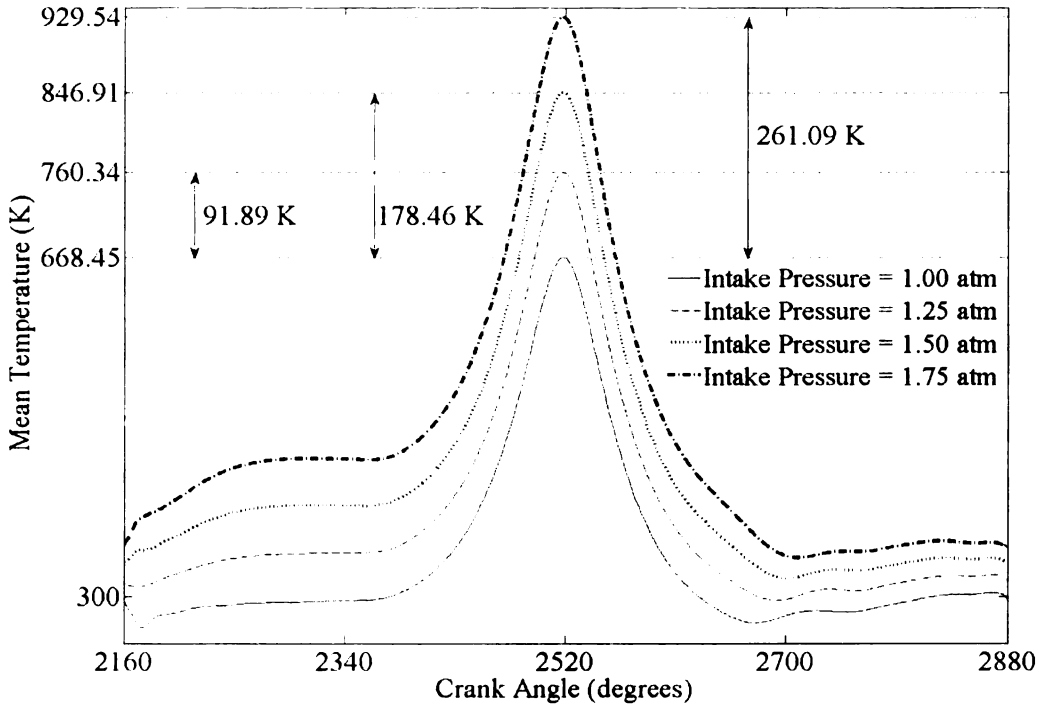

Figure 4.21 Effect of turbocharging on Mean Cylinder Temperature

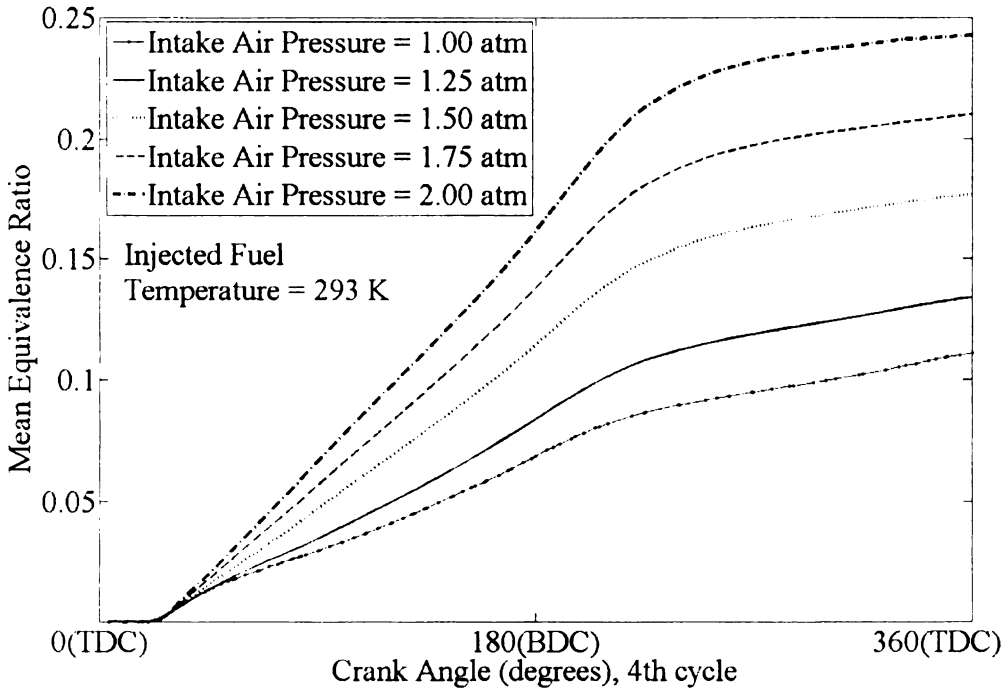

Figure 4.22 Effect of turbocharging on Mean Equivalence Ratio

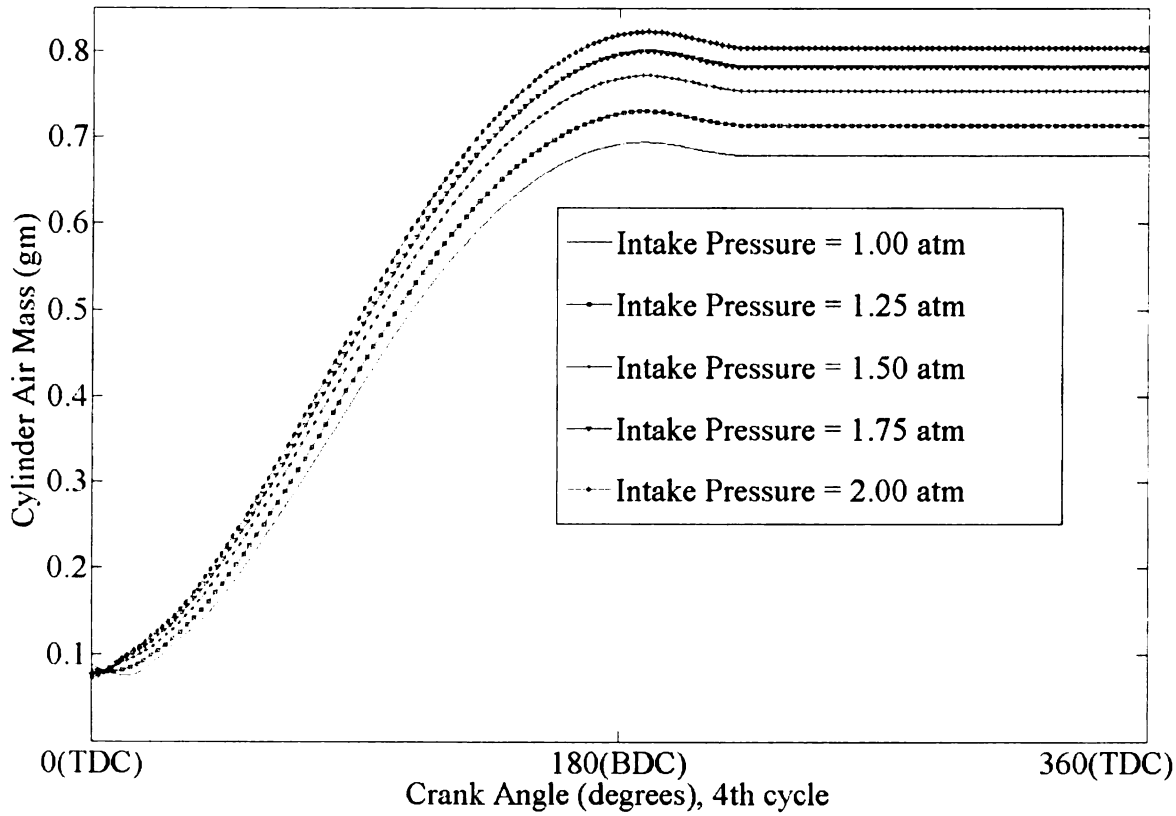

Figure 4.23 Total air mass inside the cylinder for different turbocharging pressures

The higher intake pressure in a turbocharged engine also causes more air to be drawn into the cylinder, with other parameters remaining unchanged. Thus, more fuel can be injected into the cylinder to take advantage of the extra air mass. However, since this study aims to vaporize the given amount of fuel more efficiently, the case of higher fuel mass with turbocharging has not been simulated.

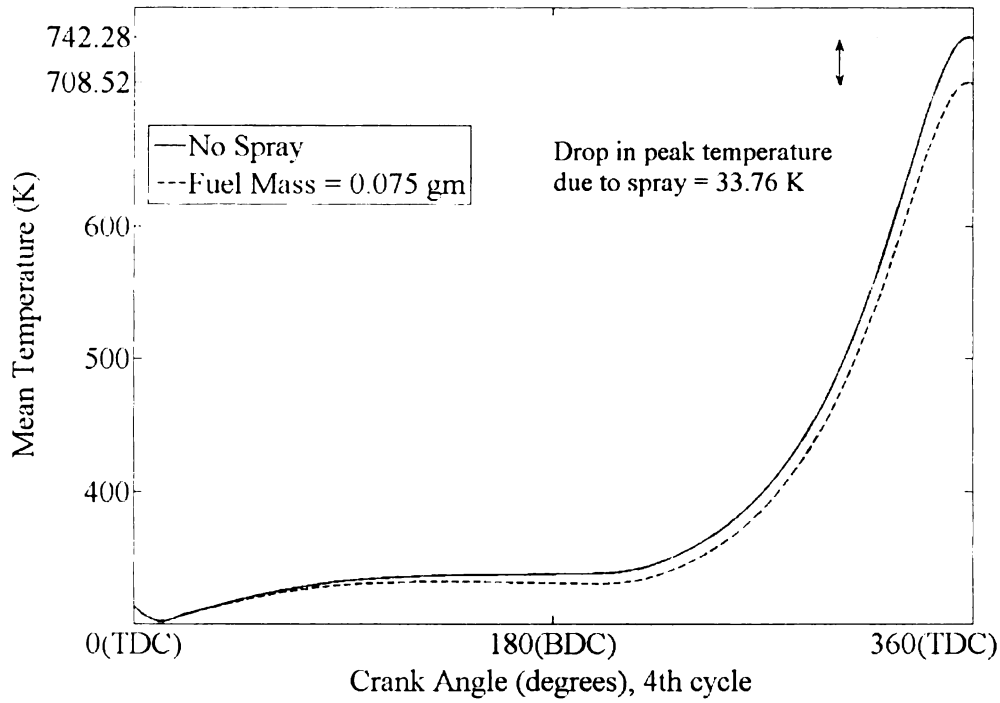

Figure 4.24 Drop in mean temperature due to fuel evaporation. Intake Pressure = 1.25 atm

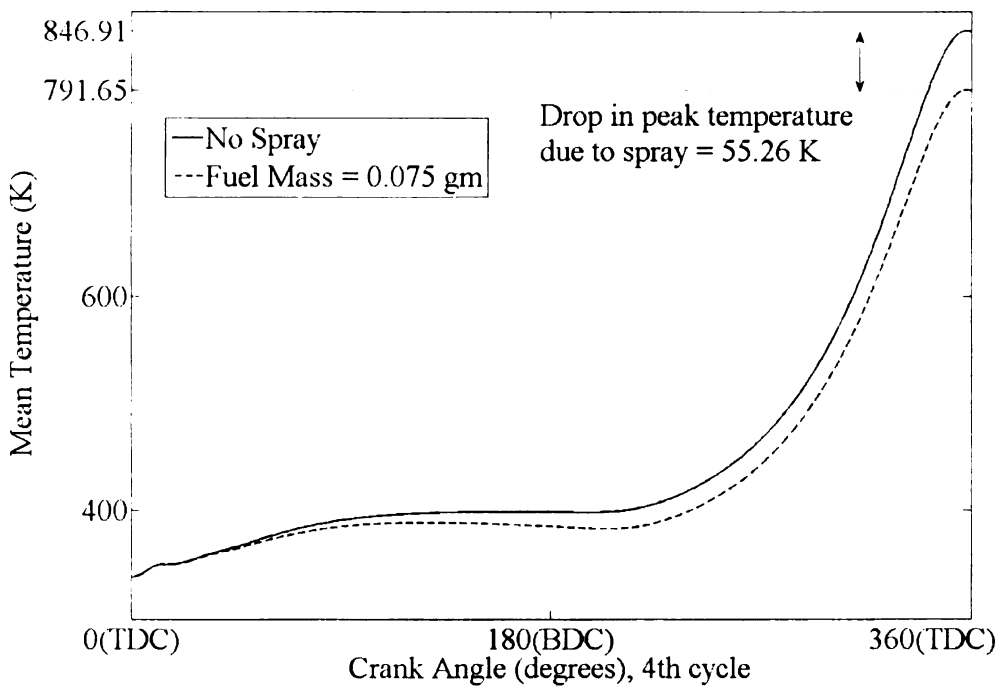

Figure 4.25 Drop in mean temperature due to fuel evaporation. Intake Pressure = 1.50 atm

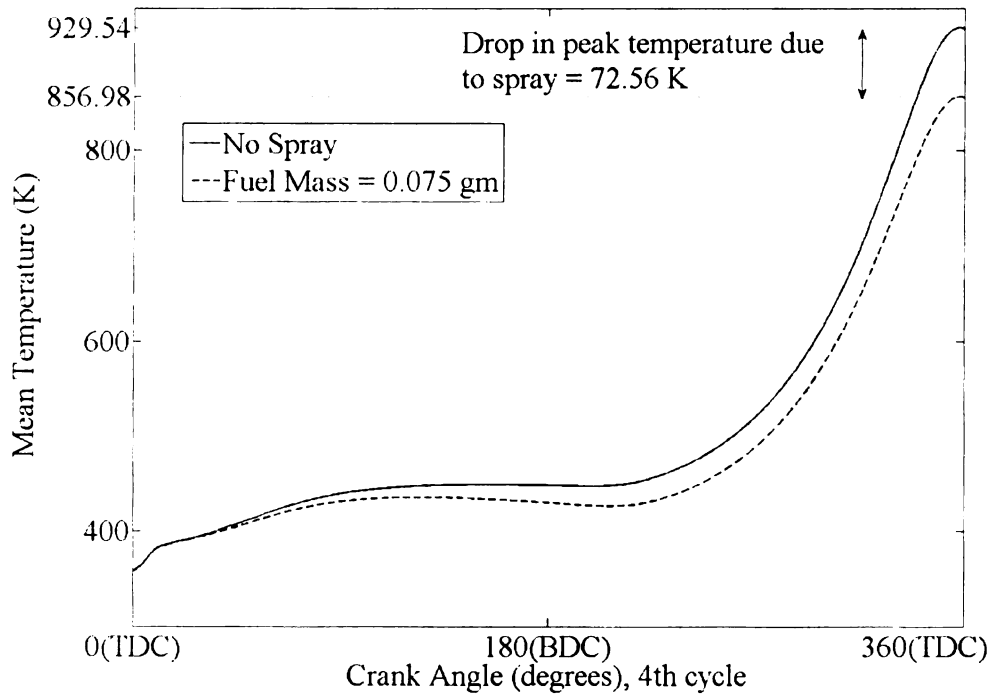

Figure 4.26 Drop in mean temperature due to fuel evaporation. Intake Pressure = 1.75 atm

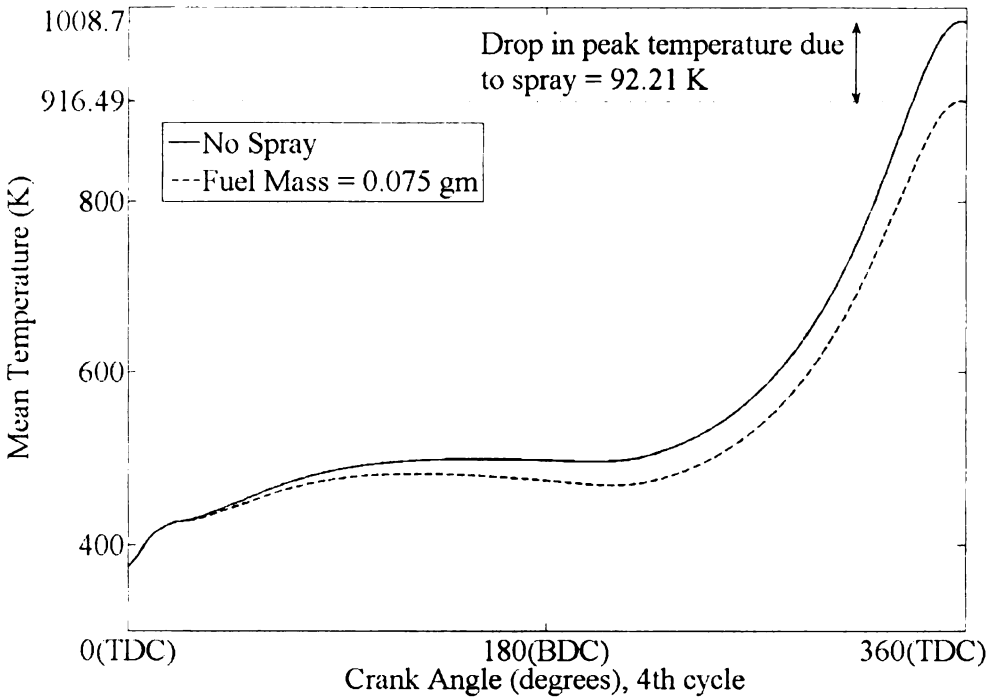

Figure 4.27 Drop in mean temperature due to fuel evaporation. Intake Pressure = 2.00 atm

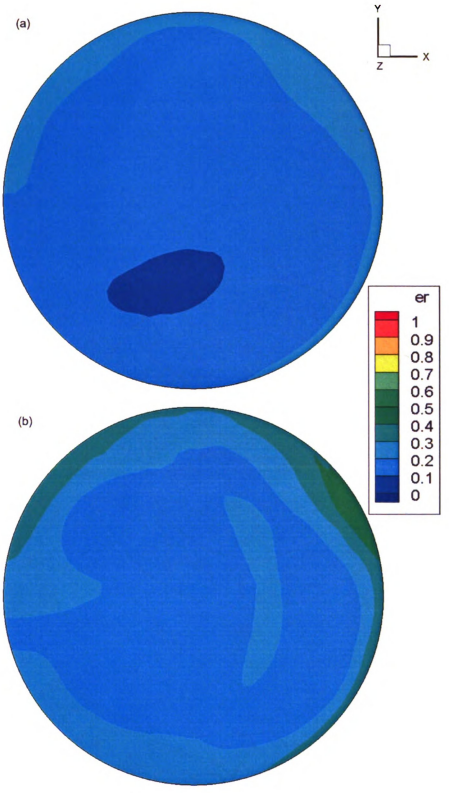

Figure 4.28 Contours of equivalence ratio (er) at cross section z=8.35 cm at CA 2505 ATDC for intake air pressure (a) 1.25 atm, (b) 1.50 atm

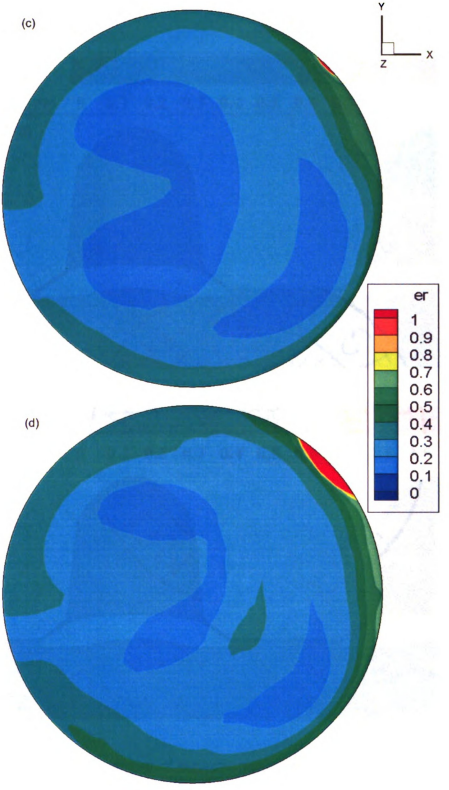

Figure 4.28 (contd.) Contours of equivalence ratio (er) at cross section z=8.35 cm at CA 2505 ATDC for intake air pressure (c) 1.75 atm, (d) 2.00 atm

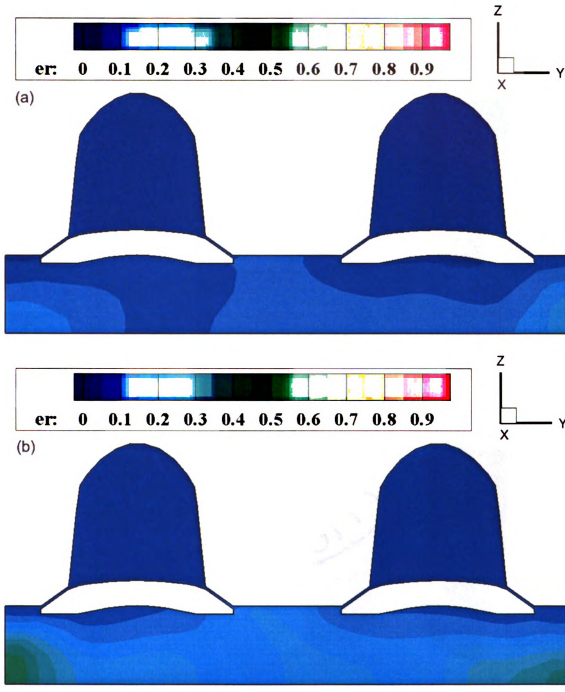

Figure 4.29 Contours of equivalence ratio (er) at cross section x=0 at CA 2505 ATDC for intake air pressure (a) 1.25 atm, (b) 2.00 atm

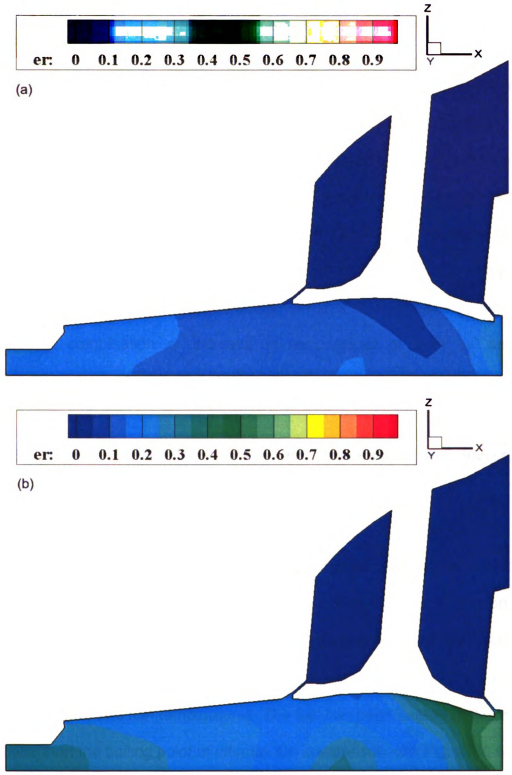

Figure 4.30 Contours of equivalence ratio (er) at cross section y=0 at CA 2505 ATDC for intake air pressure (a) 1.25 atm, (b) 2.00 atm

4.5 Combined strategies for better vaporization of ethanol fuel

The strategies discussed above may be combined to get even better fuel vaporization. As we have seen in the previous three sections, increasing the fuel temperature, heating the intake air and turbocharging, help in better vaporization of ethanol droplets. But, it is desirable to achieve even better evaporation to get a combustible mixture. While it may not be possible to increase both intake temperature and pressure at the same time as both would require large amounts of heat, with only exhaust gases being our major source of energy, we can either have a combination of increase in temperature of both air and fuel or turbocharging and increase in fuel temperature.

4.5.1 Effect of increased intake air temperature and increased fuel temperature

Part of the exhaust being used for heating intake air can also be used to heat the fuel itself. The ratio of heat transferred to the intake air and heat supplied to the fuel to raise its temperature can be optimized to give the best possible evaporation. Fig. 4.31 shows the mean equivalence ratios for simulations with increased air and fuel temperatures. The fuel has been heated to 343 K, which is lower than the boiling point of ethanol. On comparison with Fig. 4.12, we find that heating up the fuel has led to significantly better vaporization e.g. in the case of intake air temperature 393 K, the mean equivalence ratio has increased by 65 %

compared to its value when only the intake air was heated. Figures 4.32, 4.33 and 4.34 show contour plots of equivalence ratio at three different cross sections. Some regions with a local equivalence ratio of 1.0 or higher can be observed.

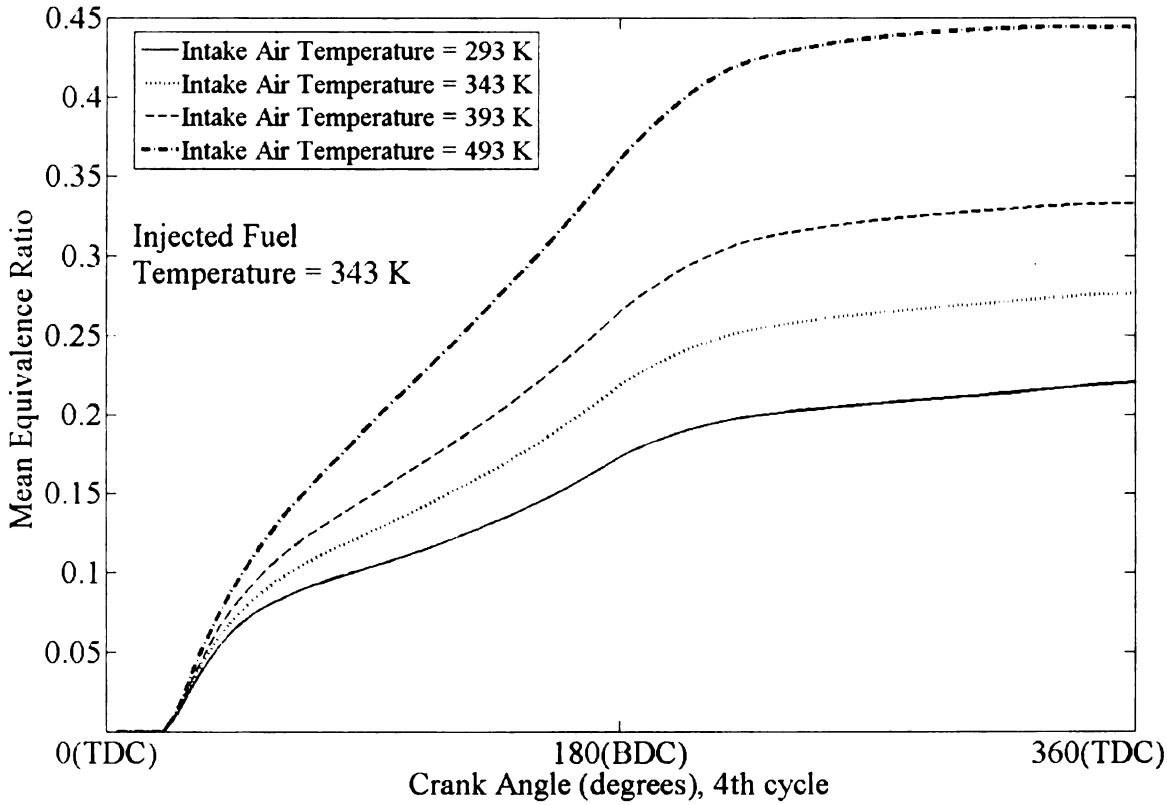

Figure 4.31 Effect of heated intake air on mean equivalence ratio. Injected Fuel temperature = 343 K

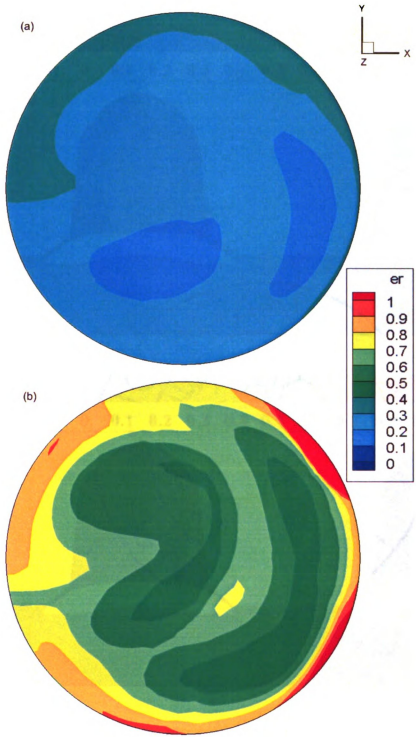

Figure 4.32 Contours of equivalence ratio (er) at cross section z=8.35 cm at CA 2505 ATDC for intake air temperature (a) 293 K, (b) 593 K. Inlet fuel temperature 343 K

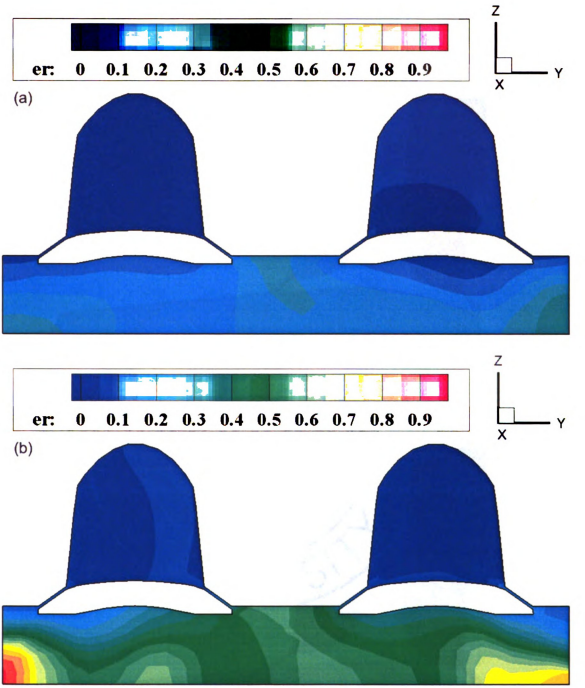

Figure 4.33 Contours of equivalence ratio (er) at cross section x=0 cm at CA 2505 ATDC for intake air temperature (a) 293 K, (b) 593 K. Inlet fuel temperature 343K

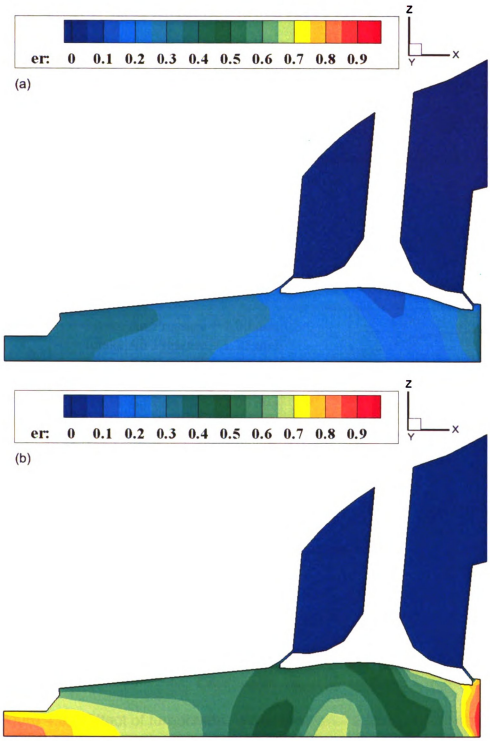

Figure 4.34 Contours of equivalence ratio (er) at cross section x=0 cm at CA 2505 ATDC for intake air temperature (a) 293 K, (b) 593 K. Inlet fuel temperature 343K

4.5.2 Effect of turbocharging and increased fuel temperature

Similar to the combined effect of heated intake air and fuel, the effect of turbocharging and heated fuel also leads to a more combustible mixture. Again, deeper analysis can give insight into which combination of turbocharging and fuel temperature would give us a better mixture.

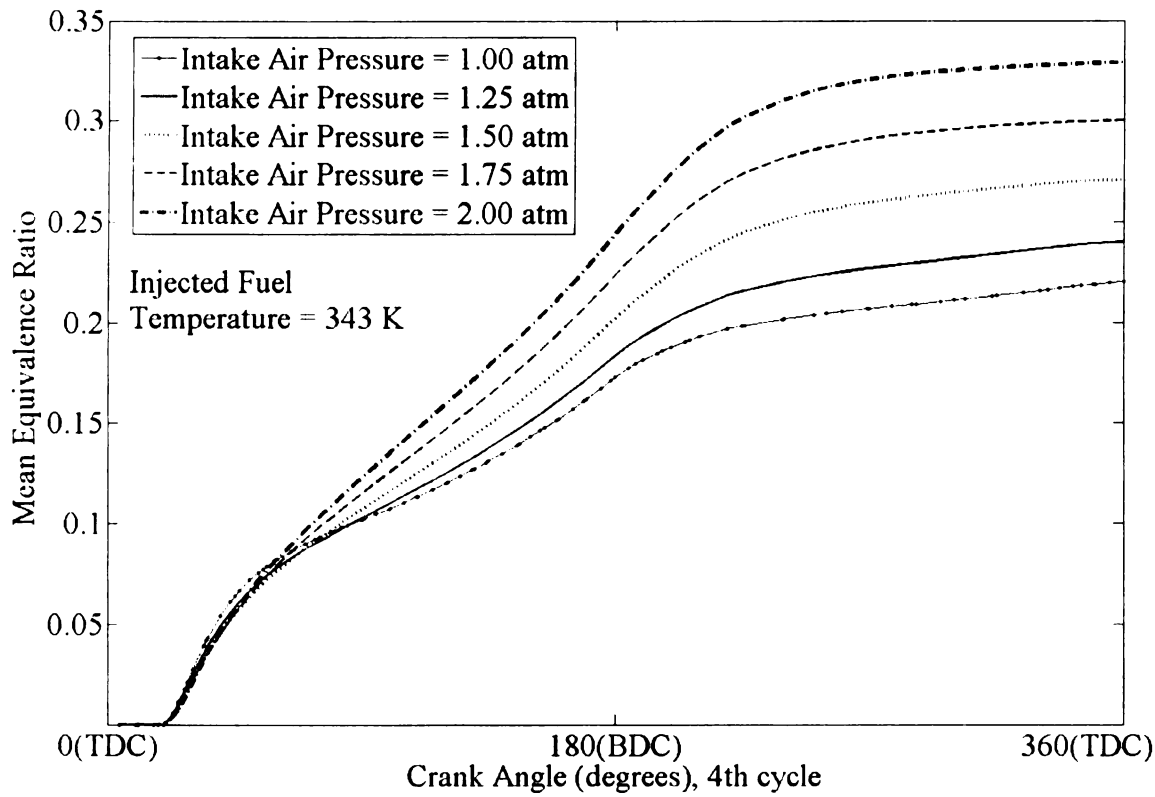

Figure 4.35 Effect of turbocharging on mean equivalence ratio. Injected Fuel temperature = 343 K

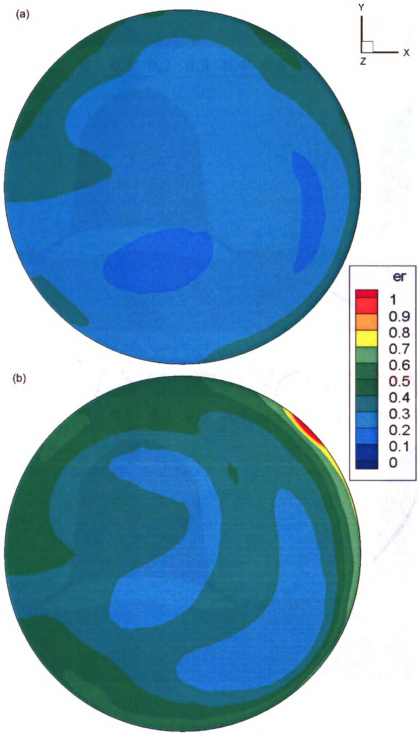

Figure 4.36 Contours of equivalence ratio (er) at cross section z=8.35 cm at CA 2505 ATDC for intake air pressure (a) 1.2 atm, (b) 2.0 atm. Injected fuel temperature 343 K

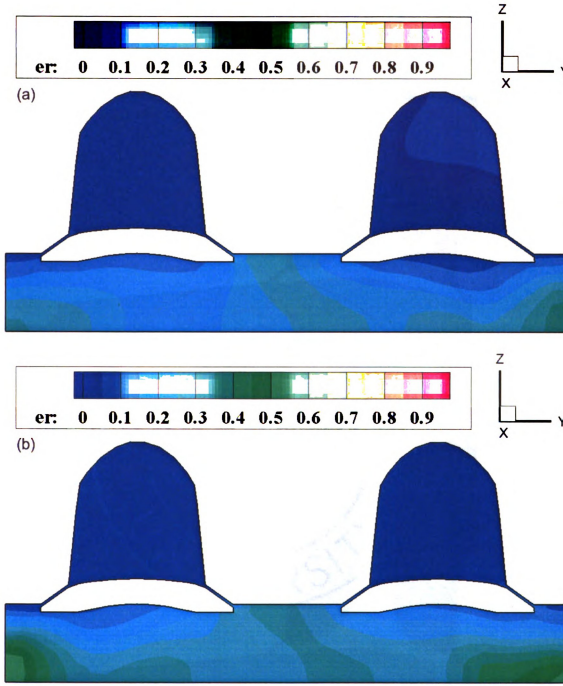

Figure 4.37 Contours of equivalence ratio (er) at cross section z=8.35 cm at CA 2505 ATDC for intake air pressure (a) 1.2 atm, (b) 2.0 atm. Injected fuel temperature 343 K

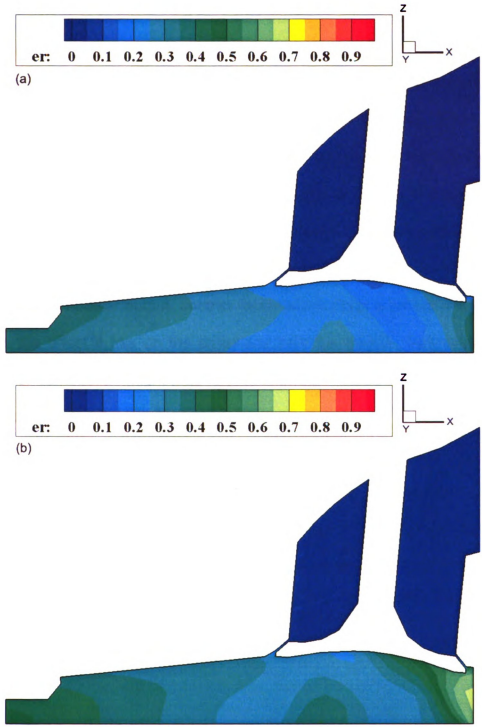

Figure 4.38 Contours of equivalence ratio (er) at cross section z=8.35 cm at CA 2505 ATDC for intake air pressure (a) 1.2 atm, (b) 2.0 atm. Injected fuel temperature 343K

4.6 Effect of spark timing on combustion

The optimum timing of the spark in a spark ignition engine depends a lot on the gas-exchange process, fuel-air mixing, compression ratio, spark plug location, combustion chamber design, flame speed, burn rate of the fuel and many other factors. In order to get the maximum amount of energy from the burnt fuel, the timing of the spark should be such that the cylinder pressure peaks in the minimum possible crank angle degrees after the top dead centre. Besides getting maximum power output, another factor which plays a critical role in spark timing is the effect it has on the emissions from the engine. Very high temperatures after combustion might lead to production of NOx by the thermal mechanism or the extended Zeldovich mechanism.

Li et al. [42] tested the effect of spark timing on the combustion of ethanol in an air cooled, four stroke, spark ignited engine for motorcycles and found that delaying the spark timing by a few crank angle degrees leads to a decrease in HC emissions and an even greater decrease in NOx, whereas the decrease in power output is comparatively lesser.

While it may not be possible to give spark timing guidelines for all engine configurations and all operating conditions, computer simulations can help us choose spark timings for a specific engine at given operating conditions. Figures 4.39-4.45 show the effect the timing of the spark has on combustion. In the case

of intake air temperature of 393 K (Figure 4.39) , sparking at CA 10° BTDC gives better combustion, while further advancing the spark leads to poorer combustion. For air intake temperature 493 K (Figure 4.40), sparking at CA 10° BTDC gives good combustion but with higher exhaust temperature, thus decreasing the efficiency. Sparking at CA 15° BTDC gives the best combustion with lower exhaust temperature, while further advancing the spark gives poorer combustion. Again, for air intake temperature 593 K (Figure 4.41), sparking at CA 15° BTDC gives the best combustion. Further advancing the spark gives poorer combustion while retarding the spark gives does not have much effect on combustion.

Similar observations can be made for spark timing in the case of higher intake pressure. Sparking at CA 15° BTDC gives the best combustion, further advancing or retardation of the spark leads to poorer combustion, although there is not much difference in the mean peak combustion temperature. One notable exception is the case of intake air pressure 1.20 atm, where advancing the spark to CA 20° BTDC gives the best combustion.

An important factor to be kept in mind in the above discussion is that the results are only for specific operating conditions. Generally, for proper electronic control of spark timing, a more comprehensive map is used, with different engine speeds being one of the parameters.

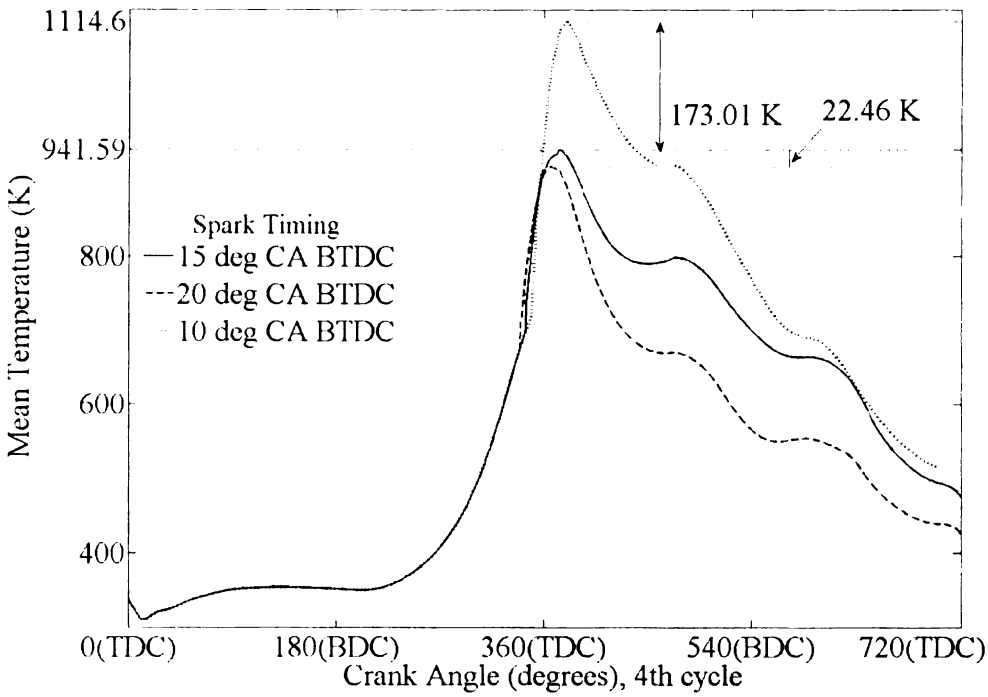

Figure 4.39 Effect of spark timing on combustion: Intake air temperature 393 K, fuel temperature 293 K

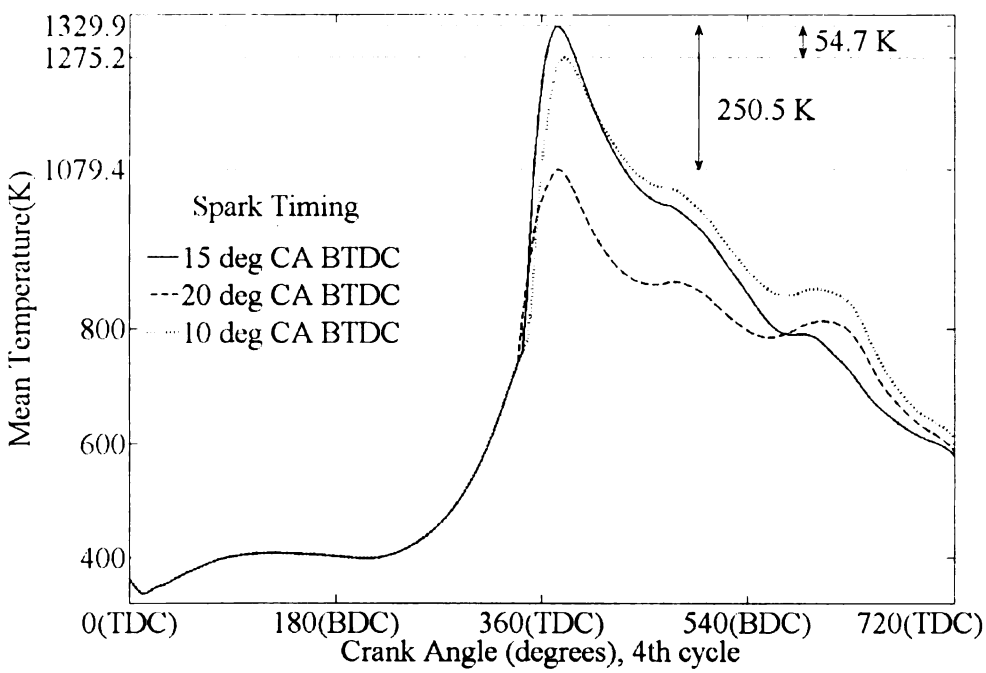

Figure 4.40 Effect of spark timing on combustion: Intake air temperature 493 K, fuel temperature 293 K

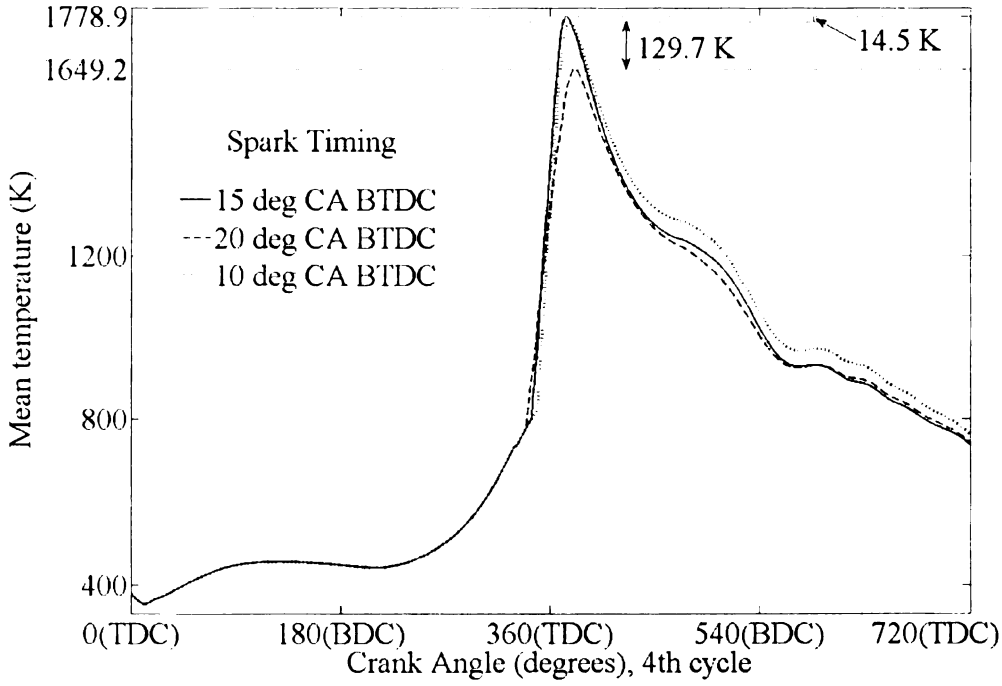

Figure 4.41 Effect of spark timing on combustion: Intake air temperature 593 K, fuel temperature 293 K

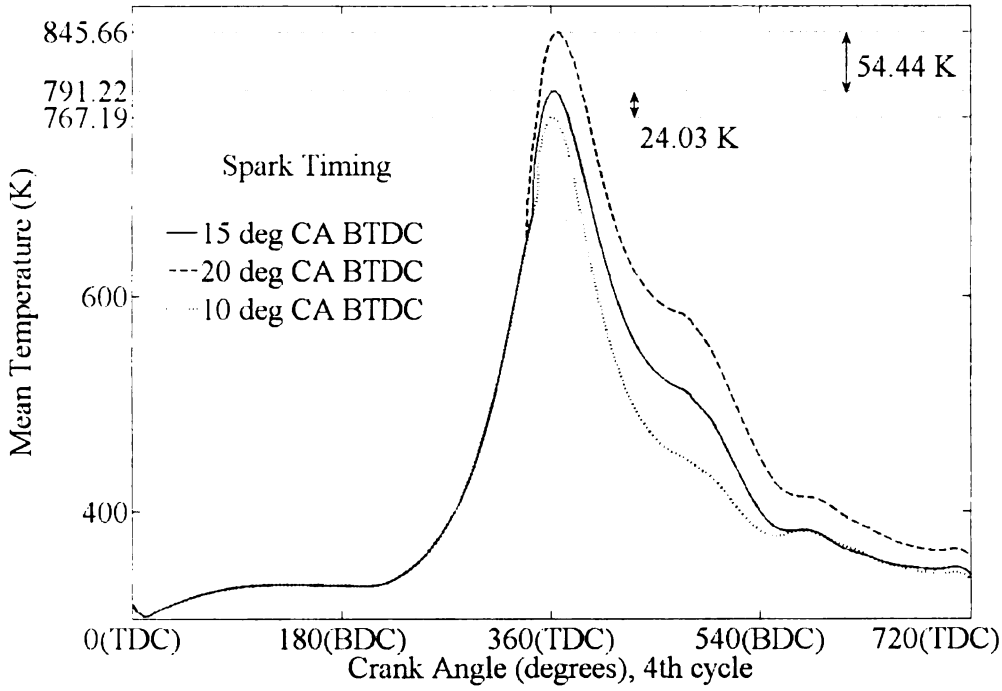

Figure 4.42 Effect of spark timing on combustion: Turbocharging pressure 1.25 atm, fuel temperature 293 K

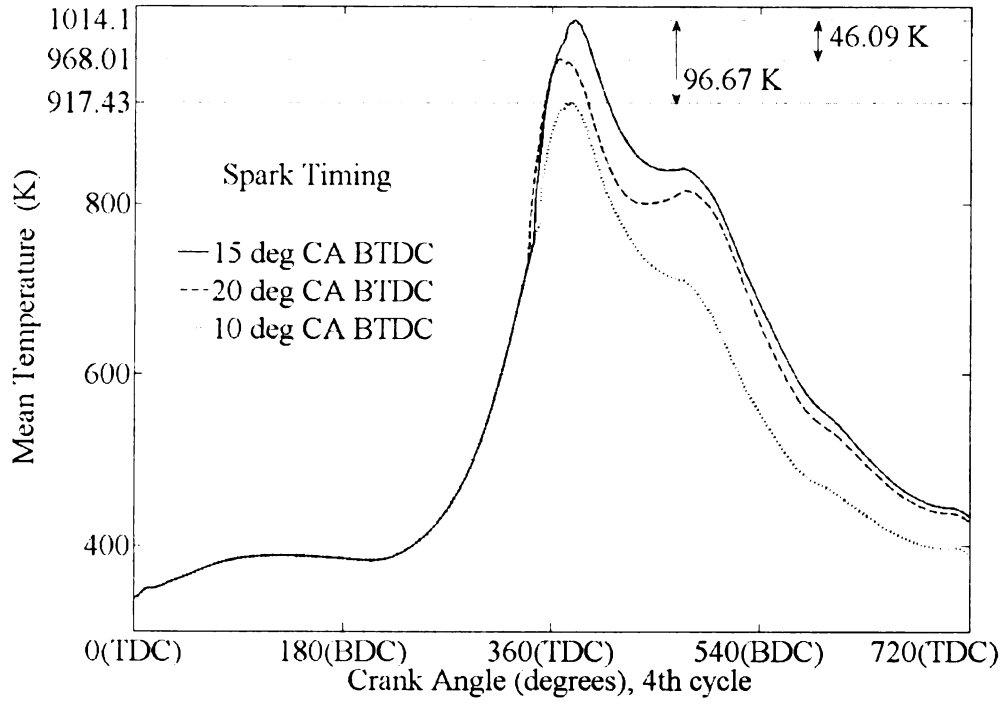

Figure 4.43 Effect of spark timing on combustion: Turbocharging pressure 1.50 atm, fuel temperature 293 K

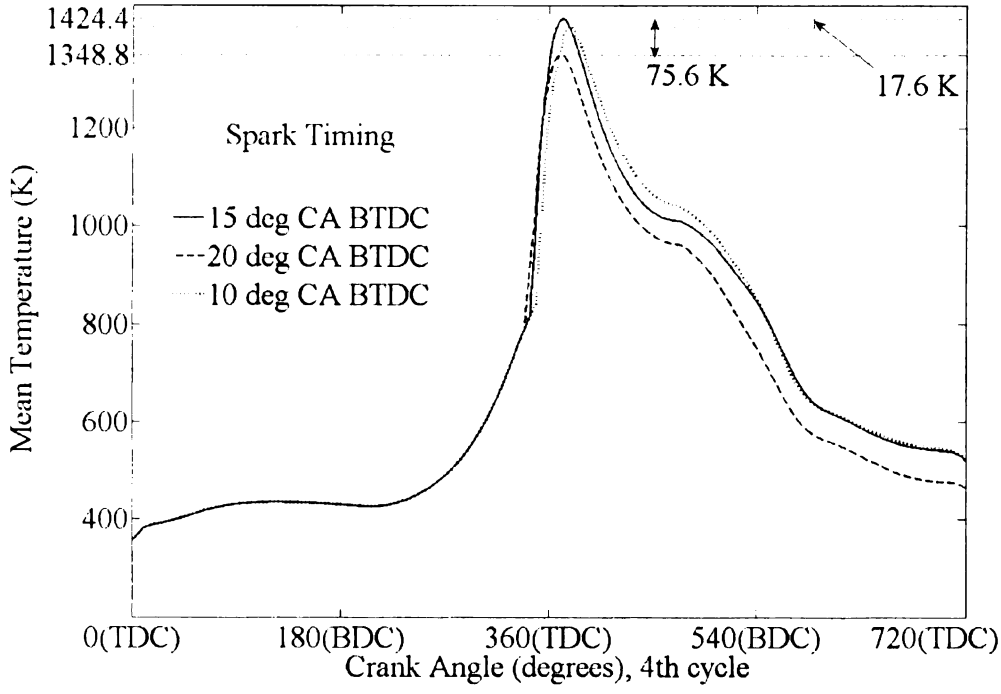

Figure 4.44 Effect of spark timing on combustion: Turbocharging pressure 1.75 atm, fuel temperature 293 K

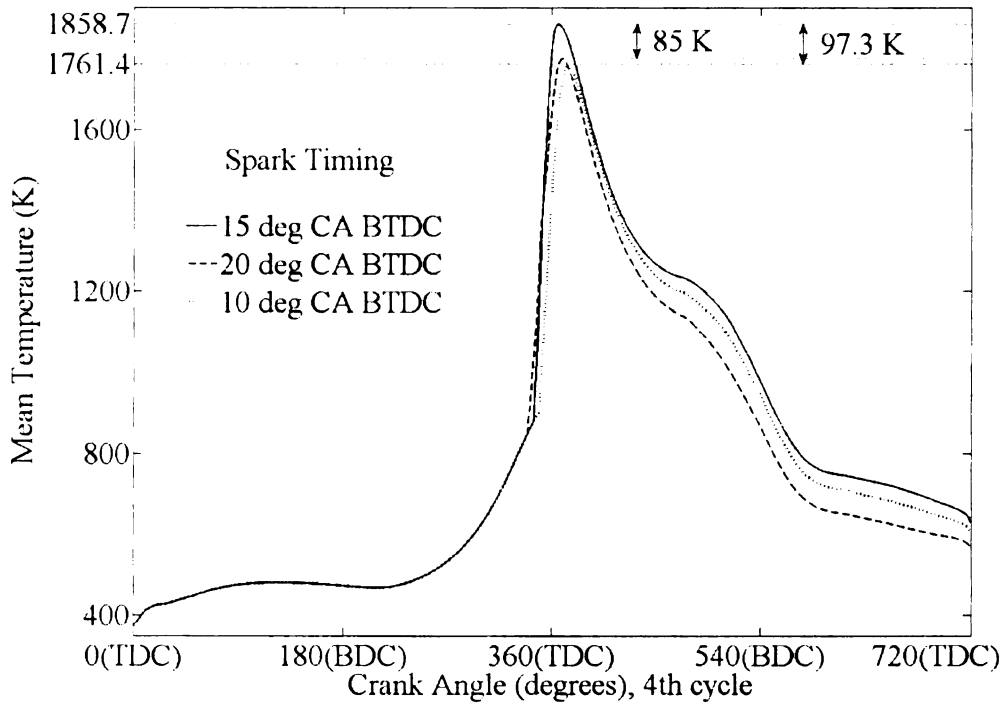

Figure 4.45 Effect of spark timing on combustion: Turbocharging pressure 2.00 atm, fuel temperature 293 K

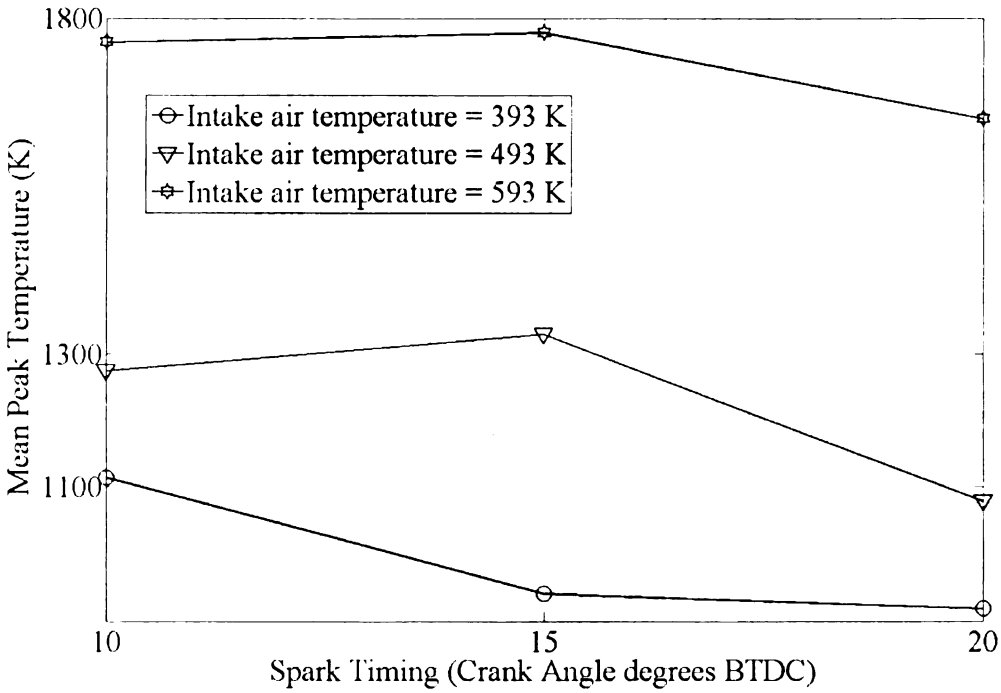

Figure 4.46 Variation of mean peak temperature with spark timing for different intake air temperatures

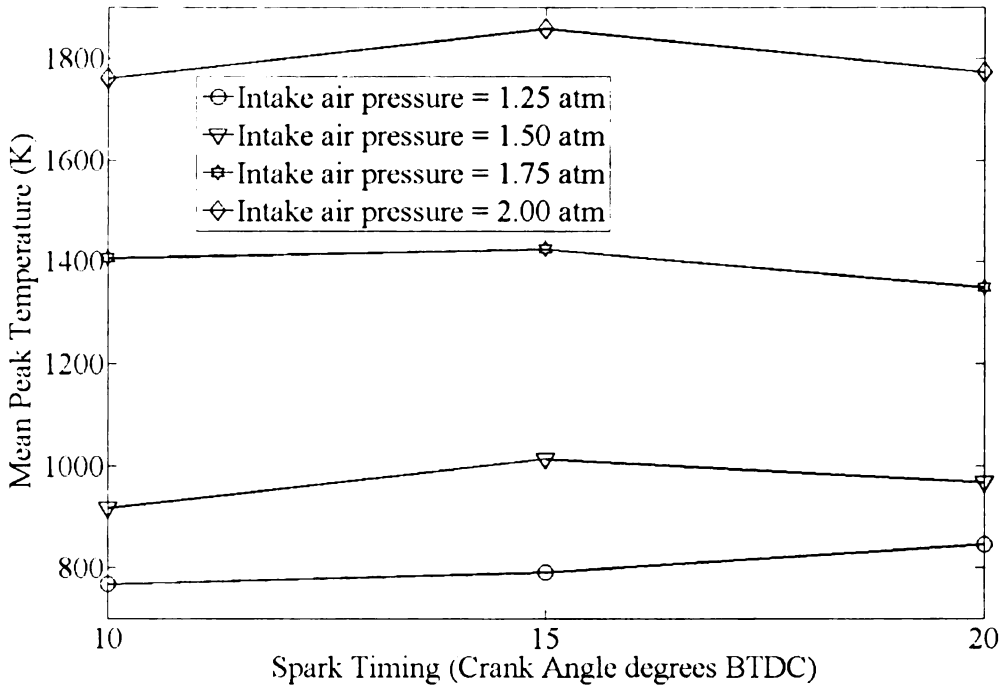

Figure 4.47 Variation of mean peak temperature with spark timing for different intake air pressures

Figures 4.46 and 4.47 show the variation of the mean peak temperature with spark timing for different intake air temperatures and pressures. We can conclude that for these conditions, spark at CA 15° BTDC gives the best combustion and we can use this result for the combustion simulations in the next section.

4.7 Effect of strategies on combustion

After having studied the effect of various parameters on the vaporization and mixing of the fuel-vapor mixture and determining the optimum spark timing, the next logical step would be to consider how the combustion of the mixture would be affected by the variation of these parameters. In all these cases, the spark has been given at two locations, at the center and at the concentrated vaporized fuel core near the wall.

4.7.1 Combustion: Heated Intake Air

As we had seen in the previous sections, adding heated intake air had resulted in increasing the equivalence ratio. So we should also expect better combustion in these cases. Figures 4.49 - 4.51 give the temperature and pressure histories for combustion when heated air was fed through the intake to the case when the incoming air was at room temperature (Figure 4.48). While intake air at 393 K does not give us any significant improvement in combustion, air at 493 K does give a higher rise in temperature and when the temperature of the incoming air is 593 K, we have significant combustion. These observations were for the case when the incoming fuel temperature was 293 K.

(a)

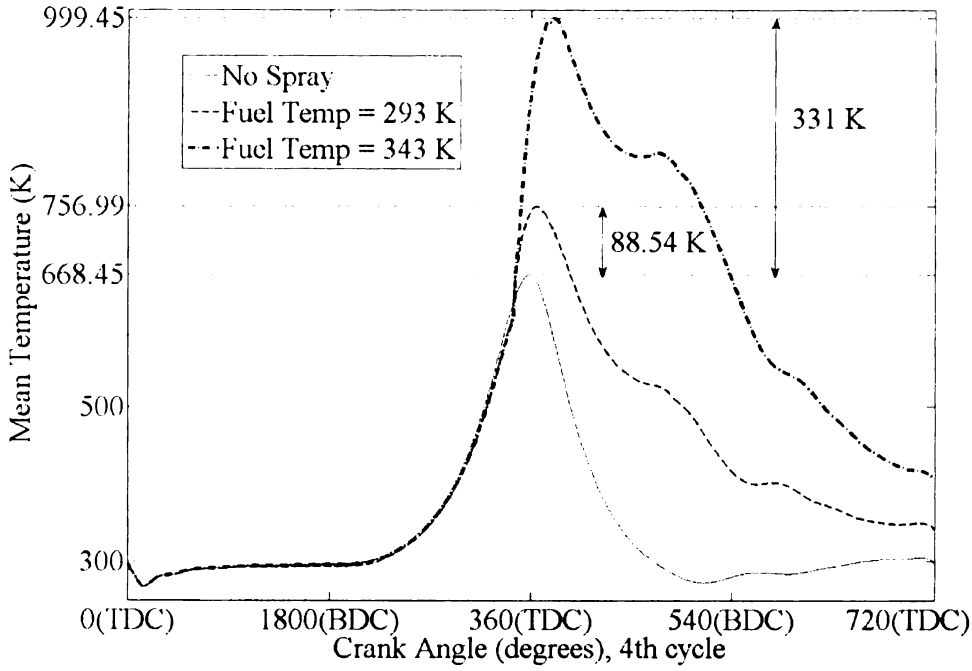

(b)

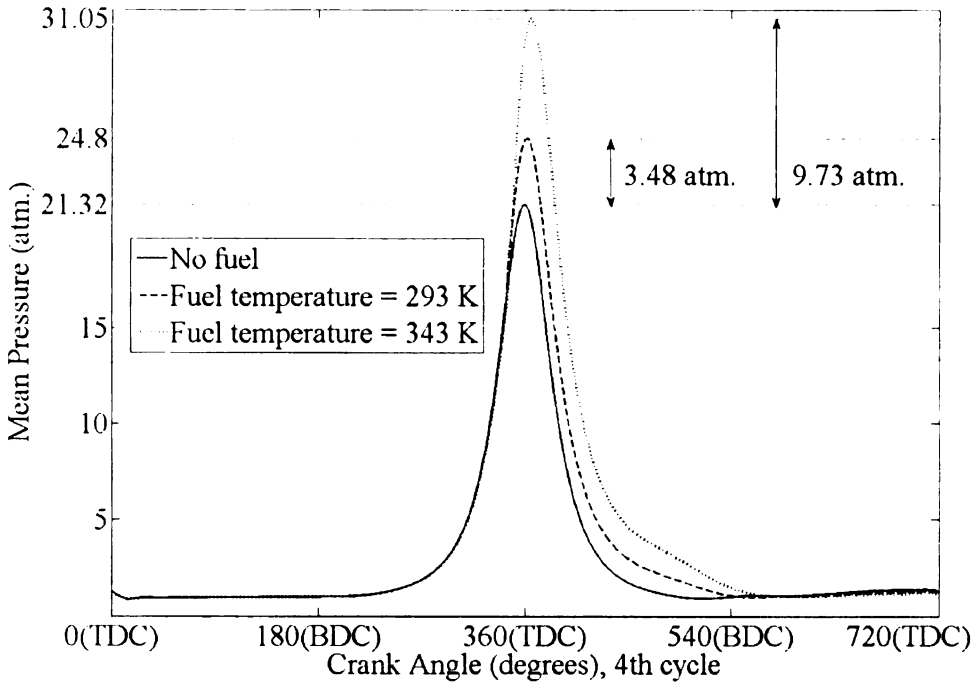

Figure 4.48 Combustion for intake air temperature 293 K (a) Temperature profile

(b) Pressure Profile

(a)

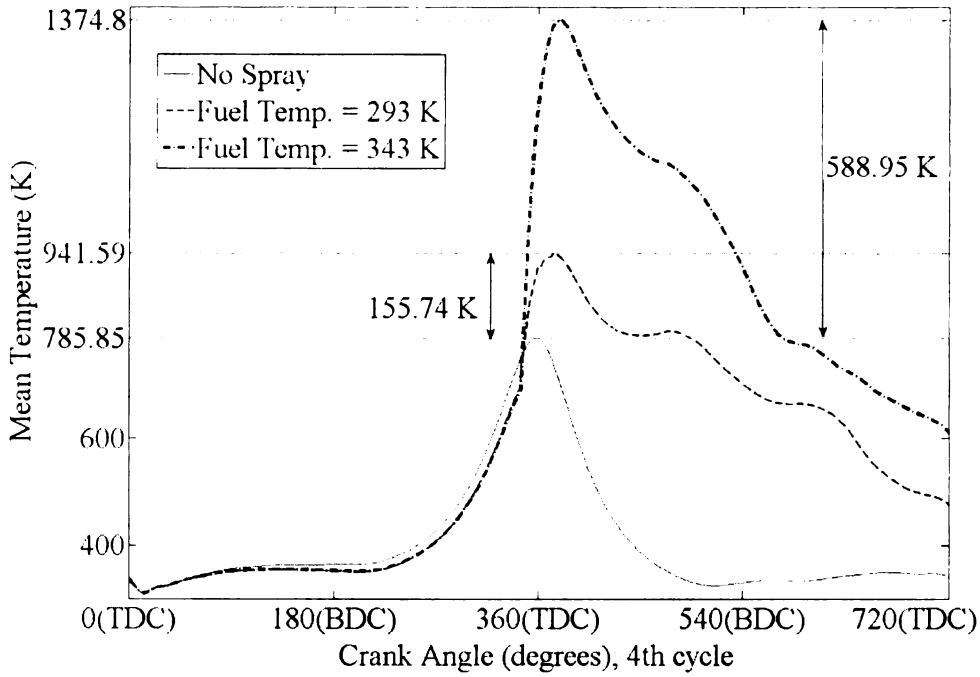

(b)

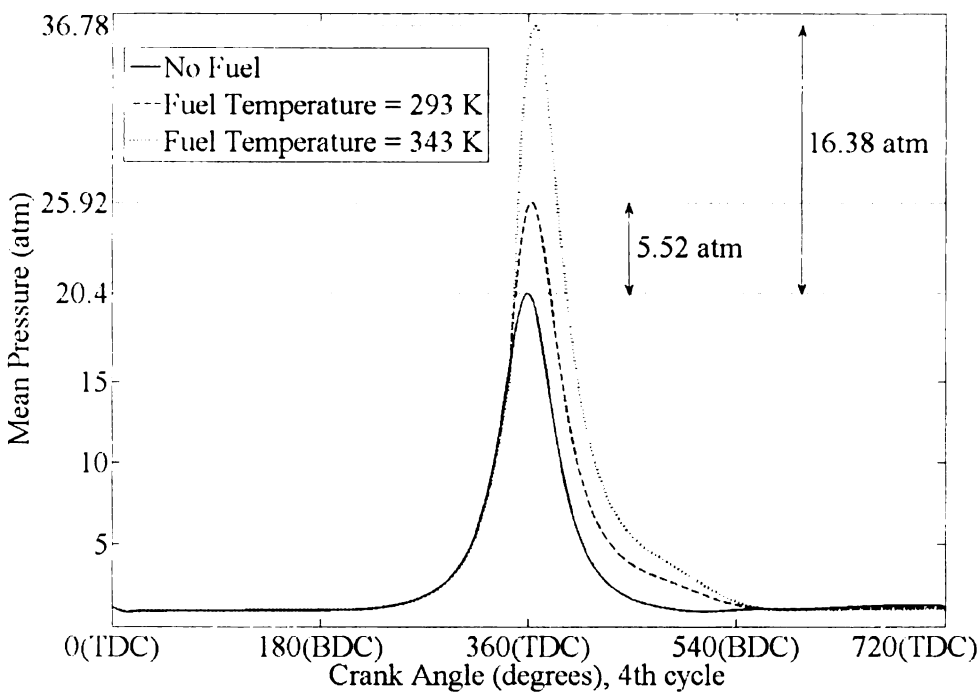

Figure 4.49 Combustion for intake air temperature 393 K (a) Temperature profile (b) Pressure Profile

(a)

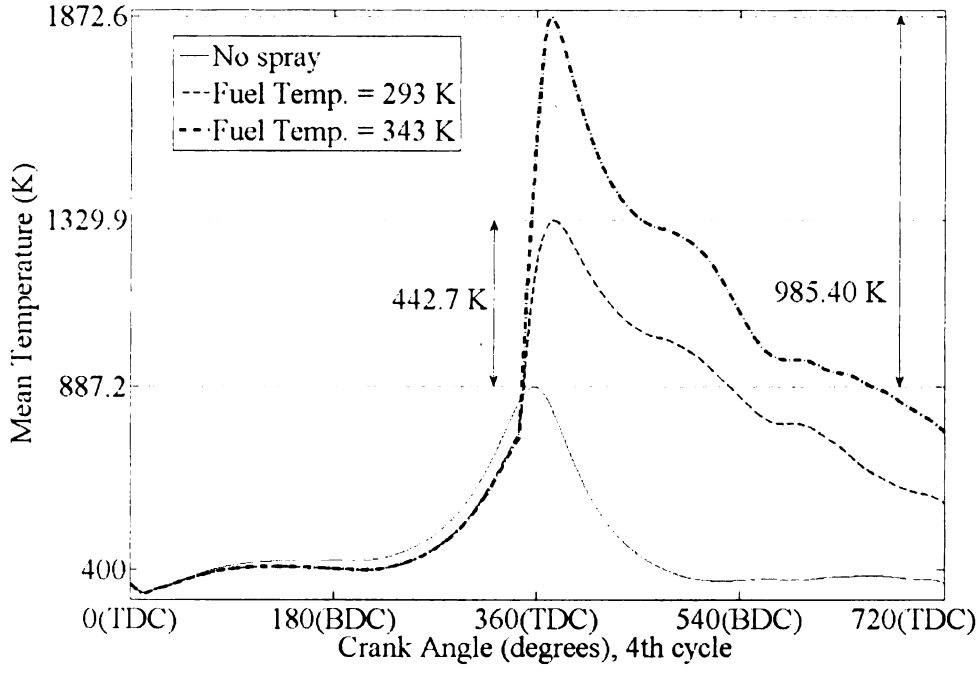

(b)

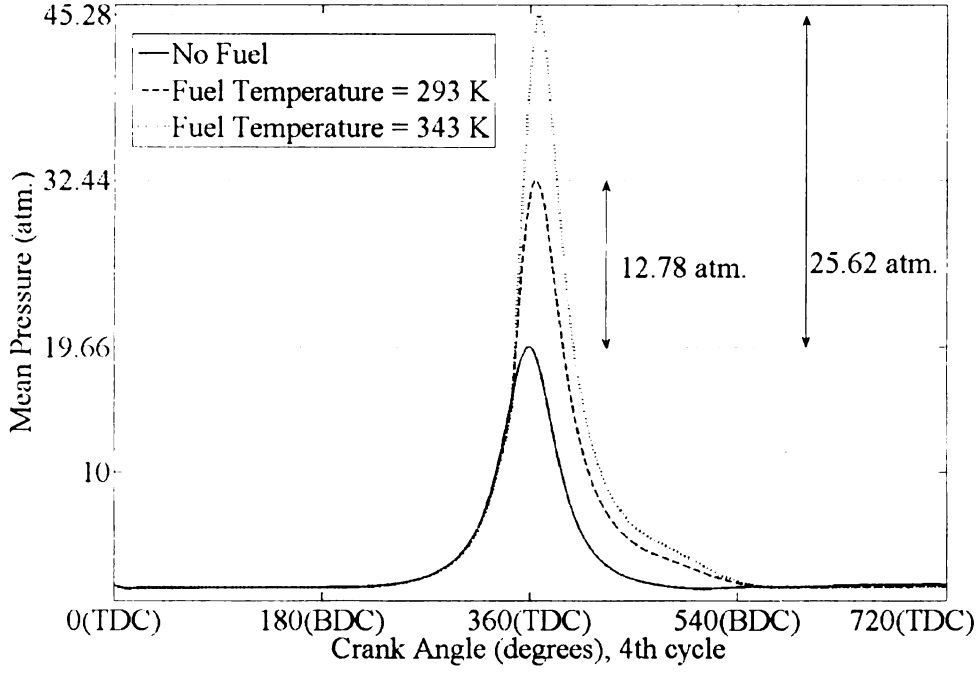

Figure 4.50 Combustion for intake air temperature 493 K (a) Temperature profile (b) Pressure Profile

(a)

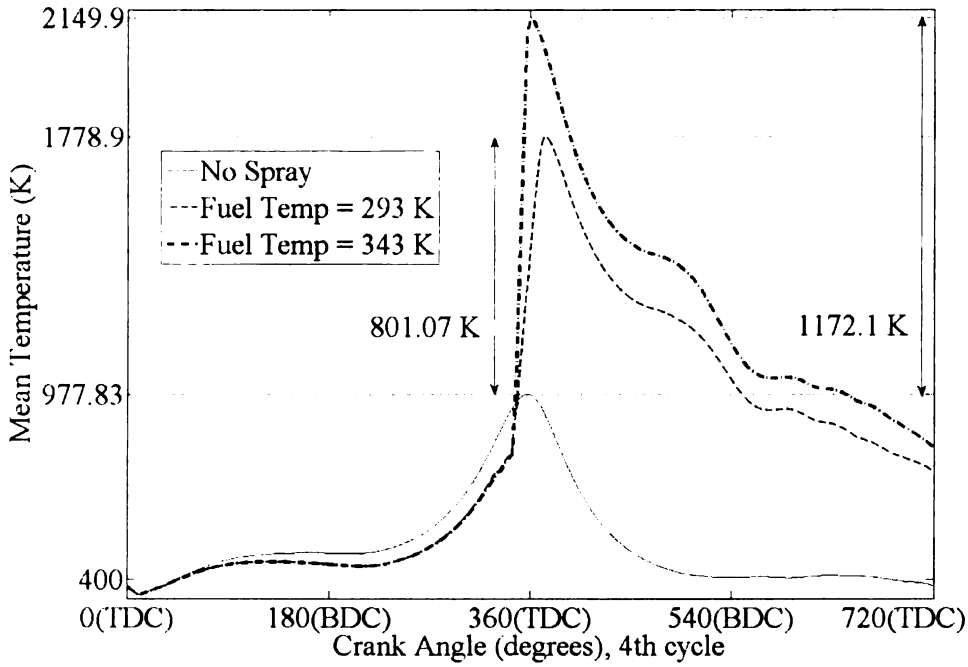

(b)

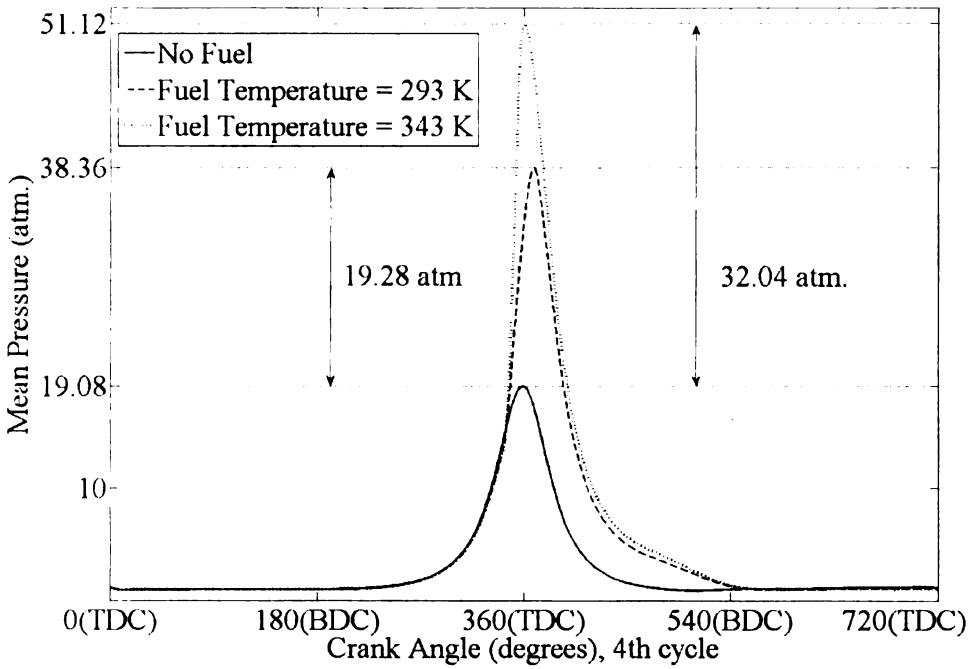

Figure 4.51 Combustion for intake air temperature 593 K (a) Temperature profile (b) Pressure Profile

Consider the case when the fuel temperature is increased to 343 K. Since the mean equivalence ratio in this case is much higher (Fig. 4.31), combustion should be much better. Now, we have significant combustion even in the case of intake air temperature 493 K and final gas temperatures reach values comparable to the gasoline combustion case when the intake air temperature is 593 K.

Figure 4.52 summarizes the results obtained above in terms of mean peak temperatures achieved after combustion. From this plot, an effort can be made to optimize the amount of heat to be supplied to the intake air and fuel to raise their temperatures. It can be observed that a higher peak temperature is obtained when the intake air is heated to 493 K and the fuel is heated to 343 K, as compared to the case when the air alone is heated to 593 K, which makes the first case an obvious choice. Since the density of air would decrease on heating it to a higher temperature, limiting the temperature to 493 K only would also result in a higher power output. Also, the peak temperature obtained is not very high and the probability of NOx production is also mitigated.

A much more intense analysis can be done to chart out the optimum intake air and fuel temperatures for different operating conditions.

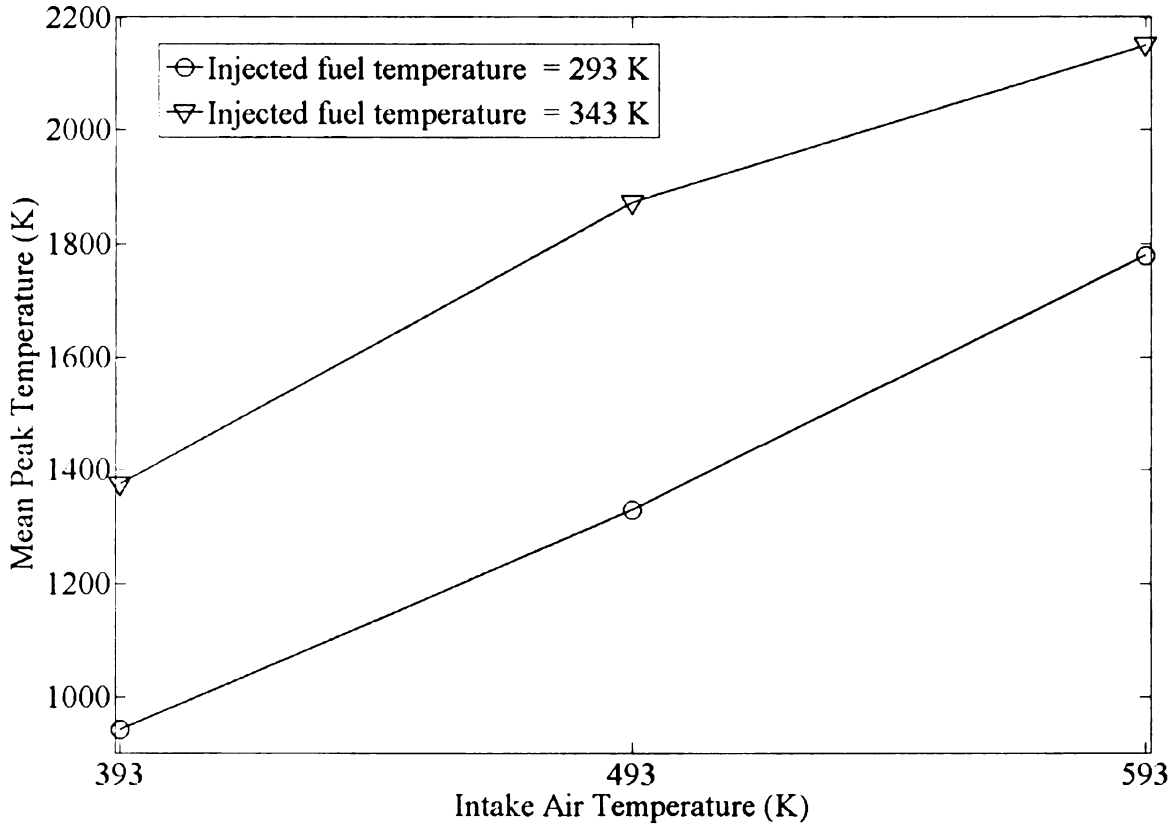

Figure 4.52 Variation of mean peak temperatures due to combustion for different intake air temperatures.

4.7.2 Combustion: Higher Intake Pressure/ Turbocharging

Here also, due to higher equivalence ratios for the fuel air mixture, we should expect to see better combustion as compared to our original case. An additional advantage, as compared to heating intake air, is that the pressure of the air is higher and the power output of the engine would also increase. Figures 4.53-4.56 give the temperature and pressure histories for combustion for cases with different intake air pressures.

While there is no significant combustion for intake air pressure 1.25 atm. for both fuel temperatures, for intake air pressure 1.50 atm. we have a significant rise in temperature and pressure when the fuel temperature is 343 K. For intake air pressure 1.75 atm., we have significant combustion for both fuel temperatures, and for intake pressure of 2.0 atm., we have temperatures attaining values comparable to gasoline combustion. Overall, using turbochargers should enable proper combustion of ethanol.

(a)

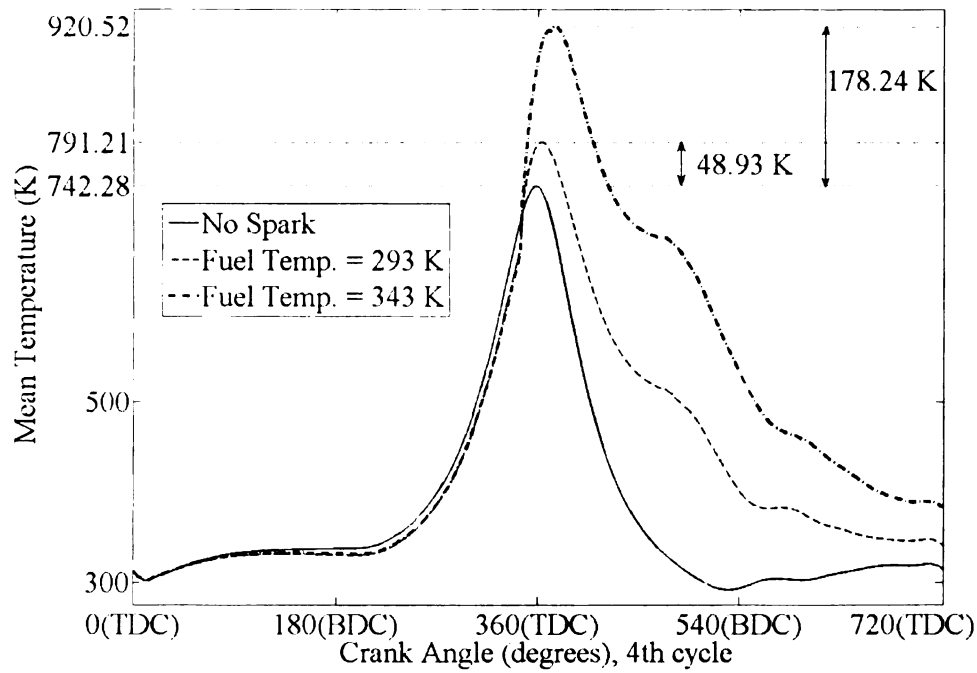

(b)

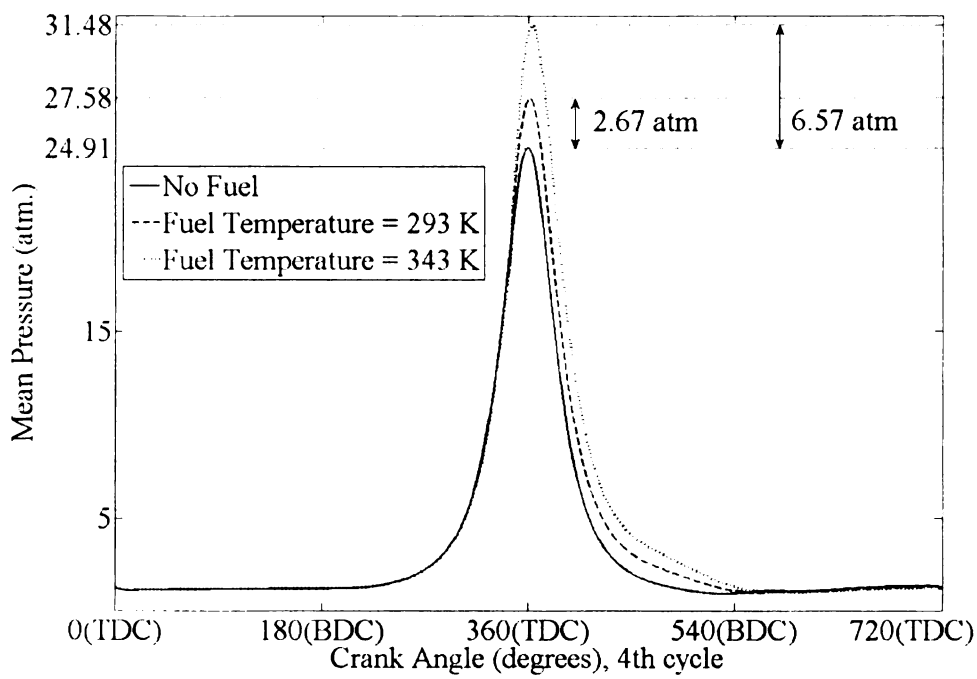

Figure 4.53 Combustion for intake air pressure 1.25 atm (a) Temperature profile

(b) Pressure Profile

(a)

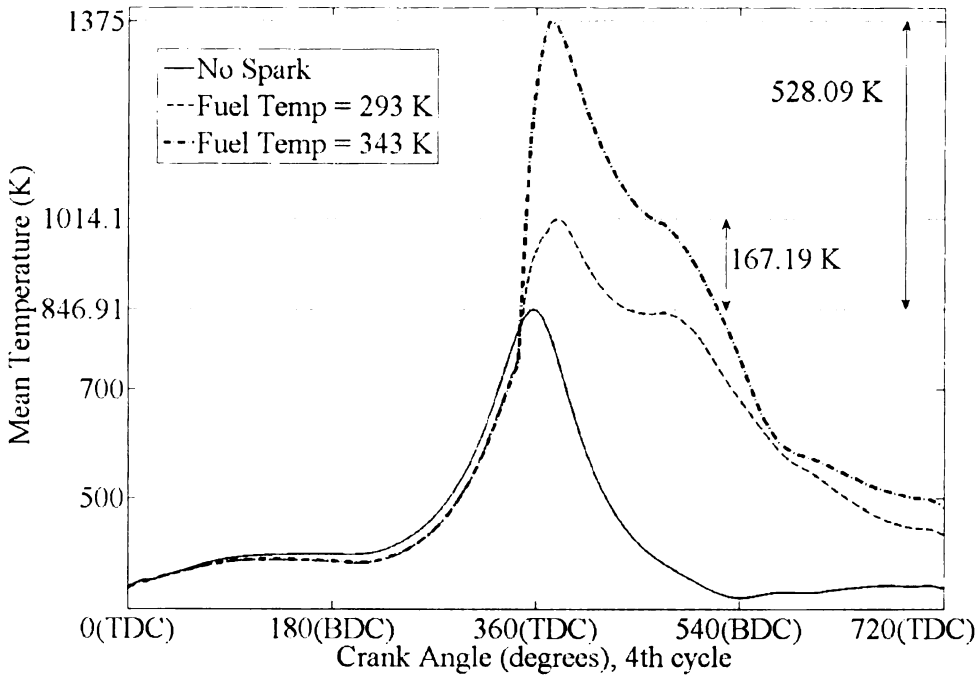

(b)

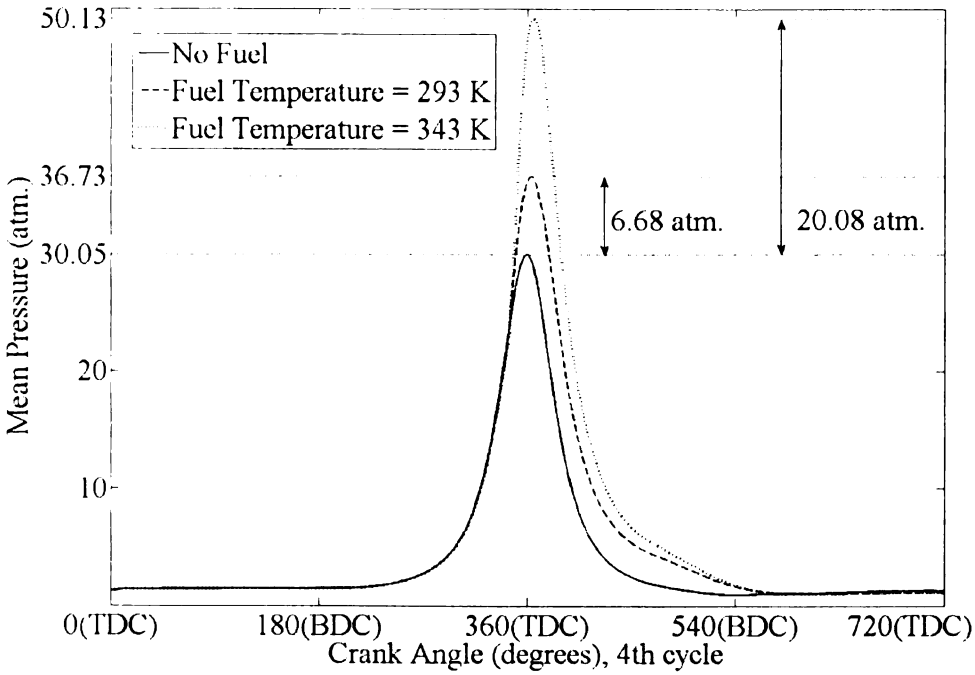

Figure 4.54 Combustion for intake air pressure 1.50 atm (a) Temperature profile (b) Pressure Profile

(a)

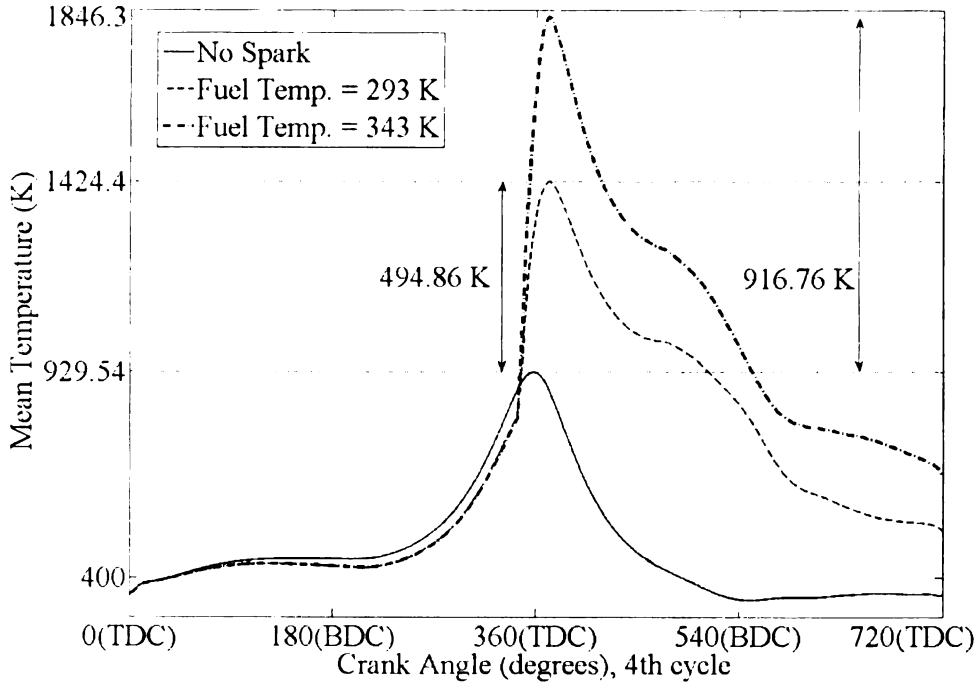

(b)

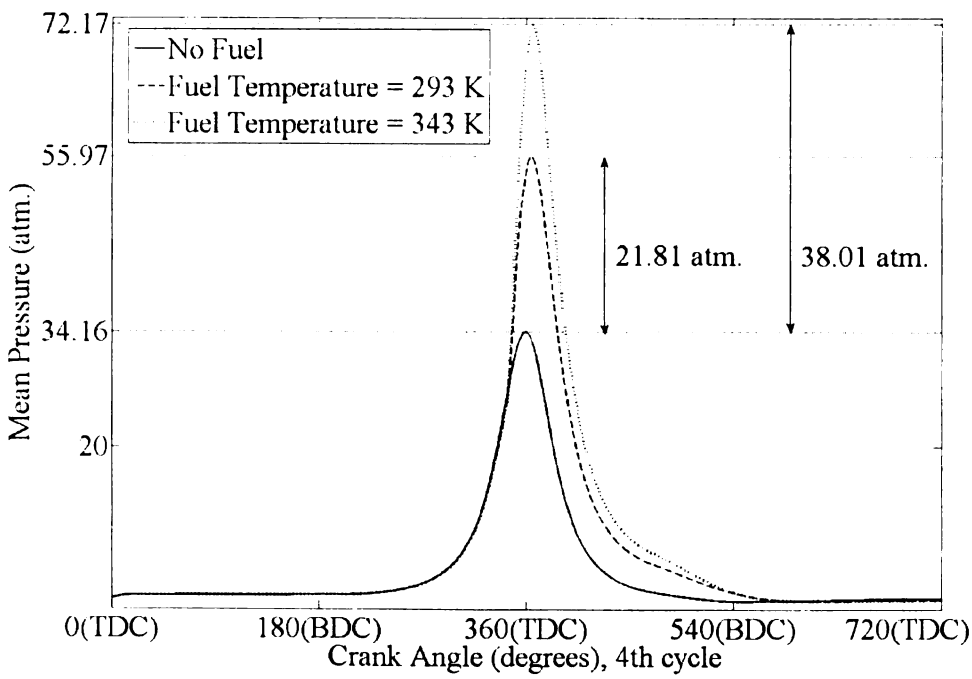

Figure 4.55 Combustion for intake air pressure 1.75 atm (a) Temperature profile

(b) Pressure Profile

(a)

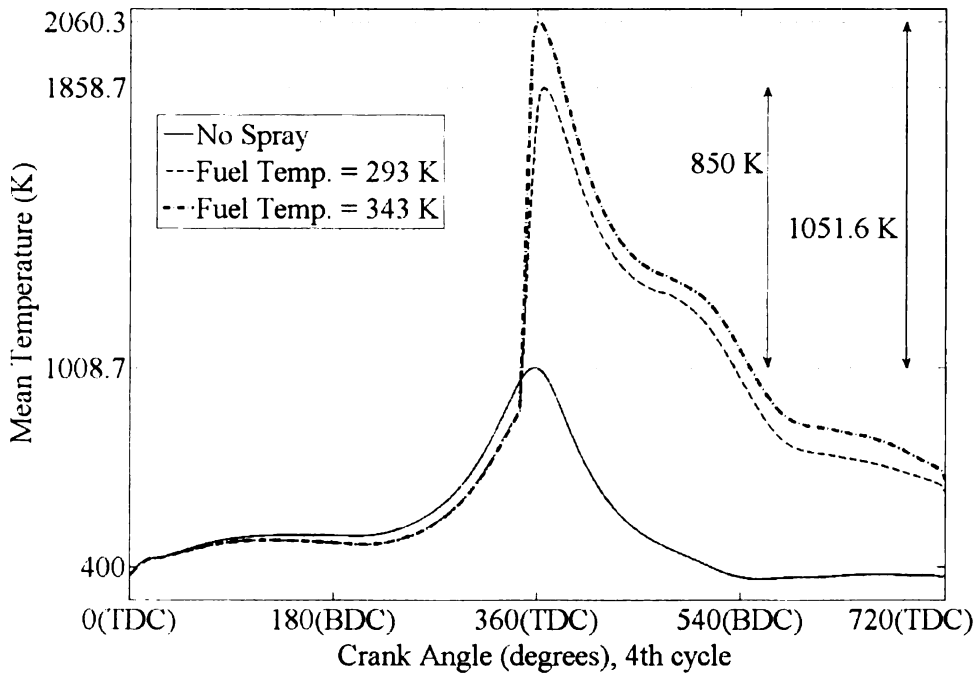

(b)

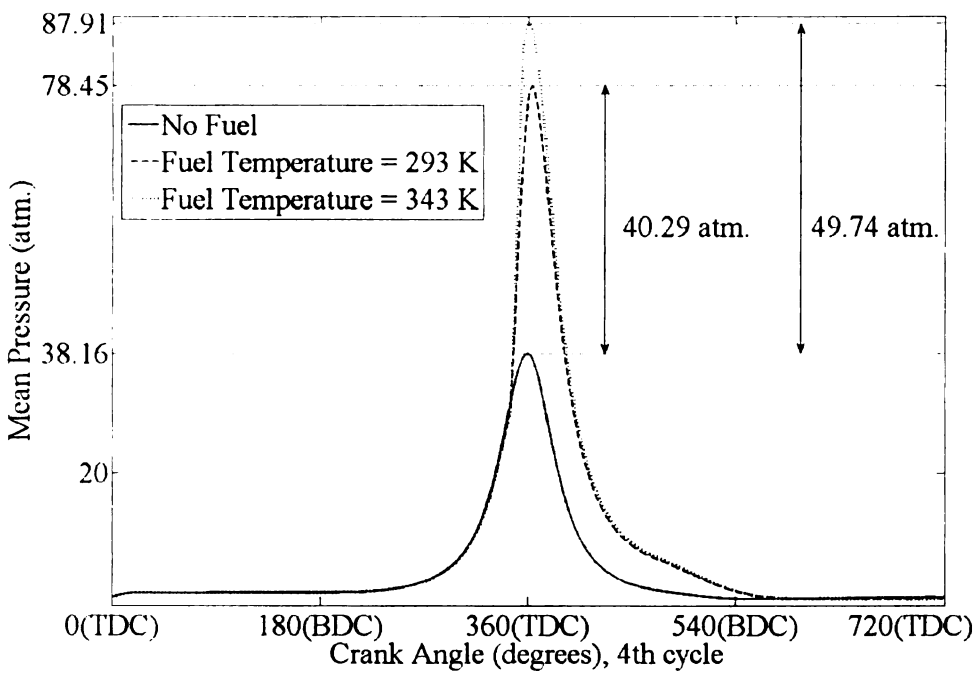

Figure 4.56 Combustion for intake air pressure 2.00 atm (a) Temperature profile (b) Pressure Profile

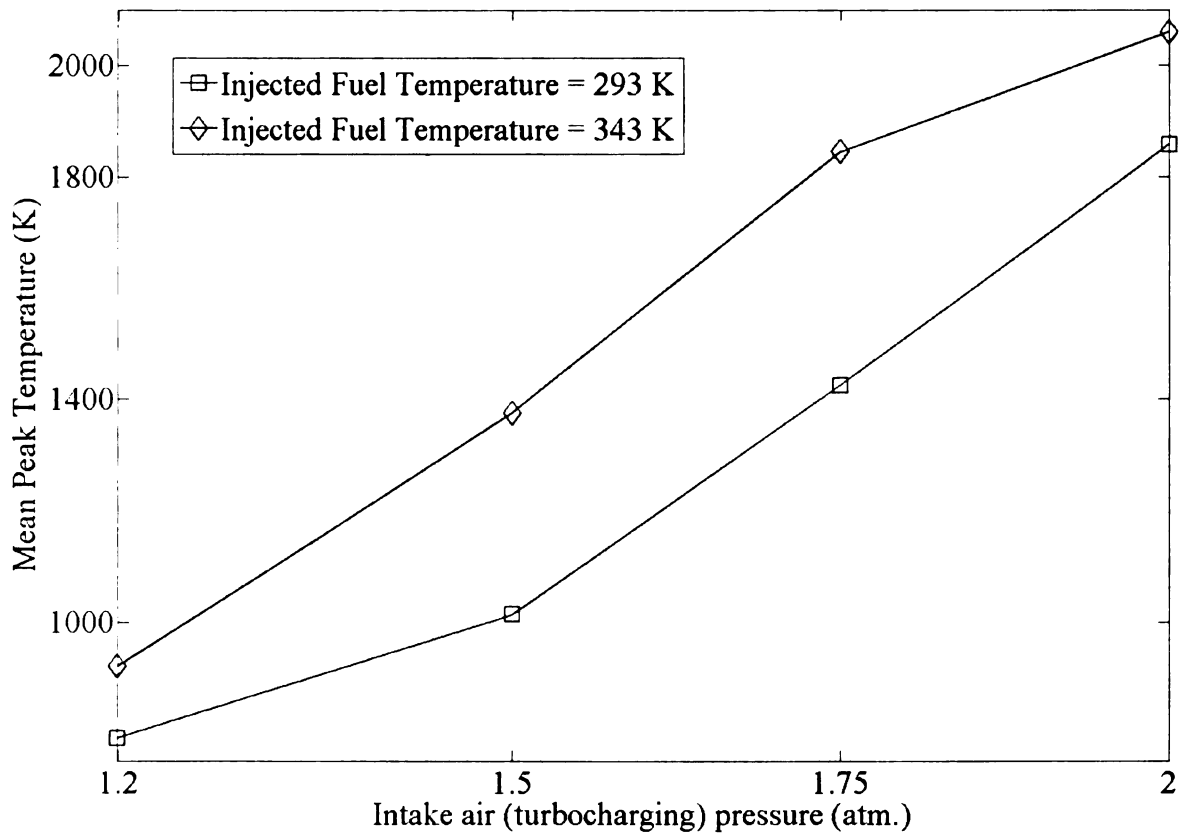

Figure 4.57 Variation of mean peak temperatures due to combustion for different intake air pressures

Figure 4.57 gives a summary of the results above with mean peak temperature as the dependent variable, and intake air temperature as well as injected fuel temperature being the independent variables. An interesting observation that can be made is that intake air pressure of 1.75 atm. with fuel temperature 343 K gives a mean peak temperature comparable to combustion for intake air pressure 2.0 atm. Thus, instead of increasing the air pressure to 2.00 atm., a better option might be to compress air only to 1.75 atm, and utilize the heat lost by cooling the air to heat up the fuel.

(a)

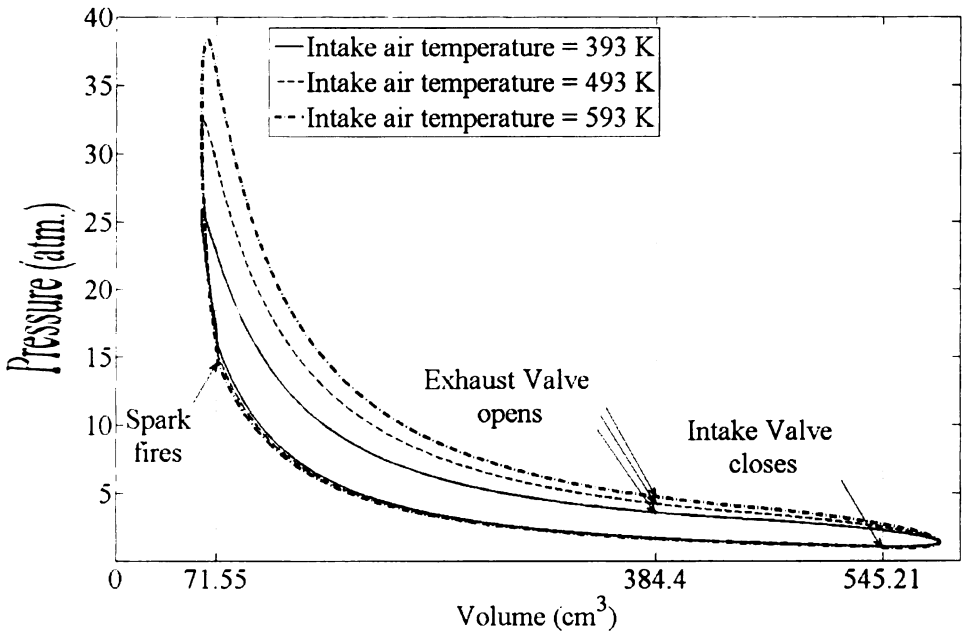

(b)

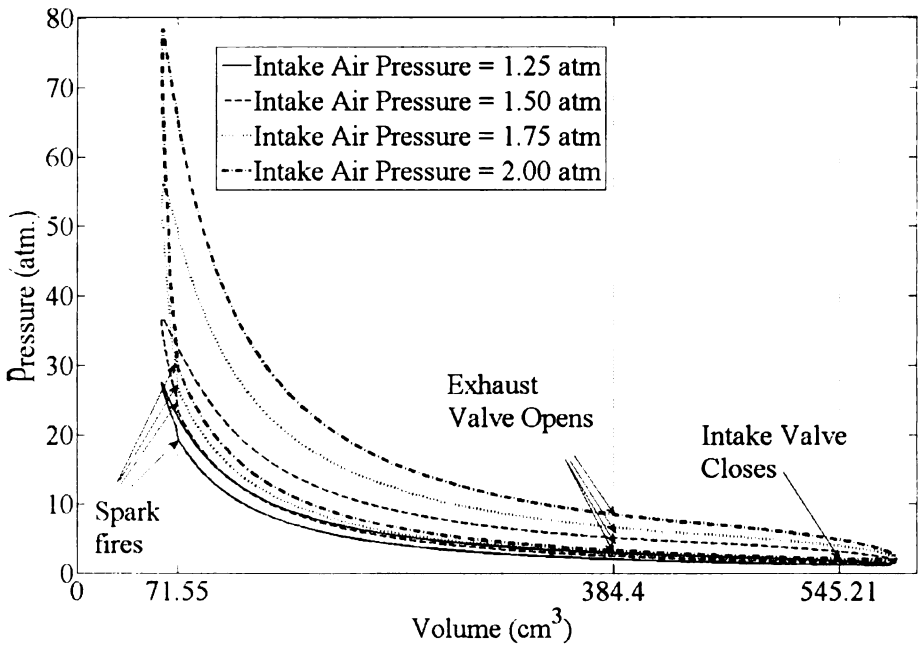

Figure 4.58 P-V diagrams for combustion (a) Different intake air temperatures (b) Different intake air pressures

Figure 4.58 shows the pressure variation with respect to the volume of the cylinder. It can be seen that when the intake air temperature is increased, the net work obtained from the engine also increases despite the decrease in density of the air. The work obtained from the engine also increases with the increase in the pressure of the incoming air.

CHAPTER 5

SUMMARY AND CONCLUSIONS

5.1 Summary

In this work, an attempt has been made to do numerical simulations to compare the performance of a direct injection spark ignition engine, operating with different fuels, namely gasoline and ethanol. A widely used, open source, computational fluid dynamics code KIVA 3V has been used for this purpose. An ignition delay model has been incorporated to mitigate some of the deficiencies of the global one step mechanism used to simulate combustion and simultaneously solve the unphysical problem of autoignition in a spark ignited engine with a moderate compression ratio of 9.8. The problem of cold start faced by ethanol operated engines has been observed in the simulations and various strategies to enhance ethanol vaporization and combustion have been tested. Simulation results indicate that some of the strategies used for emission control and downsizing of gasoline engines can be employed for enhancing combustion in ethanol operated engines.

The following list summarizes some of the features of this research:

- Detailed study of the main features of KIVA 3V, including the study of the governing equations, spray models and numerical schemes.

- Comparison of the properties of ethanol and gasoline

- Review of some of the methods being investigated to enhance cold start of ethanol operated engines.

- Study of the effect of different initial conditions and cycle to cycle variability of mean thermodynamic quantities.

- Selection of important spray parameters.

- Review of some of the mechanisms of ethanol oxidation and empirical ignition delay correlations.

- Formulation of an ignition delay look up table, with the help of a commercial chemical kinetics software CHEMKIN^{TM}, with temperature and equivalence ratios as the variable parameters.

- Use of an ignition delay model to correct the small ignition delays predicted by the one step global mechanism used to simulate combustion in KIVA.

- Comparison of vaporization and combustion of gasoline and ethanol for the same operating conditions.

- Study of the effect of various methods to improve vaporization of ethanol.

- Selection of optimum spark timing for the given operating conditions.

- Study of the effect of various methods to improve vaporization on combustion.

5.2 Conclusions

Due to the unavailability of experimental results for ethanol and detailed initial and boundary conditions required for a proper numerical simulation, it is not possible to make quantitative comparisons and conclusions. Also, the use of a relatively coarse grid, diffusive $k-\varepsilon$ turbulence model and a global combustion model, does not give sufficient numerical accuracy to make detailed comparisons, which would be possible only by the use of Large Eddy Simulations (LES) or Direct Numerical Simulations (DNS). But a qualitative analysis of the results is still possible and the conclusions of such an analysis are as follows:

- Cold start problem can be observed in case of ethanol operated internal combustion engines. The problem is due to low vaporization caused by the high latent heat of vaporization and low vapor pressure of ethanol.

- Increasing temperature of intake air gives better ethanol vaporization and consequently better combustion.

- Use of turbochargers also gives better fuel vaporization and combustion.

- An optimum way to enhance cold start operation of ethanol operated engines would be to simultaneously increase the intake air temperature or pressure and the temperature of the injected fuel.

5.3 Recommendations for future work

In order to gain a better understanding of ethanol operated internal combustion engines, some of the possibilities for future work are as follows:

- Use of a finer grid for better quantitative results.

- Use E85, a mixture of 85% ethanol and 15% gasoline by volume, as fuel.

- Consider the effect of exhaust gases on ignition delay, to properly simulate Exhaust Gas Recirculation (EGR).

- Use of improved primary and secondary droplet breakup models,

turbulence models like Reynolds stress models (RSM) and detailed multistep, multispecies chemical mechanisms.

- Use of the latest version of KIVA called KIVA 4. Some of the features of KIVA 4 which can be useful are:
    - Uses unstructured grids, allowing easier generation of complex engine geometries.
    - Allows parallelization of the code, thus encouraging the use of finer grids.
    - A multicomponent fuel algorithm is available, allowing the simulation of multicomponent fuels like gasoline and E85.

APPENDIX

BOUNDARY CONDITIONS

This appendix describes briefly the methodology used in KIVA 3V to assign boundary and initial conditions to the various relevant quantities.

Velocity Boundary Conditions: For rigid walls, the boundary conditions can be specified as:

1. **No Slip**: The gas velocity equals the wall velocity in this case.
2. **Free Slip**: In this case, the normal gas velocity is equal to the normal wall velocity and the tangential components of the wall stress are set to zero.
3. **Turbulent law-of-the-wall**: Again the normal gas velocity is set equal to the normal wall velocity while matching the velocity to a logarithmic profile dependent on the k- ε model constants specifies the tangential components of wall stress.

In this project, the velocities have been set to **turbulent law-of-the-wall** condition.

Temperature Boundary conditions on the wall: There are two options:

1. **Adiabatic Wall**: In this case, the wall heat flux is zero.
2. **Constant Temperature Wall**: If the velocity boundary condition is no slip or free slip, the wall temperature is specified. However, if the turbulent law-of-the-wall condition is used, the wall heat flux is specified using a

modified Reynolds analogy formula.

Turbulence Parameters: The Boundary conditions for k and ε are assigned in KIVA 3V by the following two equations:

$\nabla k.n = 0$ and $\varepsilon = c_{\mu\varepsilon} \frac{k^{3/2}}{y}$, where k and ε are evaluated a distance y from the wall and

$$c_{\mu\varepsilon} = \left[\frac{c_\mu}{\mathrm{Pr}_\varepsilon \left(c_{\varepsilon_2} - c_{\varepsilon_1} \right)} \right]^{1/2}$$

INITIAL CONDITIONS

Some of the important initial conditions specified are as follows:

Temperature: Initial temperature inside the cylinder and the intake and exhaust varies for different cases considered. The temperatures of the cylinder wall, cylinder head, piston and the valve surface are set to 293 K.

Pressure: Initial pressure of the air is set to be 1 atm.

Velocity: Inlet velocity at the intake runner is specified to be zero and the flow is pressure driven.

Turbulence parameters: Inside the cylinder, k=0.10 cm^2/s^2 and turbulence length scale = 0 cm. In this case, initial ε will be proportional to the distance to the nearest solid wall. At the intake and exhaust boundaries, ambient k=423 cm^2/s^2 and ambient turbulence length scale=4.8 cm

Swirl Profile: Two quantities define the initial swirl conditions inside the cylinder:

1. **α=3.11**. This defines the initial azimuthal velocity profile and the specified value is commonly used for engine flows.
2. **Initial swirl ratio of air rpm to crankshaft rpm**. This is set to 0 in this project.

BIBLIOGRAPHY

1. Avinash Kumar Agarwal. Biofuels (alcohols and biodiesel) applications as fuels for internal combustion engines. Progress in Energy and Combustion Science 33: 233-271, 2007

2. Dennis J. Miller, Ramani Narayan, Kris A. Berglund, Carl T. Lira, Harold J. Schock, Farhad Jaberi, Tonghun Lee, James Anderson, Timothy Wallington, Eric Kurtz, Will Ruona, and Heinz Hass. Novel Biofuel Formulations for Enhanced Vehicle Performance. 2007

3. A.A. Amsden. KIVA-3V: A Block-Structured Computer Program for 3-D Fluid Flows with Valves, Chemical Reactions, and Fuel Sprays. Los Alamos National Laboratory, 1998

4. Wen Dai, Sreeni Cheemalamarri, Eric W. Curtis, Riadh Boussarsar, and Richard K. Morton. Engine Cycle Simulation of Ethanol and Gasoline Blends. SAE Technical Paper 2003-01-3093 (2003).

5. Matthew Brusstar and Marco Bakenhus. Economical, High – Efficiency Engine Technologies for Alcohol Fuels

6. Koichi Nakata, Shintaro Utsumi, Atsuharu Ota, Katsunori Kawatake, Takashi Kawai and Takashi Tsunooka. The Effect of Ethanol Fuel on a Spark Ignition Engine. SAE Technical Paper 2006-01-3380 (2006).

7. Pamela R.D. Williams, Colleen A. Cushing, and Patrick J. Sheehan. Data Available for Evaluating the Risks and Benefits of MTBE and Ethanol as Alternative Fuel Oxygenates. Risk Analysis, Vol. 23, No. 5, 2003.

8. Gregory W. Davis. Development of Technologies to Improve Cold Start Performance of Ethanol Vehicles. Final Report Grant No. PLA-00-48, Department of Consumer & Industry Services, State of Michigan.

9. Tomoko Kito-Borsa, Debra A. Pacas, Sami Selim, and Scott W. Cowley. Properties of an Ethanol-Diethyl Ether-Water Fuel Mixture for Cold-Start Assistance of an Ethanol-Fueled Vehicle. Ind. Eng. Chem. Res., 37, 3366-3374, 1998.

10. Dan Cordon, Eric Clarke, Steven Beyerlein, and Judi Steciak. Catalytic Igniter to Support combustion of Ethanol-Water/Air Mixtures in Internal Combustion Engines. SAE Technical Paper 2002-01-2863. (2002).

11. Luis Carlos Monteiro Sales and Jose Ricardo Sodre. Optimized Cold-Start Auxiliary System for Emissions Reduction in Ethanol-Fueled Engines. SAE Technical Paper 2002-01-2690. (2002)

12. A.A Amsden, J.D. Ramshaw, P.J. O'Rourke, and J.K. Dukowicz. KIVA: A Computer Program for Two- and Three- Dimensional Fluid Flows with Chemical Reactions and Fuel Sprays. Los Alamos National Laboratory report LA-10245-MS (February 1985).

13. A.A Amsden, J.D. Ramshaw, L.D. Cloutman, and P.J. O'Rourke. Improvements and Extensions to the KIVA Computer Program. Los Alamos National Laboratory report LA-10534-MS (October 1985).

14. A.A Amsden, , T.D. Butler, P.J. O'Rourke, and J.D. Ramshaw. KIVA: A Comprehensive Model for 2D and 3D Engine Simulations. SAE Technical Paper 850554 (1985).

15. A.A Amsden, P.J. O'Rourke, and T.D. Butler. KIVA-II: A Computer Program for Chemically Reactive Flows with Sprays. Los Alamos National Laboratory report LA-11560-MS (May 1989).

16. A.A Amsden. KIVA-3: A KIVA Program with Block-Structured Mesh for Complex Geometries. Los Alamos National Laboratory report LA-12503-MS (March 1993).

17. A.A Amsden. KIVA-3V: A Block-Structured KIVA Program for Engines with Vertical or Canted Valves. Los Alamos National Laboratory report LA-13313-MS (July 1997).

18. A.A Amsden. KIVA-3V, Release 2, Improvements to KIVA-3V. Los Alamos National Laboratory report LA-13608-MS (1998).

19. Rolf D. Reitz. Computer Modeling of Sprays. Spray Technology Short Course. Pittsburgh, PA. May 7, 1996.

20. P.J. O'Rourke and A.A Amsden. The TAB Method for Numerical Calculation of Spray Droplet Breakup. SAE Technical Paper 872089 (1987).

21. F. Zhao, M.-C Lai, and D.L. Harrington. Automotive spark-ignited direct-injection gasoline engines. Progress in Energy and Combustion Science, 25:437-562, 1999.

22. P.J. O'Rourke and A.A Amsden. A Particle Numerical Model for Wall Film Dynamics in Port-Injected Engines. SAE Technical Paper 961961 (1996).

23. P.J. O'Rourke and A.A Amsden. A Spray/Wall Interaction Submodel for the KIVA-3 Wall Film Model. SAE Technical Paper 2000-01-0271 (2000).

24. C. Baumgarten. Mixture Formation in Internal Combustion Engines. Springer – Verlag Berlin Heidelberg (2006).

25. Henry J. Curran, Mary P. Dunphie, John M. Simmie, Charles K. Westbrook, and William J. Pitz: Shock Tube Ignition of Ethanol, Isobutene and MTBE: Experiments and Modeling. Twenty-Fourth Symposium (International) on Combustion/ The Combustion Institute, pages 769 – 776, 1992.

26. Joseph W. Bollentin and Richard D. Wilk. Autoignition Characteristics of Ethanol. SAE Technical Paper. 961175 (1996).

27. Charles K. Westbrook and Frederick L. Dryer. Chemical Kinetic Modeling of Hydrocarbon Combustion. Progress in Energy and Combustion Science, 10:1-57, 1984.

28. Nick M. Marinov. A detailed chemical kinetic model for high temperature ethanol oxidation. International Journal of Chemical Kinetics, 31(3):183-220, 1999.

29. T.S. Norton and F.L. Dryer. An experimental and modeling study of ethanol oxidation kinetics in an atmospheric pressure flow reactor. International Journal of Chemical Kinetics, 24(4): 319-344, 1992.

30. Apoorva Agarwal and Dennis N. Assanis. Multi-Dimensional Modeling of Natural Gas Ignition Under Compression Ignition Conditions Using Detailed Chemistry, SAE Technical Paper 980136 (1998)

31. Valeri I. Golovitchev and N. Nordin. Detailed Chemistry Sub-Grid Scale Model of Turbulent Spray Combustion for the KIVA Code. In-Cylinder Flows and Combustion Processes, Vol. 33-3, pp.17--25, ASME Fall Technical Conference, Ann Arbor, Michigan,1999

32. Valeri I. Golovitchev, N. Nordin, and Jerzy Chomiak. 3-D Diesel Spray Simulations Using a New Detailed Chemistry Turbulent Combustion Model. SAE Technical Paper 2000-01-1891. (2000)

33. Feng Tao, Valeri I. Golovitchev, and Jerzy Chomiak. Self-Ignition and Early Combustion Process of N-Heptane Sprays Under Diluted Air Conditions :Numerical Studies Based on Detailed Chemistry. SAE Technical Paper 2000-01-2931 (2000)

34. Jonas Gustavsson, Valeri Golovitchev, and Arjan Helmantel. 3-D Modeling of Conventional and HCCI Combustion Diesel Engines. SAE Technical Paper 2004-01-2964 (2004)

35. Song-Charng Kong and Rolf D. Reitz. Application of detailed chemistry and CFD for predicting direct injection HCCI engine combustion and emissions. Proceedings of the Combustion Institute, 29(1): 663-669, 2002.

36. Y.Z. Zhang, E.H. Kung, and D.C. Haworth. A PDF method for multidimensional modeling of HCCI engine combustion: effects of turbulence/chemistry interactions on ignition timing and emissions. Proceedings of the Combustion Institute, 30(2): 2763-2771, 2005.

37. R. J. Kee, F. M. Rupley, J. A. Miller, M. E. Coltrin, J. F. Grcar, E. Meeks, H. K. Moffat, A. E. Lutz, G. Dixon-Lewis, M. D. Smooke, J. Warnatz, G. H. Evans, R. S. Larson, R. E. Mitchell, L. R. Petzold, W. C. Reynolds, M. Caracotsios, W. E. Stewart, P. Glarborg, C. Wang, C. L. McLellan, O. Adigun, W. G. Houf, C. P. Chou, S. F. Miller, P. Ho, P. D. Young, D. J. Young, D. W. Hodgson, M. V. Petrova, and K. V. Puduppakkam, CHEMKIN Release 4.1, Reaction Design, San Diego, CA (2006).

38. Chemkin™ Theory Manual. Release 4.1. Reaction Design. 2006

39. Chemkin™ Getting started. Release 4.1. Reaction Design. 2006

40. Maarcio Turra deAvila, Luben Cabezas Gaomez, Marcelo Valente Feitosa, and Michael George Maunsell. Heat Exchanger Study for Ethanol Vaporization to Fuel Otto Cycle Engines. SAE Technical Paper. 2001-01-3836. (2001).

41. L. Guzzella, U. Wenger and R. Martin. IC Engine Downsizing and Pressure-Wave Supercharging for Fuel Economy. SAE Technical Paper 2000-01-1019 (2000)

42. Liguang Li, Zhimin Liu, Huiping Wang, Baoqing Deng, Zongcheng Xiao, Zhensuo Wang, Changmin Gong, and Yan Su. Combustion and Emissions of Ethanol Fuel (E100) in a small SI Engine. SAE Technical Paper 2003-01-3262 (2003).

43. Olivier Colin, António Pires da Cruz and Stéphane Jay. Detailed chemistry-based auto-ignition model including low temperature phenomena applied to 3-D engine calculations. Proceedings of the Combustion Institute, 30(2): 2649-2656,2005.